UNIVERSITÀ DEGLI STUDI DI PAVIA

DOTTORATO IN SCIENZE CHIMICHE E FARMACEUTICHE E INNOVAZIONE INDUSTRIALE
(XXXIII Ciclo)

Coordinatore: Chiar.mo Prof. Giorgio Colombo

Development and characterization of anti-icing and anti-fouling coatings for overhead lines

Tesi di Dottorato di
Francesco Pini

AA 2020/2021

Tutor
Chiar.mo Prof. Lorenzo Malavasi

Co-tutor
Dr. Marcella Balordi (RSE spa)

Index

1 INTRODUCTION

Power grids are the backbone of contemporary society: every aspect of human life, from mass production to transport, from entertainment to health care and well-being, is highly dependent on electricity and its efficient and constant provision.

By definition, power grids consist of transmission and distribution networks; the first being long distance transport from production sites and the latter the effective delivery of electrical energy to communities.

From a physics perspective, transmission is operated with three-phase alternating currents (AC) at very high voltages (>100kV, up to 1MV) to enhance efficiency and ultimately stepped-down to service voltages (single phase 230VAC for common household use) with the use of transformers.

A large number of substations allow the connection between different transmission and distribution lines forming an interconnected network that can extend across a whole continent. It is important, for the continuity of the service, for a single node of the network to be fed by more than one input line.

A wide area synchronous grid is a regional scale power grid that operates with a coordinate AC frequency and is electrically tied together granting a pooling of generation and load aside the possibility of mutual assistance and cooperation.

Almost all continental Europe, along with some Mediterranean Sea countries, share the same synchronous grid under the European Network of Transmission System Operators for Electricity (ENTSO-E), the largest synchronous electrical grid (in terms of power) in the world. Aside this, High Voltage Direct Current (HVDC) connections are also present between non synchronous grids as, for example, between continental Europe and Great Britain.

Transmission via overhead power lines is almost always preferred over underground connections, especially when long distance transmission is involved. [1]

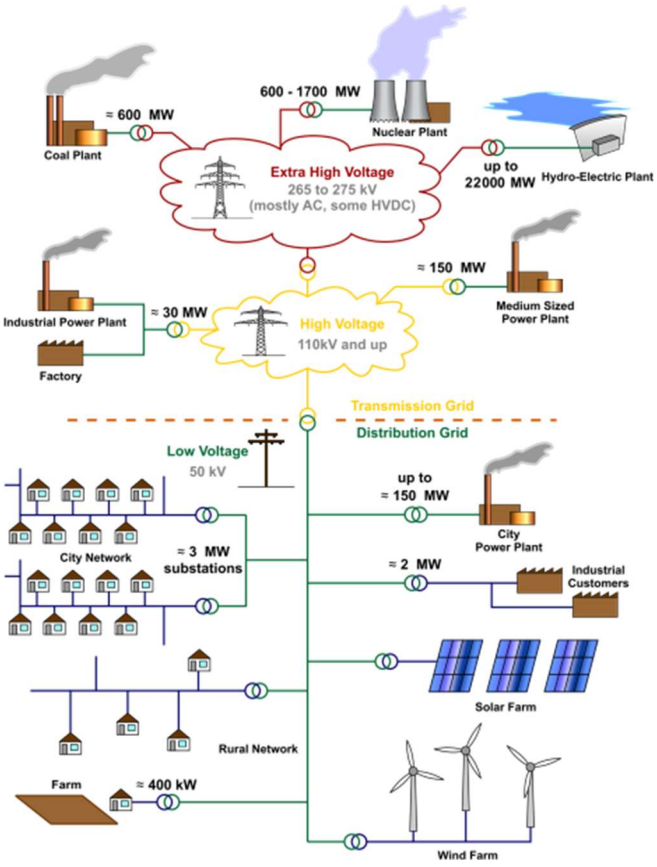

Figure 1.1 – an exemplified scheme of electrical production, transmission and distribution (from en.wikipedia.org/wiki/Electrical_grid)

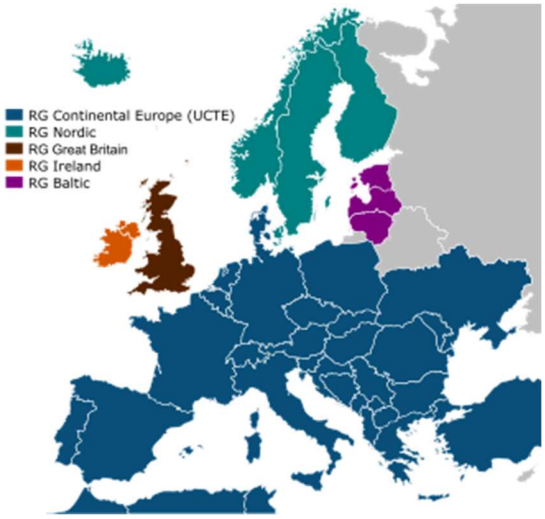

Figure 1.2 – map of European transmission system

Figure 1.3 – map of World transmission systems

When thinking of overhead power lines the first image that comes to mind is either towers and pylons, which are made of a steel lattice in case of high voltage transmission or single wood and steel poles for local distribution. Their main function is to provide mechanical support to conductors.

Towers are engineered to withstand conductor's weight along with external forces acting on them: these being unusual like earthquakes or more common such as wind and ice or snow accumulation on wires insulators and structures. Higher voltages require higher towers for safety reasons (e.g. more distance from wire to wire and from wires to electrically grounded parts). [2]

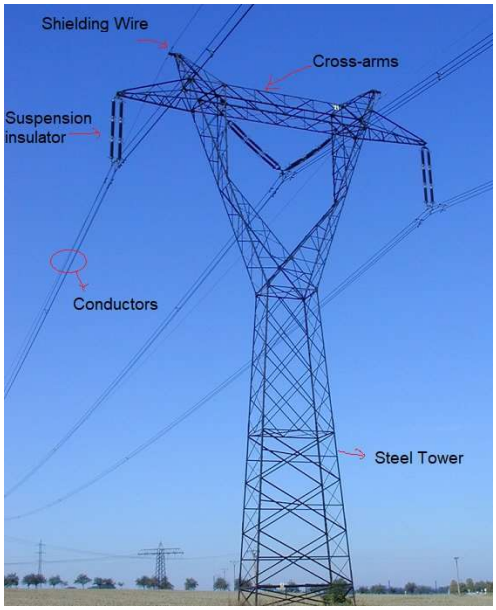

Figure 1.4 – image of a pylon: conductors, insulators, ground or shield wires are highlighted

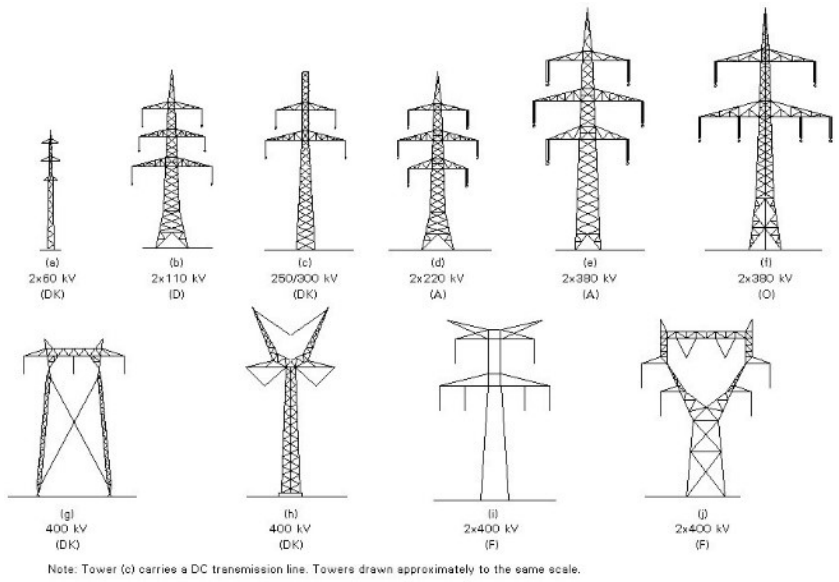

Figure 1.5 – different pylons and their voltage rating (from electicalreviews.blogspot.com/2016/06/tower.html)

1.1 Power lines components

Electrically active components of power lines, such as conductors, earth wires and insulators, are of particular interest for the following chapters of this dissertation.

1.1.1 Conductors

Conductors, exactly as the name implies, are in charge of electric conduction; for the most by far, aluminum or alloys, like anticorodal (6000 series Al alloys containing Mn, Mg and Si), are the materials of choice due to their availability, durability, mechanical resistance and high conductivity.

Conductor cables are made of multiple twisted strands, sometimes reinforced with a steel core.

Aluminum and anticorodal will be used as synonyms from now on since the presence of other metals for structural properties is not a topic in this dissertation.

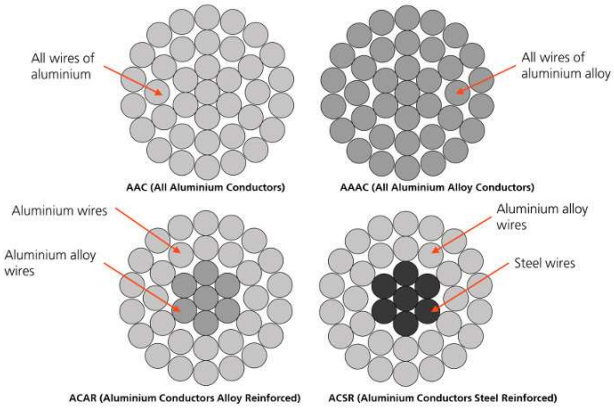

Figure 1.6 – Schematic showing conductor bundles composition (from www.theenergyofchange.com/electric-conductors-transmission-line) [3]

1.1.2 Insulators

Insulators cover a dual role in both sustaining the conductors and in providing a dielectric barrier between conductors and grounded parts. A wide variety of insulators have been and are in use, depending on line voltages, year of pose and location.

Glass insulators are of major use, although porcelain, ceramic, polymer and composites are sometimes found. Insulators are often bundled to allow a greater distance and, thus, a higher maximum safe voltage via a cap and pin chaining. A rule of thumb is to place a glass insulator for every 15-40kV, depending on insulators' dimensions in the power line.

Figure 1.7 – Image of insulators connected with cap and pin chaining (from https://powerline.net.in/2016/01/26/design-criteria/[4])

1.1.3 Earth wires

Earth wires serve multiple purposes aside providing a ground to AC: they are run at the top of the power lines to act as a lighting shield and are often coupled to optical fibres (OPGW, OPtical Ground Wires) which carry data communication as well as data about the power lines themselves. Since no current is run through them, earth wires are usually far thinner than conductors and are made of zinc plated steel (ZPS), since mechanical resistance can be prioritized over conductivity. Earth wires, just as conductors, are made of twisted strands.

1.1.3.1 Zinc plated steel

Zinc plating is applied to other metals and used as a physical barrier and as a sacrificial anode to protect the underlying metal from oxidation processes due to water, moisture and salty atmospheres. This is due to the fact that Zn forms a passivation layer which adheres to the underlying Zn, protecting it and the core metal from corrosion. This happens through a series of reactions with atmospheric oxygen, water and carbon dioxide, eventually forming an hard, compact and insoluble layer of Zn(CO3) on the external

surface. [5] Zn low oxidation potential also allows it to be oxidized instead of the metal on which it is applied.

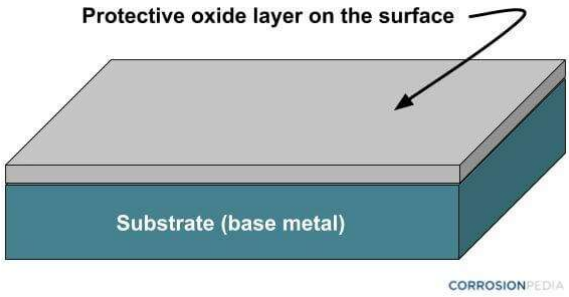

Figure 1.8 – zinc plating cross-section

1.2 The threat of ice

Ice or snow accumulation on components is one of the main dangers regarding overhead power lines.

Aside from power lines, ice and snow accumulation represents an issue in many other fields. Any metal surface exposed to cold environments is prone to high ice accumulation loads. Offshore construction, wind turbines and aircrafts being the most renowned examples. In particular, offshore constructions can suffer heavy structural damage from ice accumulation which also poses great risk to workers, wind turbines suffer both mechanically and in terms of efficiency of the rotor (aerodynamically: wing shape and symmetry of rotation) and aircrafts can suffer alterations of lift effects potentially leading to stalling due to ice accumulation on wing's edges. [6]

Ice and snow accumulation on power line components leads to sleeve accretion, resulting in multiple detrimental effects: A) increased load on wires, poles and junctions (even >20kg/m), B) a bigger wire diameter, leading to higher forces produced by winds, C) loss of wire symmetry, giving rise to aerodynamic effects which may lift the wires, resulting in a phenomenon known as galloping, adding stress to power line components as well as enhancing the risk of contact between two phases or between a phase and ground, D) high dynamic loads derived from the shedding of large chunks of ice detaching from conductors.

Delaying ice and snow accumulation and facilitating early shedding is therefore of primary importance for the safety of power lines.

Ice sleeve formation is a typical catastrophic process, the reason lying in the fact that accumulation on the top side of a conductor triggers a rotation-accumulation process resulting in the formation of a uniform sleeve all around the conductor in times dependent on the distance from the constraint. The middle part of the conductor has a more pronounced rotation than the part of wire closer to a tower.

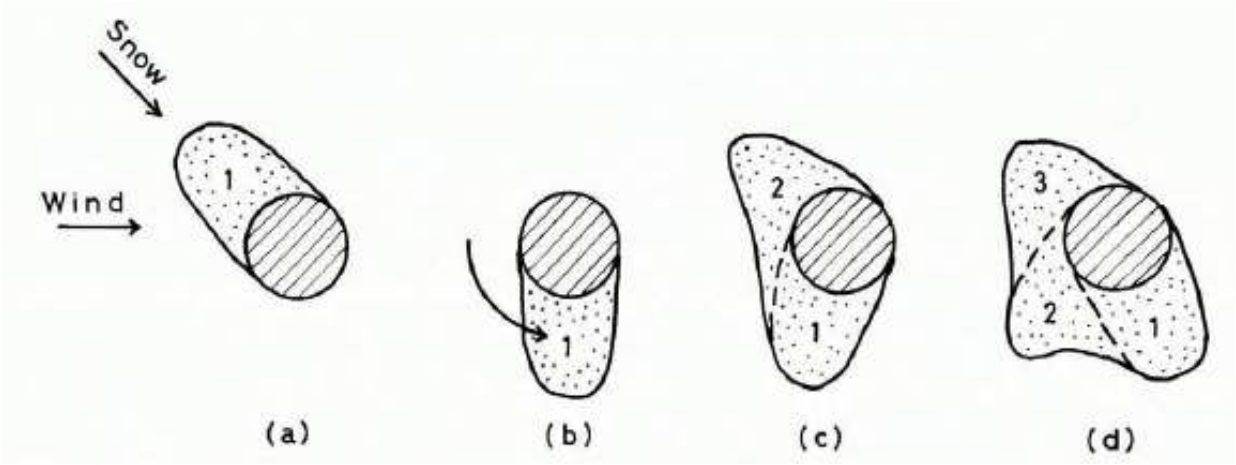

Figure 1.9 – accumulation of snow on a conductor

Makkonen published many papers on snow accretion models which have been proven to be in very good accordance with real data. [7], [8]

Makkonen's model accounts for wind direction and speed, surface roughness of conductors, their rotation, humidity and other parameters.

A schematic of the interconnection of factors influencing ice growth is hereafter reported.

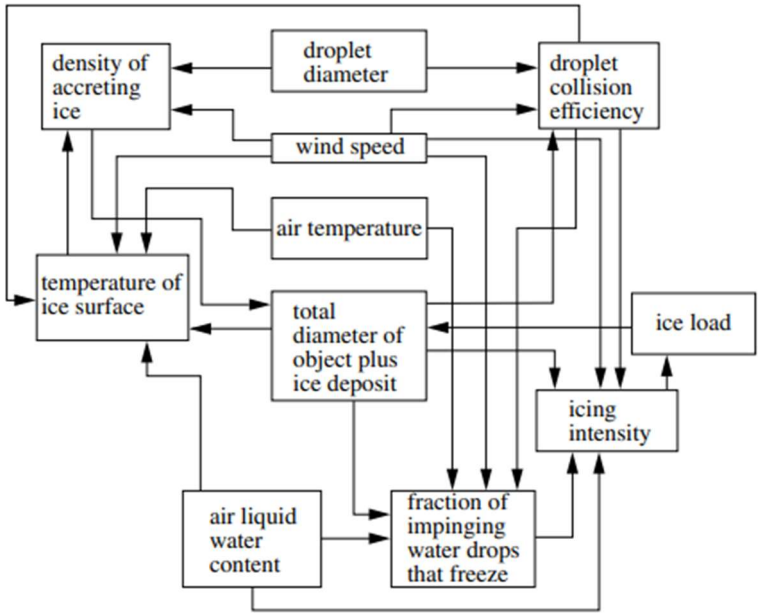

Figure 1.10 – interdependence of various factors of the icing process caused by water droplets

Models and simulations have to be taken as an example of how wide the knowledge base is when talking about anti-icing: chemistry of coatings, models of accretion, meteorological forecasting of extreme events, electrical and mechanical engineering, all come into play when trying to reduce ice-related damage to the electrical system.

1.2.1 Anti-icing methods

A vast set of solutions to power grid icing have been implemented throughout the years.

For the sake of categorization, these are usually divided in passive and active methods.

1.2.1.1 Active anti-icing methods

Active methods range from the simplest mechanical percussion of iced overhead wires by the means of a presumably insulating pole to sophisticated solutions as small rovers able to move and remove ice formations along the wires.

Figure 1.11 – a method of active de-icing

Although alluring, these rovers come with high costs, high maintenance and their use is limited to only one span of wire at a time. At the time of writing, their use is cost effective only in case of very long spans which experience extreme and continuous icing (e.g. rivers crossings).[9]

Some other anti-icing methods classified as active rely on raising the current passing through the wires, ranging from the straightforward Joule effect heating to inductances or thermomagnetic coatings.

In case of Joule effect heating, a large set of drawbacks come to mind: first of all the necessity of a larger current consumption (current needs to be requested first in order to be provided) along with the difficulty of maintaining every component of a power line within max operation parameters (e.g. wires sag, power ratings of components).

Other active methods suffer the fact that they cannot be activated when needed (magnetic heating and inductances never stop dissipating heat and power) and can create electromagnetic interference by modifying wires' overall impedance. Thus, their use is very limited.

1.2.1.2 Passive anti-icing methods

Passive methods, which will be treated extensively in the next parts of the dissertation, include chemical coatings, mechanical methods such as counterweights to defuse accumulation-rotation mechanisms and the so-called snow rings which break the ice accumulation along the wires in smaller, and easier to shed, chunks.

It is always highlighted in literature [10] how coatings need to be always ready to work as intended for long times on massive amounts of wire-length. Therefore they must be cheap, easy to apply to long spans of wire and durable across, possibly, many years of weathering.

1.2.2 Reports of major icing events

The necessity of anti-icing solutions comes from experience. Several major icing events occurred throughout the years resulting in extensive damage. Hereafter, a recall of some of the icing events occurred in Canada in 1998 and in Italy alongside some hints about which geographical and meteorological features caused them is presented. Countless other reports can be found online and in CIGRE technical brochures.

1.2.2.1 Canada, January 1998

Perhaps, the most infamous icing event on power lines occurred in January 1998 in Eastern Canada and North-Eastern US.

From January 4th to January 10th a 80 hours freezing rain precipitation occurred, accumulating as much as 110mm of ice on electrical structures but also on trees and infrastructures, resulting in 1.4 millions of people left without electricity, at least 25 people dying from hypothermia as well as others reportedly dying from carbon monoxide intoxication while trying to warm-up, widespread damage to buildings, agriculture and both livestock and wild animals.

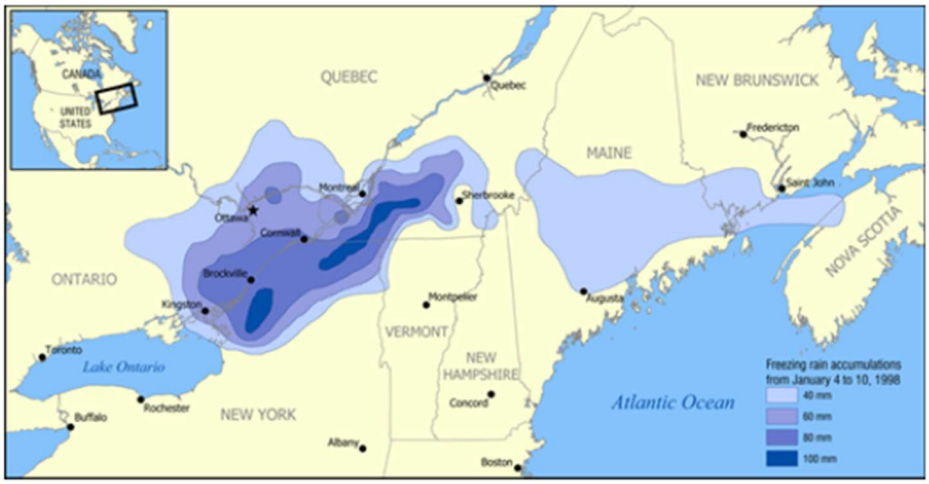

Figure 1.12 – map of NE Canada showing freezing rain accumulation from Jan 4th to 10th, 1998

Figure 1.13 – image showing the amount of freezing rain accumulated on a twig

The entirety of the power grid of the region was shut down, save one power linkage to Montreal.

One thousand pylons, 3000km of power lines and 4000 transformers were damaged by this event. Power outages in some areas lasted until the end of January, 15'000 special forces were sent to the region and damage was quantified in 6bnUSD. Briefly, the extraordinariness of the event lies in the fact that high pressure areas on Labrador and on the Atlantic Ocean forced a series of surface low pressure systems to be channelled in the St. Lawrence Valley, alternating freezing rain to steep temperature drops.

Table 1.1 – damage of 1998 Quebec storm on the power grid

Voltage level/kV	Total lines	Broken and/or collapsed towers
735	10	149
315	12	58
230	13	306
120	67	1091 (steel and wooden poles)
49	14	1500 (wooden poles)

Total	116	3104

1.2.2.2 Major events in Italy

In Italy, the January 2017 Abruzzo snowstorm and the 5-6 February 2015 Emilia-Romagna event are to be recalled and set a stepping stone to research in the field similarly to 1998 events in Eastern Canada. [11]

1.2.2.2.1 The Abruzzo, January 2017 event

In Abruzzo in January 2017 as much as 20 million tons of snow fell to the ground (1 meter of average snow covering on the whole region (~10'000 km^2), with peaks of more than 3 meters) during a snow storm spread on a two-week period. Wet snow precipitations led to pylons and poles falling to the ground in many areas. Black-outs left more than 150'000 people without electric current for a period ranging from 24h to a week or more. The situation was made worse by a concurrent seismic wave taking place in the same days making emergency and rescue operations (evacuations, disposal of generators) utterly difficult to put in place.

Figure 1.14 – a collapsed pole in Abruzzo, 2017

1.2.2.2.2 The Emilia-Romagna, February 2015 event

The events of Emilia-Romagna of 5-6 February 2015 left around 300'000 people without current for more than 8h after a heavy snowfall event. Wet snow accumulation led to more than 400 conductors failures and 18 pylons or poles falling to the ground. [12]

Table 1.2 – effects of February 2015 snowstorm on Emilia-Romagna and Lombardia (faults on medium voltage lines)

Cause	Broken conductors	Broken towers	Short circuits	Total
Ice sleeves	416	18	13	447
Fallen trees	79	1	5	85
Other causes	8	8	108	124

Total	503	27	126	656

Table 1.3 – effects of February 2015 snowstorm on Emilia-Romagna and Lombardia (users left with no power for over 8 hours after medium voltage faults)

Cause	Broken conductor	Broken towers	Short circuit	Total
Ice sleeves	202.342	4.735	9.264	216.341
Fallen trees	30.570	183	3.391	34.144
Other causes	1.139	1.278	46.635	49.152
Total	234.051	6.196	59.390	299.637

1.2.2.3 Considerations

To sum up, these events are extremely unlikely and come up from many different contributing causes but when these conditions are met together they result in abrupt and extensive damage.

Whereas a single power line interruption (e.g. a tree falling on the wires) can easily be stemmed by the complexity of the power grid engineering, icing can result in large scale interruptions, may it be for physical damage to infrastructure or safety shutdowns on the grid, resulting in widespread black-outs in a per se unusual and potentially dangerous situation as a snowstorm. Damage to power lines is only a side of the problem, whereas its consequences can be extremely harmful to small and medium scale economy and safety. Additionally, climate change is increasing the incidence of these unpredictably severe events.

1.2.3 Different "ices": glaze, rime, snow

Icing is a complex phenomenon and many different forms of ice exist. Formation of one over the other depends on current atmospheric conditions.

On earth conditions, ice can be found in 2 crystalline phases (I_c, metastable cubic and I_h, stable hexagonal). An analysis of ice crystal structure shows how cubic phase, only present in ice crystals in very cold

environments as high altitude clouds, can induce stacking faults that can even influence long-term shape of snowflakes. [13], [14]

The type of icing can be defined by either the conditions in which ice is formed or the appearance of resulting ice. Icing can be also distinguished in in-cloud icing and precipitation icing [15]. The type of icing can also be determined by the current atmospheric conditions as stated in ISO 12494 (2000)

-In-cloud icing is caused by super-cooled droplets in clouds or haze which hit the surface and freeze. Depending on the temperature and droplet size different types of ice will be formed.

-Precipitation icing is formed when rain or snow freeze upon contact with a surface. Snow will stick to a surface if the air temperature is between 0 and 3 °C, when the snow contains liquid water. Because of the presence of liquid water the snow crystals can form bonds between each other. These bonds are weak when formed but then become stronger as soon as the temperature falls below 0 °C. Precipitation icing can also be formed by rain falling when the air temperature is below 0 °C. The most common reason for this is when there is a temperature inversion, but it is also known to occur when there is a swift temperature rise, leaving the objects' temperature lower than that of the air.

Two main types of ice are commonly distinguished. The characteristics of these types are shown in Table 1.4 after ISO 12494. [16]

1.2.3.1 Glaze and Rime

Glaze is caused by freezing rain, freezing drizzle or wet in-cloud icing. A relatively slow freezing allows air bubbles not to be trapped in its structure. The resulting ice is clear, transparent and has the highest density. This ice is also very smooth and evenly distributed. Icicles can be formed when rain or drizzle falls when the air temperature is between 0 °C and -4 °C. [17]

Rime icing is a type of in-cloud icing and the most common of all icing events. Rime icing is formed when super cooled fog or cloud droplets freeze upon hitting a surface below 0°C. Usually rime ice is very fragile and has a low density. Formation time, hence the density, of rime ice depends on temperature and drop size. Higher temperature and larger drops produce ice with higher density than low temperature and small drops.

Figure 1.15 – image showing different icing types [18]

Table 1.4 – Characteristics of glaze, snow and rime

Type of ice	Density (kg/m^3)	Adhesion/cohesion	Colour	Shape
Glaze	900	Strong	Transparent	Evenly distributed icicles
Wet snow	300-600	Weak (forming) Strong (frozen)	White	Evenly distributed icicles
Hard rime	600-900	Strong	Opaque	Asymmetrical, pointing windward
Soft rime	200-600	Low	White	Asymmetrical, pointing windward

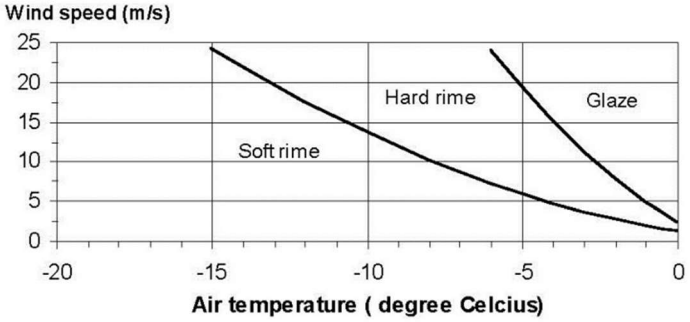

Figure 1.16 – Formation conditions of glaze, hard rime and soft rime

1.2.3.2 Snow

Snow is characterized by LWC (liquid water content) and density. LWC can range from 1-2% to around 25% with a direct influence on snow density (ranging up to 400kg/m^3).

Accumulation of snow happens in many meteorological situations. [19]

The main danger for overhead lines is represented by wet-snow forming a complete sleeve around a wire.

To form a cylinder sleeve several meteorological conditions come into play, including wind speed and direction, temperature, humidity, precipitation amount and snow LWC. It is to consider that these conditions change continuously, making every snowing event as unique as only a snowflake can be. [20]

From a physical perspective, adhesive (snow-substrate) and cohesive forces (snow-snow) must be taken into account. These can be originated and modified during the snowing event by several processes.

-freezing/variations in snow LWC,

-snowflakes bonding through freezing of supercooled water molecules on their surface,

-sintering processes,

-interactions with water vapor (sublimation processes),

-water moving in snow structure by capillarity,

-metamorphism of snow flakes,

The system we are considering is physically complex since snowfalls require temperature at the edge of a phase transition, in a wet environment. Tiny variations in temperature or any other parameter, either in simulations or reality, have a massive influence on final results. It is important to learn from past snowing events and to accumulate data so to improve our understanding and forecasting ability. Anyway, chemical coatings must be effective for every condition that can be met.[21]–[23]

1.2.4 How to test anti-icing properties : the importance of ARF

Ice adhesion testing methods are as many as the icing types. No such thing as a standard test method exists in literature. Guidelines are reported in some cases but testing must be dependant of final application of tested coatings. [24], [25]

Absolute results may also differ from one test method to the other, resulting in the need to rely on ARF (adhesion reduction factor) to evaluate anti-icing properties of a coating. [26]

ARF is a normalized measure of ice adhesion, resulting from the following equation:

$$ARF = {ice\ adhesion}_{bare\ sample} \Big/ {ice\ adhesion}_{coated\ sample}$$

This result normalization can offer some more insights on the real worthiness of a coating/material. The higher the ARF, the better the material properties.

Not even ARF can be considered an universal figure of merit, though. Some materials may perform better than others in function of testing methods, or even in function of single test parameters. A conference paper, presented at IWAIS 2022 by Balordi et al. [27] highlights how even though a general trend can be seen between samples with different roughness and coatings, testing conditions can influence relative and absolute results in terms of ice adhesion and also standard deviation between values. In this paper a tensile test machine has been used to measure the force needed to take an aluminum cylinder out of a cup filled with water and kept in a freezer for different times to allow icing. This paper shows how uncoated samples are always ordered from the smoothest to the roughest in terms of ice adhesion but this is not true anymore when talking about coated samples. A higher (-8°C) ice temperature results in lower adhesion than the one obtained at -16°C for almost all the samples, whereas the time spent at -16°C has antipodal effects on ice adhesion values and their distribution in function of their surface treatment.

This analysis gives a very deep insight on processes involved in icing and the way ice evolves in one of the most used ice adhesion testing methods. Still, these results are just faintly relatable to results of testing with, say, centrifugal testing or vibrational ones.

Ice testing gets even more complex when considering outdoor or large scale indoor testing. Aside economical constraints, it falls victim of the unpredictability of meteorological conditions, not only in terms of how ice and snow accumulate, but also depending on if, and when, useful (abundant and possibly

damaging) precipitations come on a single testing site which can host an handful of samples in a single winter. For this reason, the many samples obtained in laboratory testing throughout the year must go through a bottleneck which rules of selection are based on data, their comprehension, but also speculation and, possibly, an hint of good fortune. [28]

1.3 The threat of pollution

On the other hand, insulators suffer from the accumulation of dirt in form of organic materials, carbon, salts and dust.

Depending on the environment, ratios between these dirt forms can vary. E.g. in a urban environment accumulation of carbonic particles from smog is of major importance whereas in a seaside environment salt and sand deposits account for the most of the dirt accumulation.

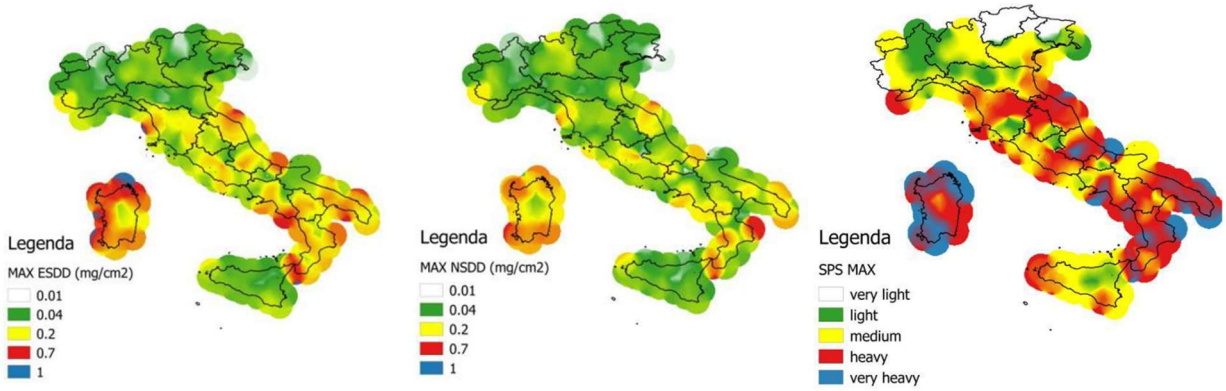

Figure 1.17 – soluble (ESDD), non-soluble (NSDD) and total dirt accumulation on insulators on Italian soil

Dirt accumulation on insulators poses a danger by making flashover phenomena more likely to happen.

1.3.1 Flashover phenomena

Flashovers consist of disruptive arc-discharges of electricity above insulators.

When an insulator is wet, a current, proportional to the salt/carbon content of water upon its surface, is directed to ground, in a similar fashion to a shunt resistance in an electric circuit. This current, although in the mA range, raises the temperature of the medium it passes through and leads to water evaporation and the eventual formation of small (10-30 mm) dry bands on the insulators.

When a dry band forms, a significant part of the voltage of the power line is applied in a very narrow space (some cm) at the two sides of the dry band. When the potential breaks the dielectric medium (30kV/cm for dry air, <10kV/cm wet air), air starts ionizing and an arc can form. Arcs can then bound together and create an electric contact between the line and grounded parts, leading to a flashover which can mechanically break insulators and wires. A short circuit on the line can also trigger protection mechanisms, or worse, can discharge to ground posing a great risk for safety. [29]

Figure 1.18 – Flashover in laboratory conditions

Deposit quantity on insulators is weighed in terms of ESDD (equivalent salt deposit density) and NSDD (non-soluble deposit density).

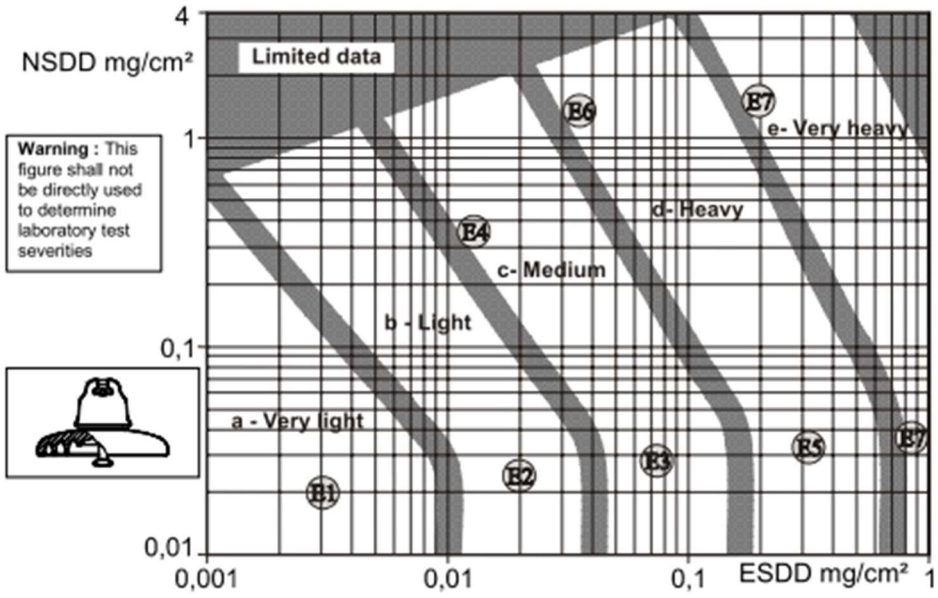

Figure 1.19 – ESDD and NSDD concentrations on polluted insulators (from https://www.inmr.com/pollution-performance-insulators-current-approximations-future-needs/)

ESDD is defined by the concentration of NaCl that, dissolved in demineralized water, would give the same volumetric conductivity as that of the natural deposit removed from an insulator surface, normalized to the surface, and is expressed in mg/cm^2.

NSDD is defined by the quantity of insoluble contaminants removed from an insulators' surface and is expressed in mg/cm^2.

ESDD is made of various different salts, depending on the location.

NSDD is composed mainly of ferrites, alumina and silicates.

Whereas ESDD's effect on flashover voltage might be straightforward, NSDD's are reportedly lowering flashover voltages as well.

Obenaus' model and subsequent iterations describe the equivalent circuit of a polluted insulator exhibiting a dry band and a conductive wet layer. The shorter the distance X (as shown in figure below), the lower the voltage needed for an arc discharge to happen.

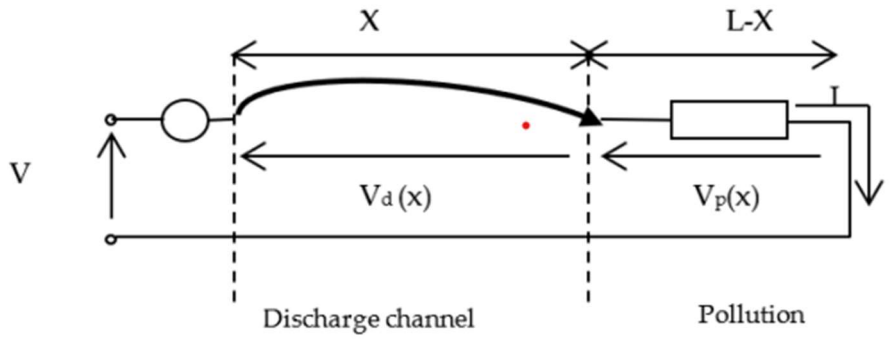

Figure 1.20 – Equivalent circuit based on Obenaus' model. V is applied voltage, $V_d(X)$ discharge voltage, $V_p(X)$ pollution voltage, I leakage current, X discharge length, L-X non shunted insulators creepage length (from Experimental Study and Modeling of the Effect of ESDD/NSDD on AC Flashover of SiR Outdoor Insulators) [30]

Still, icing on insulators can result in similar flashover phenomena in particular conditions allowing a small layer of liquid water to be present and act as a conductor.

Usually, ice accumulation on insulators doesn't pose mechanical threats, excluding the falling of heavy and/or pointy ice chunks on humans, since insulators are attached directly to the pylons, thus providing a neglectable torque and mechanical stress.

In this light, anti-icing coatings for conductors and anti-fouling coatings for insulators are of great importance for the overall safety of the power grid.

2 STATE OF THE ART AND DEFINITION OF TERMS

2.1 Hydrophobicity

Hydrophobicity and wettability properties are of primary importance in understanding ice adhesion and anti-fouling mechanisms.

A liquid, when in contact with a surface, is subjected to two kinds of forces: cohesive and adhesive.

Adhesive forces between a liquid and solid cause a liquid drop to spread while cohesive forces within the liquid cause the water droplets to ball up and avoid contact with the surface.

2.1.1 Contact angle

Wettability is usually expressed in terms of contact angle (CA), which is the shape of the liquid-gas interface. When the liquid is water, a CA >90° describes a hydrophobic surface and a CA <90° indicates a hydrophilic surface.

At the thermodynamic equilibrium the three interfacial energies (γ) at the liquid-gas (surface tension), solid-gas and liquid-solid phase boundaries are described by Young's equation:

$$\gamma_{SG} - \gamma_{SL} - \gamma_{GL} \cos\theta_{CA} = 0$$

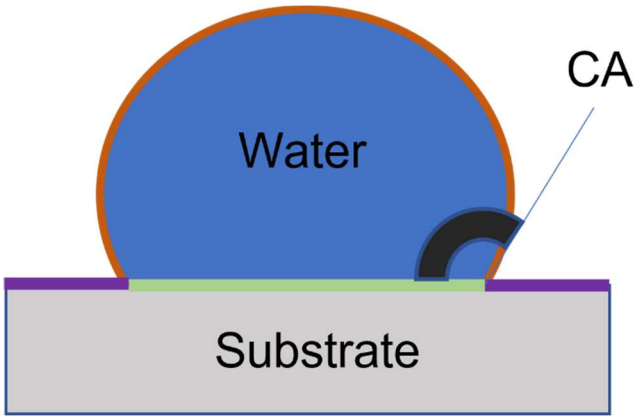

Figure 2.1 – Scheme of forces acting when water is in contact with a substrate. Interface energies are highlighted in different colours (S-L light green, L-G orange, G-S purple)

Typically, CA is measured via sessile drop measurements with a contact angle goniometer. CA goniometers are optical systems deriving the shape of a pure liquid droplet on a surface with the help of a imaging software.

Non-polar surfaces repel water much more than polar ones and result in higher contact angles. Plastics and hydrocarbon based compounds are hydrophobic, metals and ceramics are hydrophilic.

2.1.2 Water dynamic properties (tilting angle, CA hysteresis)

Another measure of water adhesion is given by tilting angles, which describe the dynamic properties of a surface. This kind of measurement is performed by placing a liquid droplet upon a sample lying on a tilting goniometric table which is gradually moved from horizontal to vertical. As soon as the droplet starts to move from its original position, tilting angle is recorded.

Tilting angles can be either expressed as sliding angles, if the droplet slides away by moving parallelly to the surface, or roll-off angles, when the droplet is effectively rolling away from the surface with a rotating movement as a ball or a wheel; roll-off behaviour is very typical to superhydrophobic surfaces (SHP).

This kind of water contact on a surface was first presented by Cassie and Baxter indagating on rough surface properties.

The Cassie-Baxter model is based on the assumption that water sits on the tips of surface roughness as well as the air in it contained. The following equation, where θ_{CB} is Cassie-Baxter contact angle, f is the fraction of liquid-solid contact (deviation from ideal conditions):

$$\cos\theta_{CB} = f(\cos\theta + 1) - 1$$

When $f = 1$ the system is in a Wenzel state. In Wenzel state droplets are sunk into the roughness of the structure beneath them, as can be seen in the picture below.

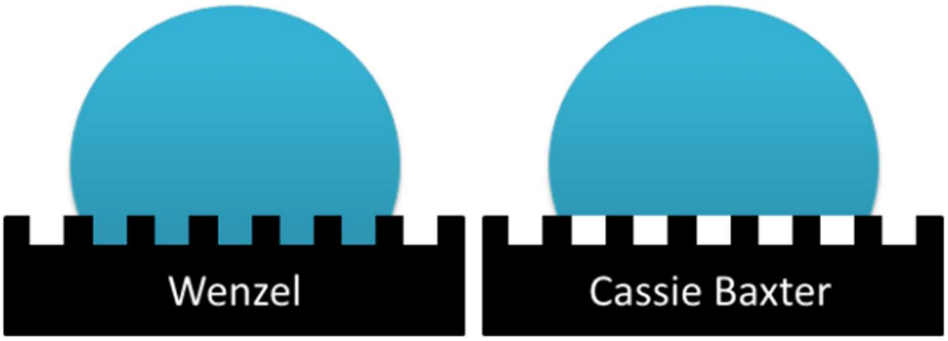

Figure 2.2 – Cassie-Baxter and Wenzel states (from [31])

In reality, Cassie-Baxter and Wenzel states coexist [32], [33], depending on a wide variety of factors including nano roughness dimensions, surface chemistry, water impact and dimensions of the resulting nanodroplets and condensation phenomena. Koishi et al. provided insightful simulations on some of these features.

Low tilting angles are regarded [34] as the most important property when it comes to find a correlation to anti-icing and anti-fouling properties.

2.2 Superhydrophobic surfaces (SHP)

Nature offers some remarkable examples of superhydrophobic surfaces: lotus leaves, *salvinia molesta*, butterfly wings and duck feathers being the most cited ones. [35], [36]

Either being created by the beholding beauty of evolution or synthesized in a scientific laboratory, SHP materials rely on somehow similar chemico-physical features.

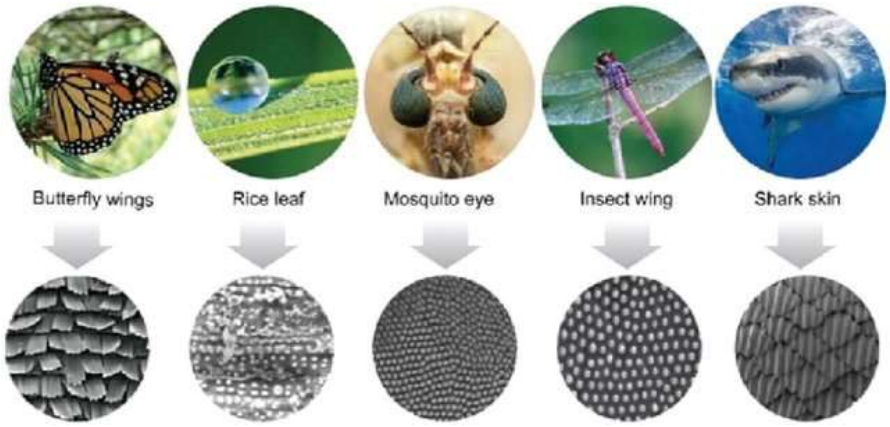

Figure 2.3 – Examples of SHP surfaces found in nature

For superhydrophobic properties to arise, surfaces need to have both micro- and nano- metric sized roughness on their surfaces. This kind of surface structure is often referred to as hierarchical.

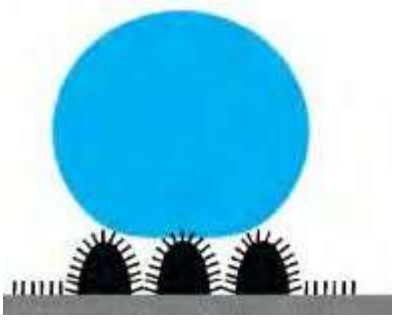

Figure 2.4 – Droplet sitting on a SHP micro-nano hierarchical surface

When such a pointy surface is also hydrophobic (e.g., after a chemical coating), water droplets on its surface form almost perfect spheres. In order to minimize surface of contact, water droplets stay in a Cassie-Baxter state, sitting on the tips of the surface.

This effect, known as Fakir effect [33] leads to high water mobility (CA>150°, Tilt <10°).

Superhydrophobic materials have been researched and developed starting from different backgrounds, with more specific research inputs coming from research fields directed towards water repellence, ranging from anti-corrosion on structures [37] to anti-fogging in glasses.

Oil water separation is also an interesting topic when talking about SHP.

Continuous water/oil separation is of great importance when reducing marine and environmental pollution. [36], [38]

2.2.1 SHP and anti-icing

Correlation between super hydrophobicity and anti-icing properties has been under fierce debate. This debate was sparked by Kulinich et al.'s publication [39] "Superhydrophobic Surfaces: Are They Really Ice-Repellent?", eventually leaving the answer to experiment and observation. From one side stands the explanation for which water, not adhering to the substrate in liquid phase, will neither adhere to it in solid phase; to the other side, mechanical interlocking between ice and the very rough surface of a SHP is given as an equally reasonable proof. [40]

Given such a discording knowledge base, a specific testing can be clarifying.

It is worth to note that many icing types exist and literature often reports a specific combination of icing and testing. (E.g. snow adhesion is very different from impact icing adhesion)

2.2.2 SHP aluminum surfaces

SHP Al surfaces have been characterized and open-field tested in the group of research. [41].

Aluminum samples were imparted a microstructure with sandblasting, shot peening or acid etching. An hydrothermal treatment has been exploited for the formation of a hierarchical structure on Al surfaces.

When Al is immersed in 100°C water, a layer of nanometric Pseudo-Boehmite (AlO(OH)) is formed from the oxide layer on its surface. [42]

The so-formed hierarchical structure becomes SHP after a treatment with an hydrophobicizer which can be bonded to the -OH moieties on its surface with a condensation reaction.

2.2.3 SHP Zinc oxide nanorods

ZnO NR, which represent the majority of the work on SHP hereafter reported, have been researched intensely during the 00's. [43]

Zinc oxide nanorods (ZnONR) are ZnO nanostructures which have been known since many decades and used in particular for their semiconductive properties as opto-electronic devices, thermoelectrics, etc.

ZnONR form in a hexagonal prism shape, following ZnO unit cell. ZnONR length can reach 100-1000um size while their width is usually under 100nm. The ratio between length and width is usually referred to as aspect ratio.

Their morphological properties are particularly appealing to obtain SHP surfaces.

ZnONR semiconductive properties (as piezo-, thermo-, photo- electric materials), which are comparable to far less common and expensive compounds, have drawn lots of attentions.

ZnONR can be prepared in many different ways, most importantly via hydrothermal growth from a solution containing a Zn salt and a templating agent. Templating agents such as Hexa Methylene Tetramine (HMT), citric acid and others, provide a growth cap on the sides of the hexagonal prisms promoting the growth only in their z-direction.

ZnONR are found in wurtzite phase, with an hexagonal cell. [44]

Several conditions of ZnONR growth are reported in literature (hydrothermal, PVD, plasma, microwave, sonochemistry, electrochemistry) but, given the large amount of information about ZnONR growth, the research have been focused on easy to produce, resistant NR with short growth times and without the use of environmentally dangerous chemicals. Given that the common use of ZnONR is very different from the one here researched, their synthesis must aim towards scalability, safety and low energy use. [45]–[48]

The synthesis of SHP ZnONR on zinc plated steel is sparsely reported in literature. Even less citations are available for hydrothermal growth of such synthesis. [49]

The use of fluorinated alkyl silane (FAS) and stearic acid as hydrophobicizers are instead well documented, although the use of stearic acid with the aim of obtaining an anti-icing surface is difficult to find in literature.[50]

2.2.4 Aim of the research

Research was aimed to find the best possible combination of treatments to be applied to zinc plated steel earth wires. Bearing the needs of a large scale-up in mind, low-energy consuming processes with the lowest count of harmful chemicals have been pursued. ZnO NR have been used for their morphological

properties instead of their semiconductive ones. In this light, hydrothermal treatments were tailored to provide an optimal trade-off between treatment times, temperatures, reactants and reliability.

Outdoor tests have been conducted along with indoor tests.

2.3 Elastomers

Elastomers are a class of polymers with peculiar mechanical characteristics: low young modulus and high deformability. The term has a very wide application and the focus will be on silicon-based compounds only.

These silicon based elastomers are often referred to as silicones or siloxanes. Chemically speaking, materials exposed hereafter fall under the category of PDMS (PolyDiMethylSiloxane) or very similar molecules.

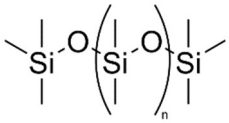

Figure 2.5 – PDMS molecule

2.3.1 PDMS

PDMS is widely used in many different fields of industry due to its unique combination of chemical properties: chemically inert, thermally and electrically insulating, hydrophobic, elastic, “soft but solid” (viscoelastic being a more appropriate definition). In most formulations PDMS is spread like a very viscous liquid; after some time (ranging from few minutes to 24h), either via solvent evaporation or chemical reaction, the elastomer is set and “solid”.

Sylgard PDMS (Syl or Syl PDMS from now on) are commercial products sold by Dow Chemicals. Syl PDMS is sold in two components (A+B) that react after being mixed in 10:1 ratios. Their setting time is few hours at RT, <1h at 120°C.

2.3.1.1 Hydrosilylation reaction

Two component PDMS elastomers rely on hydrosilylation reactions to form an interconnected chemical structure leading to a very elastic solid material. [51].

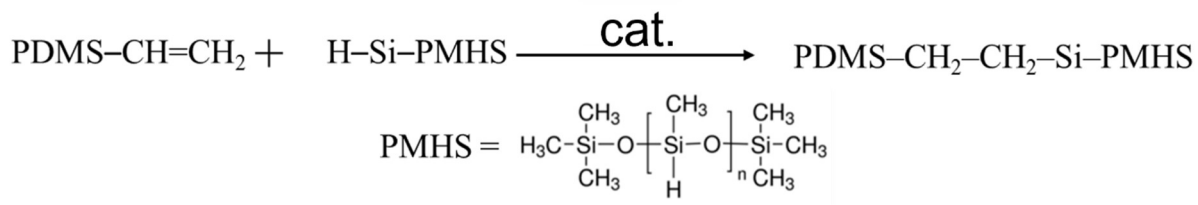

Figure 2.6 – Scheme for hydrosilylation reaction

Hydrosilylation reactions can be catalysed by various noble metal based compounds, the most renown being Karsted's catalyst (Platinum(0)-1,3-divinyl-1,1,3,3-tetramethyldisiloxane). Such catalysts can coordinate double bonds and H allowing them to react. Hydrosilylation is by itself a thermodynamically favourable reaction but doesn't proceed until a catalyst is added. [52]

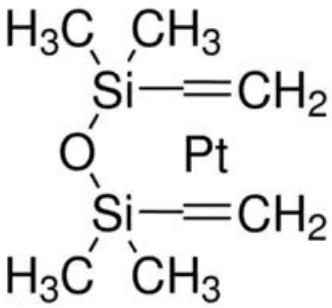

Figure 2.7 – Karsted's catalyst

In case of Sylgard PDMS, the A part contains vinyl terminated molecules whereas the B part provides hydride moieties. Given the different viscosities, it has been hypothesized that the vinyl equipped, longer chains are bound together by the hydride-containing short chains to create an interconnected net-like structure which eventually transitions from a very viscous liquid to an elastic solid. [53], [54]

2.3.1.2 PDMS as anti-icing material

The mechanisms behind the anti-icing properties of PDMS are described by an empirical formula proposed by Kendall and Chandury to calculate ice detachment from a thin film

$$\tau_{ice} \propto \sqrt{\frac{W_{ad}\ \mu}{t}}$$

Where τ_{ice} is shear stress of ice adhesion, W_{adh} is work of adhesion, μ is material shear modulus and t is thickness. This equation explains some of the trends reported in literature and seen in data. As seen,

PDMS' low work of adhesion (as an hydrophobic surface), low surface energy and viscosity (intended as the ability of a thick film to self-sustain until setting is complete) come into play. The stick-slip mechanism proposed by Beemer et al. [55] gives a little more insight on the mechanism behind ice detachment from soft elastic films: when a shear force is applied to detach ice from PDMS, the practically unavoidable small distance between the plane of shear force and the free PDMS gel surface results in a torque. This in turn results in stretching of the free PDMS gel surface behind the rear end of the ice block. At sufficiently high tensile stress, the PDMS gel surface locally peels off and detaches from ice, then the van der Waals forces ensure that ice reattaches to the PDMS gel, but only after trapping an air cavity at the interface. This locally detached air cavity propagates as a separation pulse. This local detachment of ice on a small surface rather than a total detachment contributes to obtain very low ice adhesion.

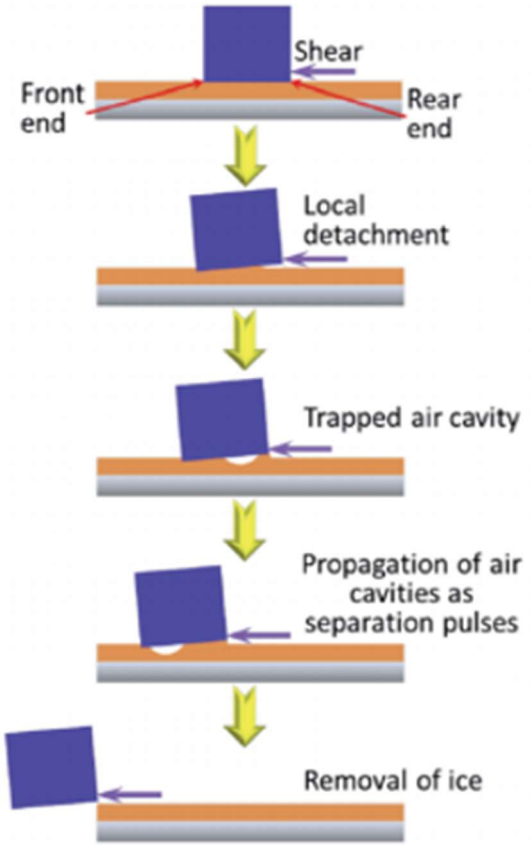

Figure 2.8 – Schematic for ice detachment from an elastic surface

Research on PDMS as an anti-icing material is wide.

Bulk or thin film, smooth or patterned to obtain hierarchical structures, filled with solid or liquids, PDMS elastomeric surfaces always report remarkable anti-icing properties. [56], [57]

It is safe to say that Sylgard PDMS 184 and 186 is regarded as a standard, a base to start from to investigate the effect of further modifications.

PDMS is also used as a standard icephobic substrate to investigate particular physical processes in the formation of ice. [58]

On the other hand, its use to avoid snow accumulation lacks literature reports; partly due to the difficulties in the production and characterization of snow.

2.3.2 Modified PDMS

PDMS can also be infused with hydrophobic molecules and lubricants in order to improve its anti-icing properties. [59]

Many papers report of silicon oil, organic oil and other molecules incorporated in PDMS.

Such molecules can be squeezed out of the PDMS matrix upon its surface making it even more hydro/ice-phobic.

Molecules can be mixed to PDMS liquid components, which are then allowed to react, being incorporated in the PDMS matrix, prolonging durability. [60]

PEG-400, Pluronic (copolymer of Poly Ethylene Glycol and Poly Propilene Glycol) and silicone oils have been used to obtain a lubricating layer, may it be made of oil or water, upon a PDMS surface. PEG-400 is used to decrease water' freezing temperature leaving a so-called quasi liquid layer in contact with ice, making it easier to detach and shed away. Pluronic has been investigated for the same reason. Pluronic has a peculiar gel- sol phase transition due to presence of more hydrophobic moieties in its structure (PPG) that interact with water molecules creating a solution only at low temperatures, when kinetic energy of said water molecules is low. Under a certain temperature, Pluronic becomes a solution, unlike most materials which behave reversely. This effect has been exploited to obtain a material which forms a water quasi liquid layer at low temperature only. [61], [62]

Some reports about creating a porous matrix exploit soluble (and low-cost) compounds such as table sugar and salt. These templating materials are removed by immersion in water or a solvent, and the voids left behind are later filled with lubricant. [63]

It is also reported that infusing PDMS with oils melting (e.g. peanut oil) around 0°C can delay ice and snow adhesion by releasing latent heat of fusion in a temperature range which is critical for ice adhesion (Phase Change Slippery Liquid Infused Surfaces). [64]

2.3.3 Aim of the research

Research on elastomers has focused on: 1) chemical modification of surface properties, 2) physical modifications of the elastomer (hardness, thickness of coatings), 3) characterization of anti-icing and anti-snow properties, 4)analysis of treatment conditions in the light of a large scale application.

Properties modification have taken Sylgard PDMS (184 or 186) as a reference.

Aging, outdoor, anti-icing analysis have been conducted.

2.4 Anti-fouling

Anti-fouling is defined by the ability of a coating to get any particle laying upon its surface to be washed away by atmospheric water. This kind of surfaces may also be referred to as self-cleaning.

An anti-fouling approach has been pursued in order to obtain coatings for glass insulators that could reduce dirt accumulation leading to discharge and flashover phenomena.

As for anti-icing, very different coatings or surface treatments can yield similar results in terms of anti-fouling properties.

2.4.1 Hydrophobics, SHPs, Superhydrophilics as anti-fouling materials

Surfaces from superhydrophilic to superhydrophobic can be regarded as promising candidates, even though with diverse mechanisms.

-on Superhydrophilic surfaces any amount of water can wet a large surface with a continuous film so that particles can be lifted from the surface and washed away. Whereas the mechanism is still debated, some effect is seen on this kind of surfaces.

-Superhydrophobic surfaces instead rely on the high mobility of water droplets upon the surface: when rolling, capillary forces take rise between particles and water so that particles are picked up. Basically, water and dirt particles have a better interaction than water and surface. Literature reports of SHP surfaces

having anti-fouling properties. It is worth to note that SHP self-cleaning does not rely on precipitation water only but also on water condensation through what is called jumping condensate (as in Cicada wings), mechanism for which water condensed on SHP surfaces undergoes coalescence, cleaning the surface in the process. [65]

-Hydrophobic surfaces have also proven to give very good results (CA 90°-120°) due to the fact that they offer a big enough surface of contact for droplets while maintaining a better interaction between water and dirt particles than water and surface.

Regardless of surface nature, good dynamic properties (low tilting angle) are of great importance in order for droplets to move and effectively clean the surface. [66]

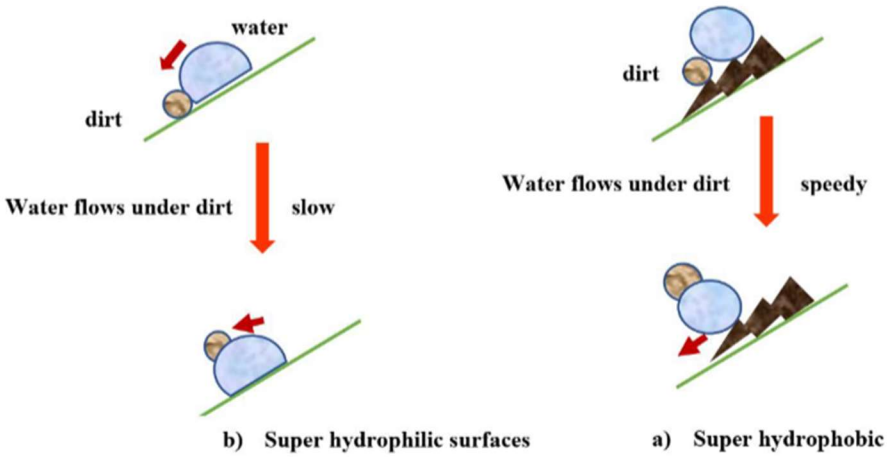

Figure 2.9 – Mechanisms of dirt removal from superhydrophilic and superhydrophobic surfaces

Self-cleaning materials are used in textile, automotive, optical, marine, aerospace, photovoltaic and construction industries and also in the medical field.

Nature, in the form of Gecko's feet, gives insight on the processes undergoing self-cleaning. [67]

Since RTV rubber is widely used in insulators coating, some superhydrophobization techniques have been reported [68]. For bare insulators, superhydrophilic properties are very often paired with photocatalysis since semiconducting metal oxides are widely available and present both characteristics.[69], [70]

2.4.1.1 Aim of the research

Research on anti-fouling materials for glass insulators have prioritized adhesion on the substrate. Several pathways present the required self-cleaning characteristics, although, respecting all off the basic prerequisites for a large scale use restricts the field even before testing. E.g. glass insulators suffer high temperatures, due to their cement/glass dual composition. The main issue regarding coatings to apply on insulators have regarded the intrinsic chemical inactivity of glass, resulting in poorly adhered coatings.

2.4.2 Photocatalytic materials

Photocatalytic surfaces are promising for anti-fouling applications on insulators, when contaminants are mainly of organic nature. These materials are used in cultural heritage conservation, as additives to concrete to degrade chemicals in air, sterilization systems and air purification.

In a photocatalytic reaction, organic molecules are degraded in a series of radical reactions. Photocatalytic materials are usually semiconducting oxides, as TiO2, ZnO,V2O5, reporting a band gap between 1.5 and 3 eV. When struck by electromagnetic radiation in the right energy window, electrons in the material hop from valence band to conducting band: a photon hitting the semiconductor causes an excitement, forming a hole (h+) in the valence band. This hole (h+) has a strong oxidising power, while the electron in the conduction band promotes reduction of acceptor species.

Materials with photocatalytic properties are well reported in literature. Photocatalysis requires semiconductors to create oxidative holes in their electron structure which are able to oxidate carbon based compounds posed in contact with them.

Photocatalytic materials include TiO2 (used for this dissertation), ZnO and mixed oxides like SrTiO3 and chalcogenides which report very high photocatalytic activities due to their electronic properties [71]

TiO2 is a staple in the field and is being used in photocatalytic concrete [72] and asphalt [73] to help reduce pollution.

Correa et al., as far as the writer's personal understanding of Spanish goes, report the use of titanium oxide coatings on porcelain insulators. The same paper reports testing in a high voltage laboratory and on a high voltage line in operation, which is a good hint on safety of operation of researched coatings. Contrasting expectations, these TiO_2 coatings seem to have no influence on leakage currents from line voltage to ground while also reportedly raising the threshold voltage for flashover. [69]

Due to their availability, TiO_2 will be investigated in terms of glass adhesion and durability.

2.4.2.1 Aim of the research

Research on Photocatalytic coatings have been focused on treatment parameters. TiO_2 has been used as a reference material for photocatalysis. Treatment parameters, adhesion to glass and the durability of the coating have been the main aim of the research. Specifically, low temperature treatments are required for insulators, due to the different materials (glass/concrete) that could mechanically fail when heated.

2.5 Hydrophobic sol-gel thin films

The application of hydrophobic thin-films as anti-icing and anti-fouling materials is wide. Many sol-gel routes have been pursued to obtain modified silicon and/or metal oxide based coatings. [74], [75]

Hydrophobic sol-gel thin films come handy in a wide variety of fields because they can be deposited in liquid phase and then be solidified with a post-deposition treatment (temperature, UV, time, solvent removal).

Chemically speaking, sol-gel synthesis relies on base or acid catalysed alkoxides hydrolysis and condensation, as reported in the image below. It is worth noting that these processes rely on water as a catalyst/reactant, making them very "green", avoiding the use of harmful solvent or, even worse, metal-organic precursors (e.g. used in CVD).[76] Base catalysed sol-gel reactions form more branched networks, whereas acid catalysed reactions lean towards the formation of linear chains.

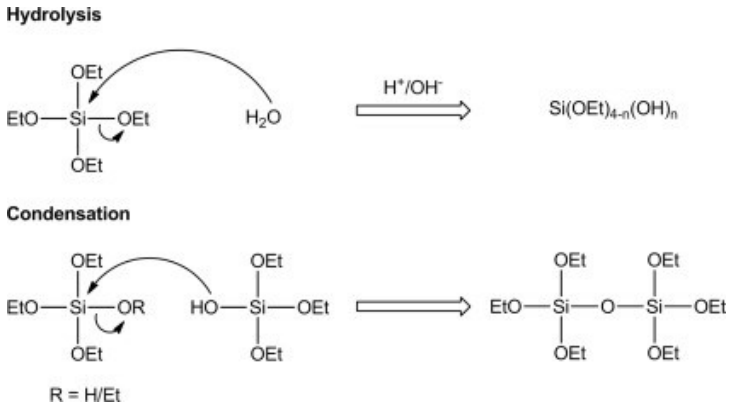

Figure 2.10 – Mechanisms of hydrolysis and condensation in a sol-gel reaction (from https://www.sciencedirect.com/topics/pharmacology-toxicology-and-pharmaceutical-science/sol-gel)

Sol-gel reactions are also widely used to obtain nanostructured powders when solvent is removed completely.

The main advantage of using a solution process stands in the possibility to fine tune the chemical composition of the resulting film. Dip-, spray-, spin-, cast- coatings can be used as deposition methods, resulting in the possibility to tailor film thickness and surface properties and morphology. Multi-layered depositions are also reported, e.g. in glasses industry anti-reflective and anti-fogging coatings can be combined. [77]

Most importantly, having free -OH moieties, sol-gel solutions can be chemically bonded to many substrates with a further condensation step.

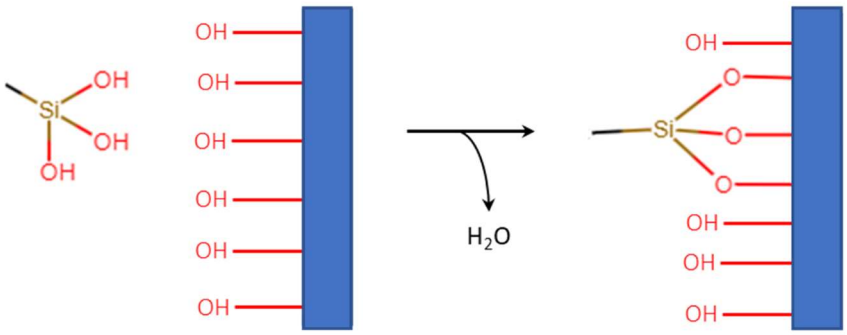

Figure 2.11 – Mechanisms of bonding of a silanol moiety to a substrate

Aside this, sol-gels can be also modified with reactive end-groups as epoxy, amine, vinyl etc. groups.

2.5.1 TEOS and derivatives

Tetra Ethoxy Ortho Silicate is of primary importance when talking about sol-gel reactions. Its structure allows to create a continuous silica film which can adhere with Si-O-H bonds to a ceramic or metallic substrate. [78]

Due to its structure with four bonding points, it can be used in the fashion of a crosslinker when mixed with other compounds, e.g. OH terminated PDMS (PDMS-OH), with fewer possible bonding sites.

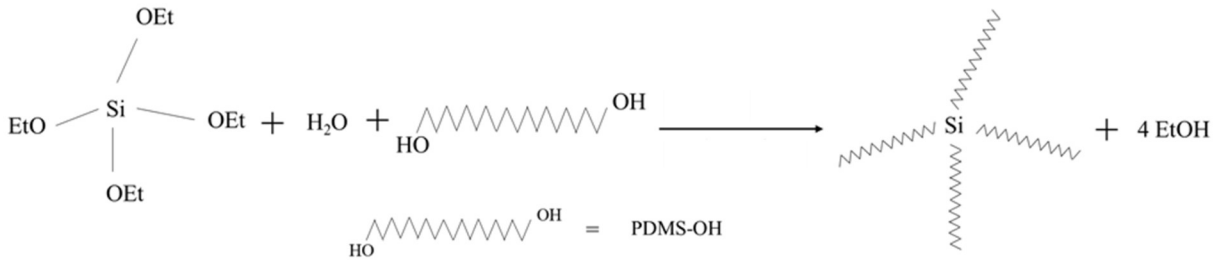

Figure 2.12 – TEOS condensation (4 reactive moieties) reaction with PDMS-OH (2 bonding moieties)

Similarly, M-TEOS (methyl triethoxy ortho silicate), providing three bonding sites, can be used in sol-gel reactions pointing towards a more pronounced hydrophobicity, due to its -CH_3 moiety.

2.5.2 Other materials

Along with TEOS, M-TEOS and PDMS-OH, other materials have been used to create icephobic or anti-fouling coatings.

Boric acid has been used in substitution of TEOS, due to the same chemical structure and the reported ability to create bond with silanes. [79]

The already reported Pluronic polymer (poloxamer) has been used to induce the formation of a quasi-liquid layer upon its surface to make ice detachment easier, due to the presence of PPG moieties in its structure which also result in a slightly more pronounced hydrophobicity at room temperature. PPG moieties also allow Pluronic to show a characteristic gel to sol transition when decreasing temperature. [80]

2.6 Snow rings

Snow rings have been reported and used, combined with anti-rotational counterweights in long (>100m) spans, in Hokkaido, Japan. Wet snow accumulating on a wire slowly slides along its strands, due to the inclination of the wire catenary. If a mechanical obstacle is put in sliding snow's way, the cylindrical accretion of the snow sleeve can be stopped and snow sleeve coherence can be negatively affected, eventually leading to an early shedding. The distance form one ring to the next is usually 75cm-150cm. Reports of effectiveness of snow rings are difficult to be found aside word of mouth, few information are found in some all-around reports on snow damage on power lines and technical report in Japanese (積雪

防止リング, standing for anti-snow accumulation rings). Anyway, the efficacy of snow rings have been tested with good results. [81]

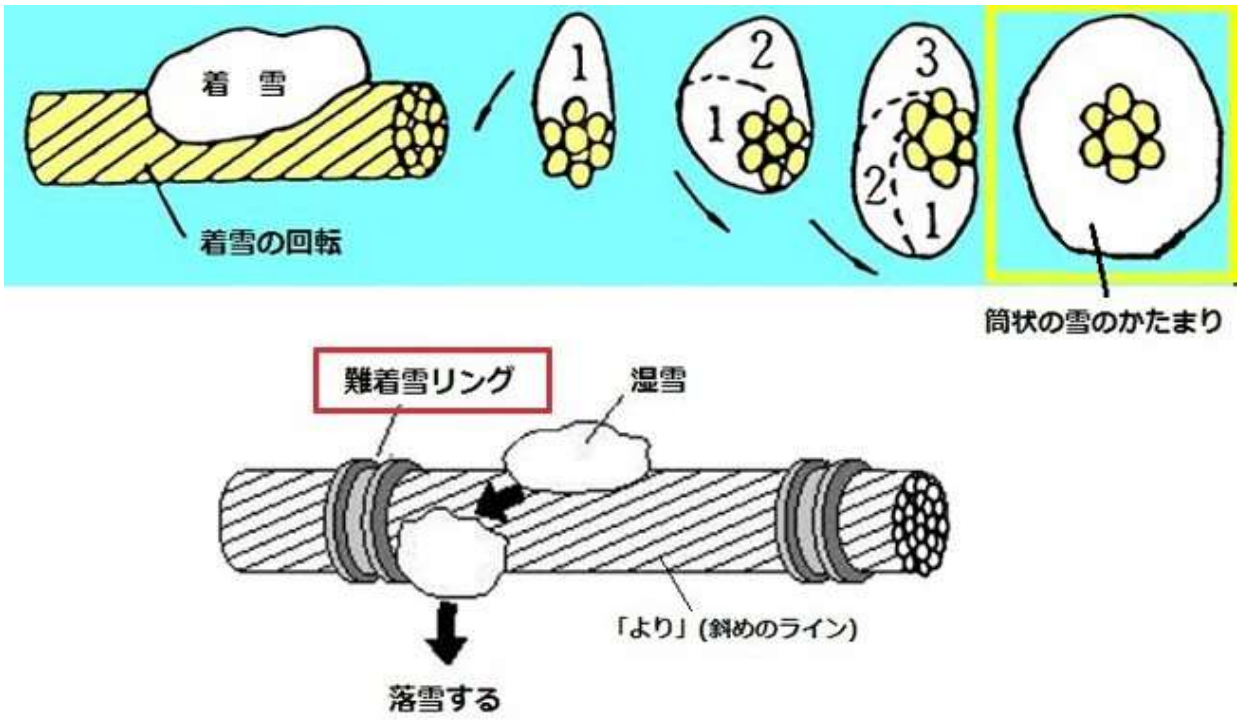

Figure 2.13 – Snow rings effect on snow accretion on wires
(https://www.hepco.co.jp/network/stable_supply/efforts/snow_prevention/index.html [82])

2.6.1 Aim of the research

Research have been focused on testing Snow Rings in open field and to assess their efficacy in preventing snow sleeve formation. Some different shapes and dimensions have been tested, thanks to the flexibility of 3D design and printing. Feedbacks on posing have been implemented from one version to the next to make an easy to install Snow Ring. The process is still in evolution at the time of writing.

3 MATERIALS AND METHODS

3.1 Chemicals

Table 3.1 – Chemicals used in synthesis and characterization

Reagent	Producer	Minimum purity (%) and notes
$Zn(NO_3)_2*6H_2O$	Sigma-Aldrich	99%
HexamethyleneTetramine (HMT)	Sigma-Aldrich	99.5%
Stearic acid	Sigma-Aldrich	95%
NaOH	Carlo Erba	pearls
Acetone		
2-propanol (iPr-OH)		99.5%
Ethylene glycol	Sigma-Aldrich	
Diiodomethane	Sigma-Aldrich	
TetraEthylenOrthoSilicate (TEOS)	Acros organics	98%
MethylTriethoxySilane (M-TEOS)	Sigma-Aldrich	90%
PEG-400	Sigma-Aldrich	
Ethanol absolute	Sigma-Aldrich	>99.5

Pluronic P-123	Sigma-Aldrich	MW 5’800
PDMS (hydroxy terminated)	Sigma-Aldrich	65cSt, 750cSt and 2550-3750cSt
HCl	Carlo Erba	37%
Boric acid	Carlo Erba	Powder
Silicone oil (PDMS)	Sigma-Aldrich	MW 95’000
PMHS	Sigma-Aldrich	
NaF	Sigma-Aldrich	
TiO_2 nanoparticles	Produced by laser ablation	20-200 nm
FAS (Dynasyilan SIVO Clear EC)	Dynasylan	Fluoro alkyl silane
ALK (Dynasilan 9896)	Dynasylan	Alkyl silane
Sylgard PDMS 184	Dow chemicals	A+B (10:1)
Sylgard PDMS 186	Dow chemicals	A+B (10:1)
H_2O_2	Sigma-Aldrich	30% in water
PDMS-vynil terminated	Sigma-Aldrich	MW 25’000
Ammonium hydroxide	Sigma-Aldrich	30-33% in water
Acetic acid	Sigma-Aldrich	99,7%

Karsted catalyst	Sigma-Aldrich	Stock 10 ppm solution
Spray glue	Maurer	
Silicone lubricant spray	Eco service	
Tesa glue	TESA	
PVDF	Alfa-Aesar	
Kaolinite (natural)	Sigma-Aldrich	
Activated charcoal	Sigma-Aldrich	100 mesh
NaCl	Sigma-Aldrich	

3.2 Laboratory testing methods (chemico-physical, ice, dirt)

3.2.1 Chemico-physical characterization

3.2.1.1 Contact angle measurements

Contact Angle (CA) has been measured with a Kruss Drop Shape Analyzer (DSA 30). The system is composed of a vertically moving head equipped with a syringe for liquid disposal, a sample holder, a temperature sensor, a camera and a backlight. Images are analysed by the proprietary Advance software. Sample holders can be swapped in function of the analysis that is needed: a tilting one for dynamic measurements (Tilting and Roll-Off) or a Peltier cooled plate with a windowed lid for cold temperature measurements.

Drop images have been fitted with tangent, Young-Laplace or manual methods to obtain CA measurements. As a rule of thumb, tangent method becomes more reliable than a Young-Laplace fit as CA gets higher in value.

Drop volume for all the analysis is 20 µl. Demineralized water have been used in all experiments.

CA have been measured on 5 drops per sample.

Tilting angles have been performed at least 3 times.

3.2.1.2 Surface Free Energy

Surface energy measurements have been conducted with Kruss DSA 30. Surface energy is calculated with OWRK method.

CA for liquids with diverse polarities (diiodomethane, glycerol, water) is measured and then an estimate of the samples' surface energy is obtained from the Advance software.

SFE is given as a sum of a disperse and a polar contribute, the first derived from mere Van der Waals interactions and the latter coming from an effective charge separation on the substrate.

3.2.1.3 Icing temperature and Icing delay

Icing delay has been measured with Kruss DSA 30 equipped with peltier cooled plate, by placing five 20ul droplets on a sample, then decreasing temperature at 6°C/min until -8°C. Icing time is recorded from reaching -8°C to the onset of freezing.

Icing temperature is measured with the same setup with the only difference being that the temperature keeps decreasing until icing is observed. This experiments give an insight on both nucleation energies and thermally insulating properties of the samples.

3.2.1.4 Scanning Electron Microscope

Scanning electron microscope (SEM) images have been taken with a Mira III, Tescan. The images show voltage, magnification and information about the technique used to acquire them.

A SEM exploits electrons to image a sample's surface. Electrons are emitted by a tungsten filament and accelerated by a high (>10kV) voltage and focused with electronic lenses. When electrons hit a sample, different interactions with matter arise.

Secondary electrons (SE) are emitted by atoms excited by the electron beam, this imaging technique is particularly suited for topography imaging since these electrons come from a very thin layer (1-10nm) of

atoms on the surface. Backscattered electrons (BSE) are beam electrons reflected by elastic scattering from a thicker layer under the surface of the sample. BSE imaging has lower resolution in respect to SE, but since the amount of BSE is proportional to atoms' Z number, differences in the chemical composition between parts of the sample can be highlighted this way.

The SEM machine is also equipped with a EDX (energy-dispersed X-ray spectroscopy) sensor. When high energy electrons hit atoms, some atom-specific X-rays are emitted, so EDX can be used to map element concentration in a sample.

3.2.1.5 X-Ray Diffraction

X-ray diffraction has been performed with a Bruker D8 diffractometer with a 2θ Bragg-Brentano configuration. X-ray diffraction is used to characterize crystal structures. Diffraction is the constructive (in-phase) reflection of an incident radiation with wavelength comparable to interatomic distance in a crystal (0.1nm) that occurs at certain angles as described by Bragg's law.

XRD can give important information on crystal phases in a sample.

3.2.1.6 X-Ray Fluorescence

XRF relies on secondary photons (fluorescence) emitted by a sample when hit with a X-ray wavelength. When struck, some core electrons are emitted and electrons dropping from higher energy levels to the one with a h+ emit very element-specific wavelengths.

XRF analysis of element concentration have been performed with a Bruker S1 Titan.

3.2.1.7 FT-IR Spectroscopy

A Alpha II FT-IR have been used for characterization.

Fourier Transform InfraRed spectroscopy is used to obtain an infrared absorption spectrum of a molecule. Peaks in the spectrogram indicate a vibration mode (bending, rocking, scissoring, etc.) characteristic of a bond in a molecule (e.g. C=O stretching appears as a strong peak at 1700cm-1) .

3.2.1.8 Atomic Force Microscope

Atomic force microscope measurements have been performed by CIMaINa (Centro interdisciplinare materiali e interface nanostrutturati at Milano University) by Dr.Chighizola.

Samples have undergone force vs indentation measurements with a 5um tip (2um typical indentation). Young moduli on such a scale have been measured. Samples have been kept in deionized water during testing to minimize adhesion between tip and sample. Several regions of interest (100umx100um) have been investigated in macroscopically separated parts of the sample. Each "point and shoot" test is composed of >100 single indentation curves, from which a mean value is derived for each region of interest. Each value is expressed as a young modulus (Pa).

3.2.1.9 Viscosity measurements

Viscosity have been measured with a Brookfield DV-1 rotational viscometer. Different spindles have been used in function of sample viscosity.

3.2.2 Ice adhesion

3.2.2.1 ice adhesion testing machine

Ice adhesion characterization has been performed on a home-built shear stress adhesion machine.

The machine consists of two Arduino Mega controllers, a motor attached to a worm gear moving a cart, a 3D printed static sample holder, a 0-10kg load cell, two 40x40mm Peltier cells in series with water cooling and a joystick for movement control.

Force of adhesion is measured by the load cell moving at a constant speed of 0.3mm/s and pressing against a 10x10x10 mm cuvette filled with ice. Shear stress is obtained from the ratio between maximum recorded force for ice surface.

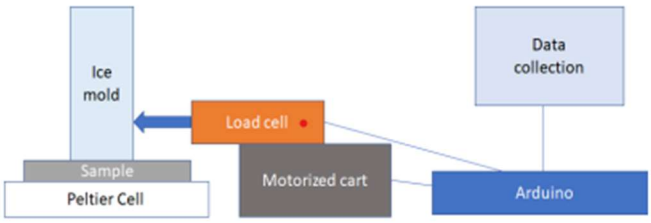

Figure 3.1 – Ice adhesion testing machine

Speed has been chosen as a trade-off between a slow movement to minimize error on the peak force and a high enough speed to avoid a heavy torque loss on the NEMA 23 stepper motor used in construction.

One Arduino is in charge of movement with a joystick controller moving the head in free mode or, when pressed, starting the test. The other Arduino records load cell data in function of time and displacement. Using two separated controllers allows more frequent readings of the load cell, up to 20Hz. Preparation of samples consists of putting a cuvette on the samples surface, filling it with 1ml of demineralized water and placing everything at -18°C for 1h in a freezer. Then the sample is put on the Peltier equipped sample holder, in order to maintain the temperature constant, and then the test is performed. The samples pass less than 60 seconds outside the freezer. Up to 9 tests have been performed on a single 50x50mm sample without evidencing errors derived from testing order.

3.2.2.2 Characterization

Ice on the samples is formed in a 10x10x10 mm polystyrene cuvette with an open top. Silicone grease is applied on cuvette rims in order to avoid water leakage and to reduce the error for container adhesion on the substrate. A correction of +10 grams (1kPa), has been applied in the load cell software to compensate this factor. Glass cuvettes showed higher ice adhesion and far higher standard deviation (>40%) than polystyrene ones. Open top cuvettes reported no difference (18% vs 20%) in standard deviation with closed top ones. Open top polystyrene cuvettes have become of use due the simple filling.

Motors and Peltier cells (which are connected in series to avoid high current surge) are operated at a voltage of 21V. Peltier cells surface temperature in function of applied voltage has been characterized and optimal operation was found around 10V instead of the maximum rated power of 12V. Hot-side cooling is obtained by placing the two peltier cells in series (electrically and thermically) above a copper heat sink with an inner flow channel for water cooling. Air cooling wasn't considered as an option due to sample holder configuration.

Every interface is thermally connected with the use of thermal paste. Water flow, once above a certain value dictated by common sense of "water flow", didn't influence cold-side temperature in this set-up. This configuration, connected to a steady flow (~1L/min) of tap water, allows the cell surface to reach -15°C.

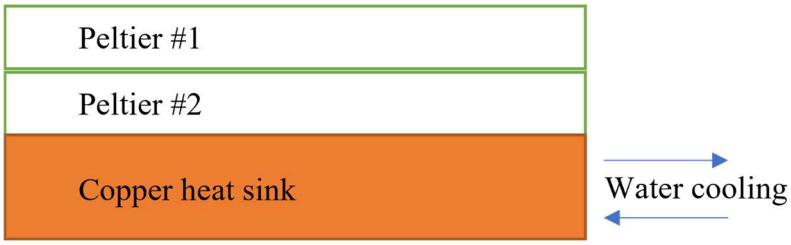

Figure 3.2 – Heat sink section

NEMA 23 motors are operated with full-steps allowing more torque in place of un-needed movement precision. High current drivers have been used.

Standard deviations of shear stress obtained with this machinery are comparable to those obtained by other methods (20%), them being reported in literature or already used by the research group.

3.2.3 Anti-fouling characterization

The self-cleaning properties of samples have been assessed by placing a known amount of simulated pollutants on both a coated glass sample and a reference untreated glass sample. The amount of water needed to wash away the pollutants is recorded. Results are reported as FRF (fouling reduction factor) which is calculated from the ratio between the water volume used to clean the untreated sample and the number of droplets needed to clean the coated sample, in a similar fashion to ARF for anti-icing characterization.

$$FRF = {water\ volume}_{\ bare\ sample} \Big/ {water\ volume}_{\ coated\ sample}$$

Carbon black, kaolin powder and NaCl have been used as pollutants to simulate NSDD and ESDD with different conductivities. FRF is reported separately for each pollutant.

Glass samples are kept on a tilting table at a 14° angle mimicking a common value of side steepness of an insulator. Both methods to measure self-cleaning properties were developed in RSE laboratories.

3.2.3.1 "Fast" self-cleaning test

For this test, glass microscope slides were covered with a known amount of pollutant powders. 20µl droplets are dispensed from a pipette from a 25mm height from the sample. When the surface is clean, water volumes needed to swipe away dirt from a coated and a bare sample are used to obtain FRF.

Figure 3.3 – Image of dirt removal

3.2.3.2 Self-cleaning "RSE method"

For this experiment, 70x70mm glass samples were used. Samples were covered with a solution of NaCl with dispersed kaolin powder and dried at 30°C. 10ml of ultrapure water have been then used to wash the surface from an height of 50mm by the means of an electronic pipette dispensing 5mL/min of water on 13° tilted samples. The quantity of NaCl washed away from the surface is obtained by measuring solution conductivity while kaolin was weighed after being collected on a 0,45um filter.

Results are given in term of FRF in respect to the quantity of pollutants which are removed from an untreated glass surface.

3.2.3.3 UV photocatalysis

Photo-catalytic properties have been monitored with FT-IR spectroscopy. In a typical experiment, 0.5ml of 10mM stearic acid in acetone solution are placed on the surface of a sample. After solvent evaporation, a FT-IR spectrum is recorded; then, the samples are exposed to UV light (4x9W UV led bulbs, 365-405nm) for a definite amount of time. Then, another FT-IR spectrum is recorded to evaluate the difference in the amounts of stearic acid on the samples before and after exposure to UV. The peaks between 2800 and 3000 cm^{-1} , ascribable to symmetric and asymmetric stretching of C-H bond in aliphatic chains, has been used to monitor the amount of stearic acid.

In the image below, FT-IR spectrograms of surfaces of TiO2_10l after 1h and 12h of UV exposure are reported as an example, showing a reduction in the peaks in the 2800-300 cm-1 area, relative to deposited stearic acid.

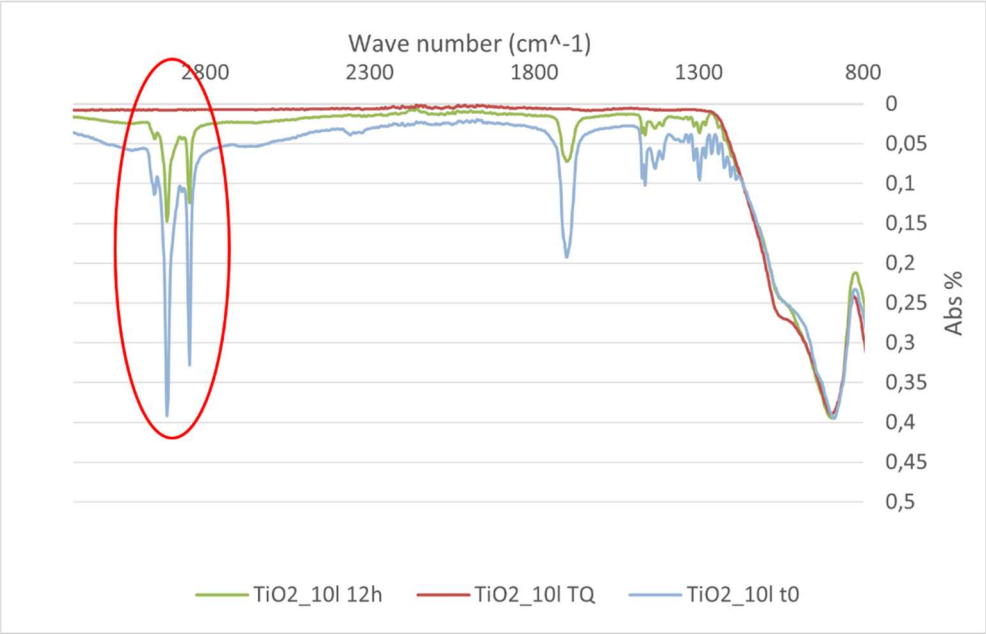

Figure 3.4 – Example of reduction in the intensity of peaks at 2800 cm^{-1} of stearic acid deposited on photocalytic samples

3.3 Outdoor, durability and dynamic ice/snow accumulation testing

3.3.1 Tape testing

Coating adhesion has been tested following ASTM D 3359-02. Samples are tested with the so-called tape testing. A cutter with a set of ten parallel blades is used to scratch the surface coating with two normal cuts. A standard 3M tape is then applied to the sample surface for a definite number of times and removed. The classification is reported in the image below.

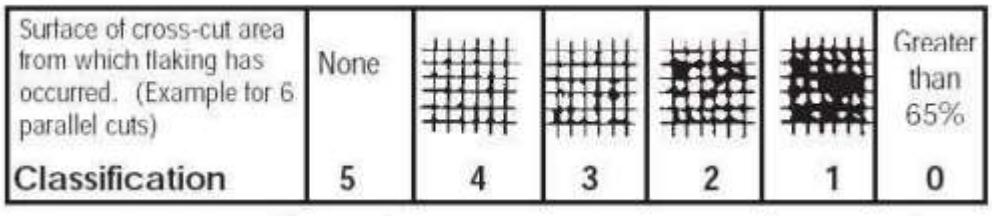

Figure 3.5 – classification of coating adhesion after tape test (ASTM D 3359 – 97)

If a thin coating is used and no visual indications can be obtained, tape test deterioration of coating is measured with contact angle and wettability characterization.

3.3.2 Accelerated weathering test

Samples' durability has been tested in a climatic chamber at the RSE facility of Brugherio. Samples have undergone cycles of stressing conditions (UV light, heat, high humidity, hot/cold cycles) as reported in the table below. To assess coatings' resistance, contact and sliding angles have been measured before and after the fast aging experiment.

Table 3.2- fast aging experiment conditions

Phase	Conditions	Duration (h)	Iterations
A	Radiation Power = 1 ± 0,1 kW/m^2 Humidity RH% ≤ 30% Black panel temperature θ = (80 ± 2) °C	71	1
B	Radiation Power = 1 ± 0,1 kW/m^2 Humidity RH% ≤ 60% Simulated rain Black panel temperature θ = (60 ± 2) °C	23	1
C	Radiation Power = 1 ± 0,1 kW/m^2 Humidity RH% ≤ 60% Simulated rain Black panel temperature θ = (80 ± 2) °C	23	1

D	Dwell at 80°C Humidity RH% = 95%	1	6
	Cooling to -30°C	1 (±10 min)	
	-30°C dwell	1	
	Heating to 80°C	1 (±10 min)	

3.3.3 Exposed samples

Samples have been exposed to the elements to assess their durability in real environment. Climate conditions can be found online and testing dates are reported for every set of samples. Area of exposure faces south-west and has high degree of dust and smog accumulation due to the proximity to a main highway and a logistic centre. Sample durability is tested by comparing properties before and after exposure.

3.3.4 Snow machine testing

Some characterizations have been made with the recently purchased snow machine.

The machine allows testing with real snow on conductor sections up to 2m.

A refrigerating system allows the chamber (2x4x3m dimensions) to be kept at low temperature. To do so, air from the chamber is taken up by a set of 4 fans and injected in again through a heat exchanger in which a low-melting fluid is passed.

The same refrigerating fluid is used to keep a rotating drum at the desired (sub-zero) temperature.

Snow is formed by drum rotation against a comb, accumulated ice is scraped away. The drum is continuously re-immersed in liquid water.

The drum can move back and forth along a span of 2 meters.

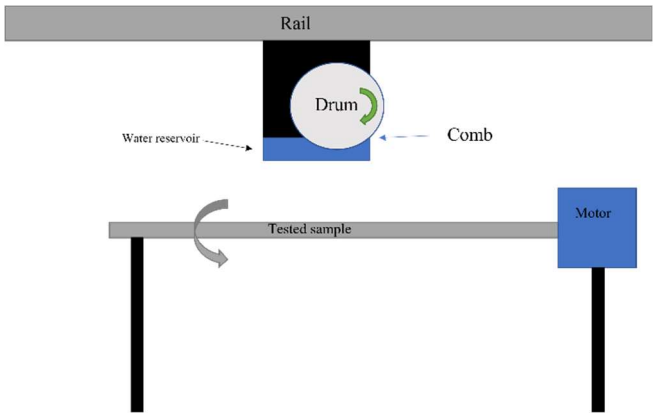

Figure 3.6 – Schematic of snow machine testing

Snow Liquid Water Content (LWC) can be tailored in certain ranges by modification of temperature, humidity and other conditions inside the chamber.

Two conditions have been optimized so far, as reported in the table below.

Table 3.3- snow machine conditions for snow #1 and #2

Test	Air T (°C)	Drum T (°C)	Air Humidity (%)	Drum speed (%)	LWC (%)
1 (dry snow)	-2.5	-5	>77	200	10
2 (wet snow)	0	-1.5	>77	100	>20

Wet snow from test 2 have been used for all characterization.

75 cm samples have been kept in a slow rotation (<6 RPM) and snow was produced all along their length.

Typically, a reference sample and a coated sample are kept parallel along the snow drum head moving direction and a video is recorded.

Reported tests are intended as preliminary, due to the short time the research group has had to get acquainted with the new instrument. Sample performance will be exposed in terms of time of snow sleeve detachment and delay in snow sleeve accretion.

The new setup, that will likely be ready in the first half of 2023 will be comprised of a modular structure frame, motors, sleeve diameter measurements, load cell to measure sleeve weight, thermal cameras and could also be operated with wire spans at a defined inclination to better simulate real conditions.

3.3.4.1 Liquid Water Content

LWC of snow has been calculated with a calorimetric method.

An amount of snow was collected in a thermos and weighed. Then a 3-5 fold amount of heated water (40-50°C) was put into the thermos and stirred until thermal homogeneity was reached. The amount of added hot water has been also weighed. Final temperature, T_f was recorded.

The following equation was used to assess LWC in snow samples:

$$LWC = \left\{1 - \frac{C}{L}\left(\frac{m_w \Delta T}{m_s} - T_f\right)\right\} \cdot 100$$

Where C is water specific heat (4200 J/kg*K), L is latent heat of fusion of ice (33400 J/kg), m_w is water mass, m_s is snow mass and ΔT is the temperature difference between water temperature and T_f.

3.3.5 Ice-wind tunnel

Tests on ice adhesion have been performed at the Airbus facility in Ottobrunn, Munich in the iCORE (icing and contamination research) ice wind tunnel. ICORE consists of a high-capacity turbine accelerating air into a loop. Accelerated air goes through a refrigerating section that shrinks into the proper test section, so to accelerate the air to match take-off speed for aircrafts (max 150 m/s) and obtaining laminar flow. Three nozzles placed at mid-height before the shrinkage allow the user to spray water droplets with the aid of a carrying gas (20-50um diameter, depending on pressure and other parameters). These supercooled droplets freeze on the samples in the test section. Glaze ice, rime ice or in between phases can be accreted by varying carrying gas (compressed air) pressure, water flow, wind speed and temperature. [83]–[85]

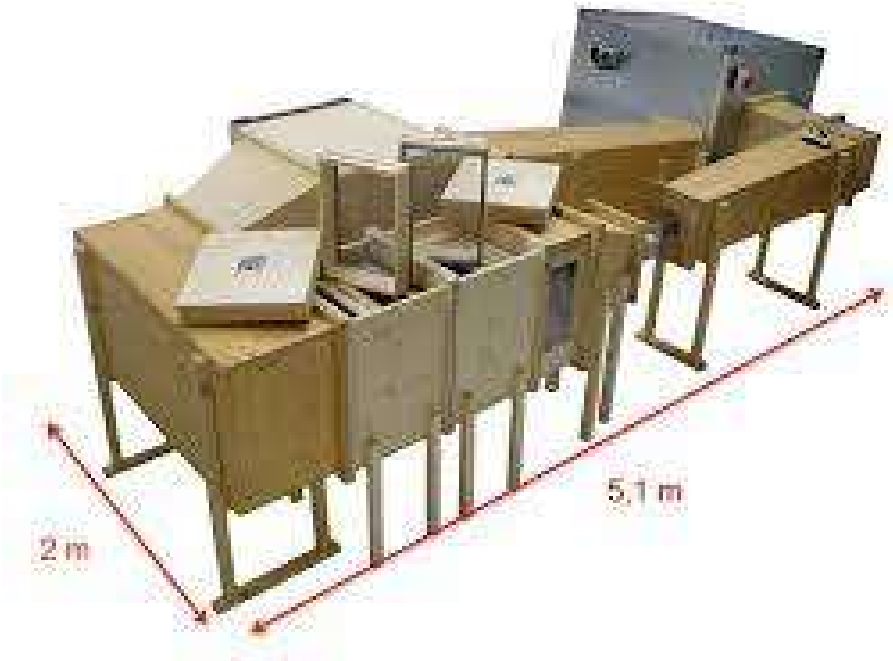

Figure 3.7 – Image of iCORE

Test section has plexiglass walls to allow one or more cameras to catch images of ice accretion and shedding.

The ice wind tunnel is equipped with sensors of pressure, temperature and humidity.

Tests have been performed on cylindrical and flat (cantilever) samples. In both cases rime and glaze have been accreted on the samples by varying water flow, carrying gas pressure and temperature.

Pitot tubes placed in the test section allow analysis of static e total pressures that can be converted into wind speed along with temperature data gathered from thermocouples placed into the tubes. A software allows to control rotation of the turbine. Three parallel compressors and a power regulator control the amount of cooling.

A preliminary test was performed to map the wind speeds in function of turbine frequency. The cooling power to keep wind at the same temperature in function of wind speed have also been mapped, since increasing wind speeds would bring to higher temperatures due to kinetic energy.

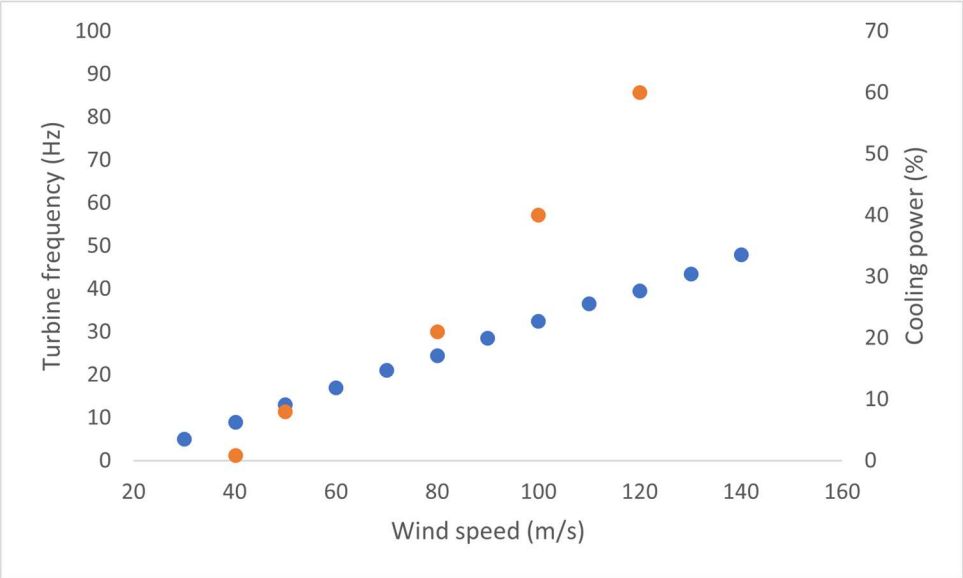

Figure 3.8 – Turbine frequency (blue) and cooling power (orange) in function of wind speed. Temperature has been maintained at -3°C.

-Ice adhesion tests on cylinder samples have been performed in rime and glaze conditions on 12mm diameter x 100mm length cylinders coated with different materials.

After accretion time, the samples were rotated by 90° and wind speed was raised with 10m/s steps every 20s, while keeping the temperature stable, until ice was detached from the surface so to obtain a measure of ice adhesion. If ice couldn't be detached from samples surface even at max wind speed, then the cooling stage was turned off resulting in a increase in temperature of around 2°C/min. Results are expressed in terms wind speed and temperature of ice detachment.

-Cantilever testing resulted in very confused data which will not be included. Testing relied on accreting an amount of ice (glaze or rime) on the cantilever (coated aluminum samples) so to obtain an ice sleeve with the same young modulus as the aluminum substrate. The samples have been equipped with strain gauges to record vibrational deformation and bound to a vibration motor. Amplitude of vibration was increased until ice detached. Since ice and substrate have the same stiffness, vibrations are symmetrical. When ice started to detach from the substrate, a rattling movement was induced resulting in a asymmetrical strain. The strain at which this symmetrical/asymmetrical transition happens is recorded. Results are usually reported in terms of shear stress of ice adhesion.

3.3.6 WILD test station in Vinadio

Outdoor tests on 75cm (30 mm diameter) and 15m (9-12mm diameter) wire spans have been performed on samples exposed in Vinadio, Cuneo, Italy in the Western part of the Italian alps in the RSE WILD [86] laboratory. The laboratory is in a side valley at around 1000m asl and close to the sea, which guarantees high amounts of precipitation in winter. WILD station receives only minimal direct sunlight during winter.

Samples are mounted and put into a slow rotation to simulate wire torsional movements. Meteorological data are recorded (temperature, humidity, direction and speed of wind, amount of precipitation). Cameras are pointed at the samples so to obtain video data of snow accumulation and shedding.

Figure 3.9 – webcam image of the WILD station on a nice winter afternoon (top-left and right 12 slots for 75cm samples, bottom-left: insulator testing , Bottom-right:15m wires)

3.3.6.1 Coverage and Load indexes

Performances of exposed samples have been evaluated by assigning an index of snow coverage normalized to 1, which is attributed to reference sample. Images taken every 15 minutes are analysed and given scores.

Images are analysed visually by some operators, assigning a Coverage index score to each sample for every frame during precipitation.

Load index is then derived from coverage accounting for other parameters as snow density, precipitation amount and times of shedding. This testing method is better expressed in a paper by Chemelli et al. [87]

Analysis of Load and Coverage indexes along with meteorological conditions gives very important insights on coatings' behaviour in real snowing conditions.

3.3.7 Real size samples (400m guard wire)

A 400m OPWG guard wire with Al SHP treatment has been exposed in November 2022 in Cencenighe Agordino . The earth wire has been produced by De Angeli. The sample has been mounted by TERNA personnel, spanning from pylon #18 to pylon #20.

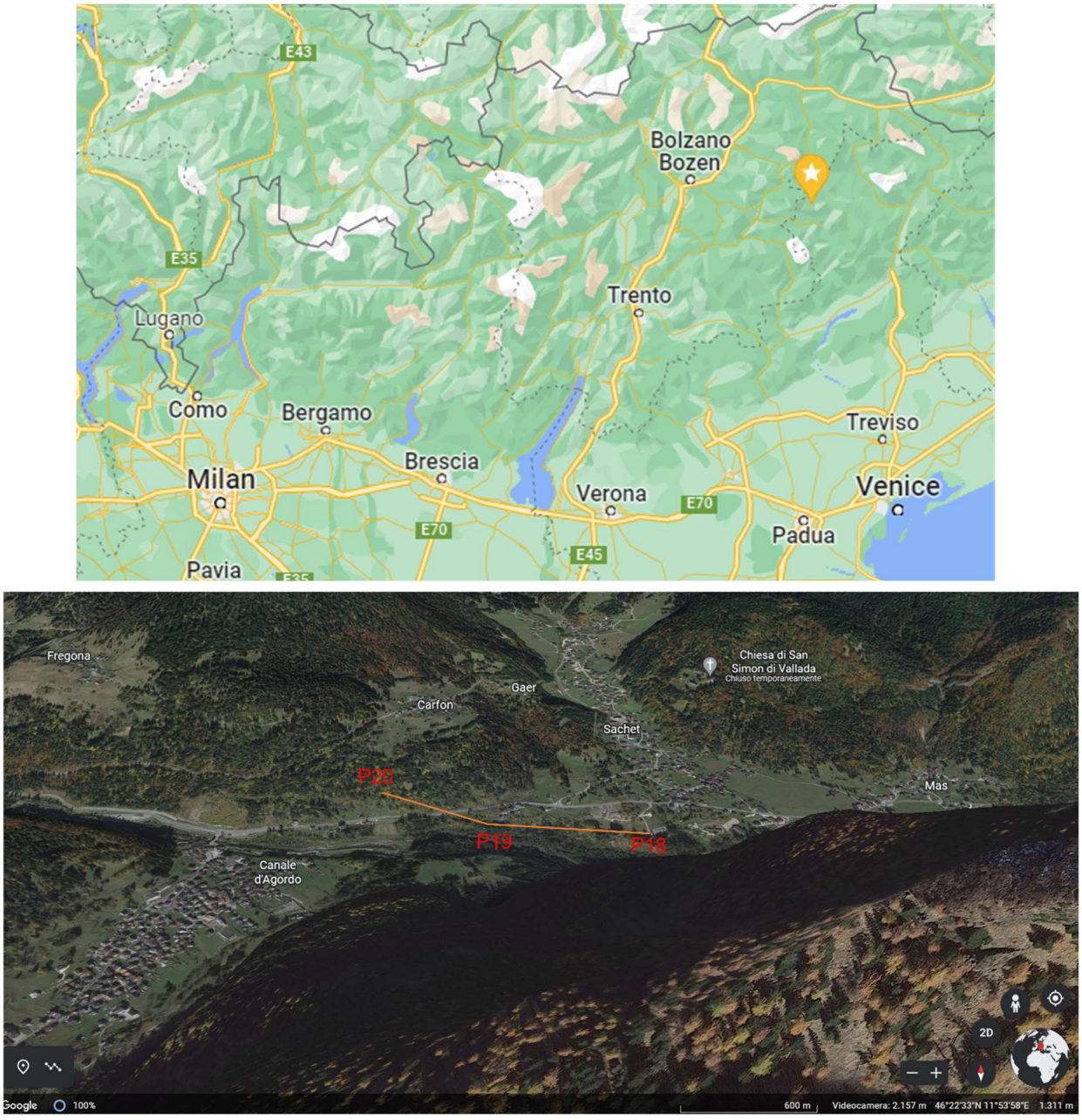

Figure 3.10 – Location of the test site

Samples will stay installed for at least two years. Data from the site will be acquired and transmitted by ELISAm system [88].The system is comprising of a NIR camera, optical targets, solar panels, battery and transmitters. One optical target per wire gives information about cable rotation and sag and snow sleeve accretion. The camera acquires pictures with and without IR flash to obtain two pictures from which the target is isolated by subtraction (targets are the only visible feature in a black background after image subtraction). From this, rotation and decrease in the area of targets indicate that a snow sleeve is growing

around the wire. The system is self-sufficient with solar panel and batteries. Two systems have been installed on pylon #19: one looking up to #20, one looking down towards pylon #18. In this way 3 conductors and 2 guard wires for each side are in the frame at any time. Results from winter 2022-2023 will be used as a stepping stone for a longer and profound analysis.

3.4 Materials and sample preparation

3.4.1 Laboratory samples

3.4.1.1 Al samples

Al samples have been purchased from Hobbymetal in form of 100x100x2mm sheets which have been later cut into 50x50mm or 20x50mm coupons.

Before applying a coating or going through a surface treatment, Al was cleaned with a basic soap in an ultrasonic bath, washed with demineralized water and dried with a paper cloth.

3.4.1.2 ZPS samples

ZPS have been purchased in 100x100x1mm sheets from Hobbymetal. Sheets have been later cut in 20x50mm coupons and sandblasted to both remove passivated layers from the surface and to create a micro roughness that is exploited for SHP surfaces. ZPS samples were cleaned with a water/acetone 50:50 mixture in a ultrasonic bath then rinsed with demineralized water.

3.4.1.3 Glass samples

Glass have been used in form of micro scope glass slides (75x35x1mm). Samples have been immersed in a 20g/L NaOH water solution for at least 2h to activate the glass, then washed with abundant demineralized water and dried with a nitrogen flux. Drying with nitrogen allows to visually identify any leftover NaOH on glass surface, which is then removed with demineralized water.

3.4.1.4 Large scale samples

Larger samples as insulators, guard wires and conductors have been prepared with treatments as close as possible to the above mentioned methods.

The 400m Al guard wire has been treated by De Angeli in their production site in Bagnoli,Padua, Italy.

3.4.2 Coating techniques

3.4.2.1 Dip-coating

Dip-coating is used to obtain thin films of coating upon a sample. Samples are dipped in a liquid and extracted at a defined speed, then the solvent is allowed to evaporate. Thickness of the coating can be calculated following the equation:

$$h = \left(\frac{\eta v}{\rho g}\right)^{1/2}$$

Where h is film thickness, η is viscosity, V is linear velocity of extraction, ρ is liquid density. This technique has been used mainly to obtain very thin films of hydrophobic molecules on micro-nano structured samples.

In practice, samples are hung from a vertical linear motion cart and dipped in a solution contained in a appropriately sized container at a speed of 0.6 mm/s, left idle for 2 minutes and then extracted at the same speed. The coating material is often in a solution of a volatile solvent (typically 1-5% conc. In EtOH) so to obtain thinner films after evaporation.

3.4.2.2 Spray coating

Spray coating is particularly suited for large scale samples.

A pressurized sprayer has been used throughout all experiments (Burkle pressure sprayer). Typically it was filled with a solution of coating material which was sprayed on the samples from 25-30 cm of distance. Some confrontations have been conducted to assess the possibility to use spray coating in substitution to dip-coating when preparing large samples.

3.4.2.3 Brush coating

Brush coating was used for very viscous coatings (e..g. silicones) and large samples. Some locally purchased paint brushes has been used throughout all experiments. When being brush coated, 75cm samples have been kept in a slow rotation so to avoid oozing of the coating.

3.4.2.4 Spin coating

Spin coating is a technique used to apply a layer of coating on a flat specimen. this is a widely used technique and very suited for fine tuning coating thicknesses. The following equation reports h in function of experimental parameters ρ for liquid density, ω for angular velocity and η for viscosity in terms of time t:

$$h = \frac{h_0}{\left(1 + \frac{4\rho\omega^2}{3\eta} h_0^2 t\right)^{1/2}}$$

Typically, samples have been spun at 200-500 rpm ,depending on viscosity, for 1 minute.

3.4.2.5 Manual tape casting machine

A simplified tape casting machine has been built in our laboratory. It has been used to prepare samples to assess the differences between different thicknesses of elastomeric coatings. It consists of a moving head with a blade mounted on it. Blade height can be tailored to need via a micrometric head equipped with a spring. A 3D printed plate with a cavity and a tailpiece allows a vacuum tube to keep the sample firmly mounted when the coating is spread.

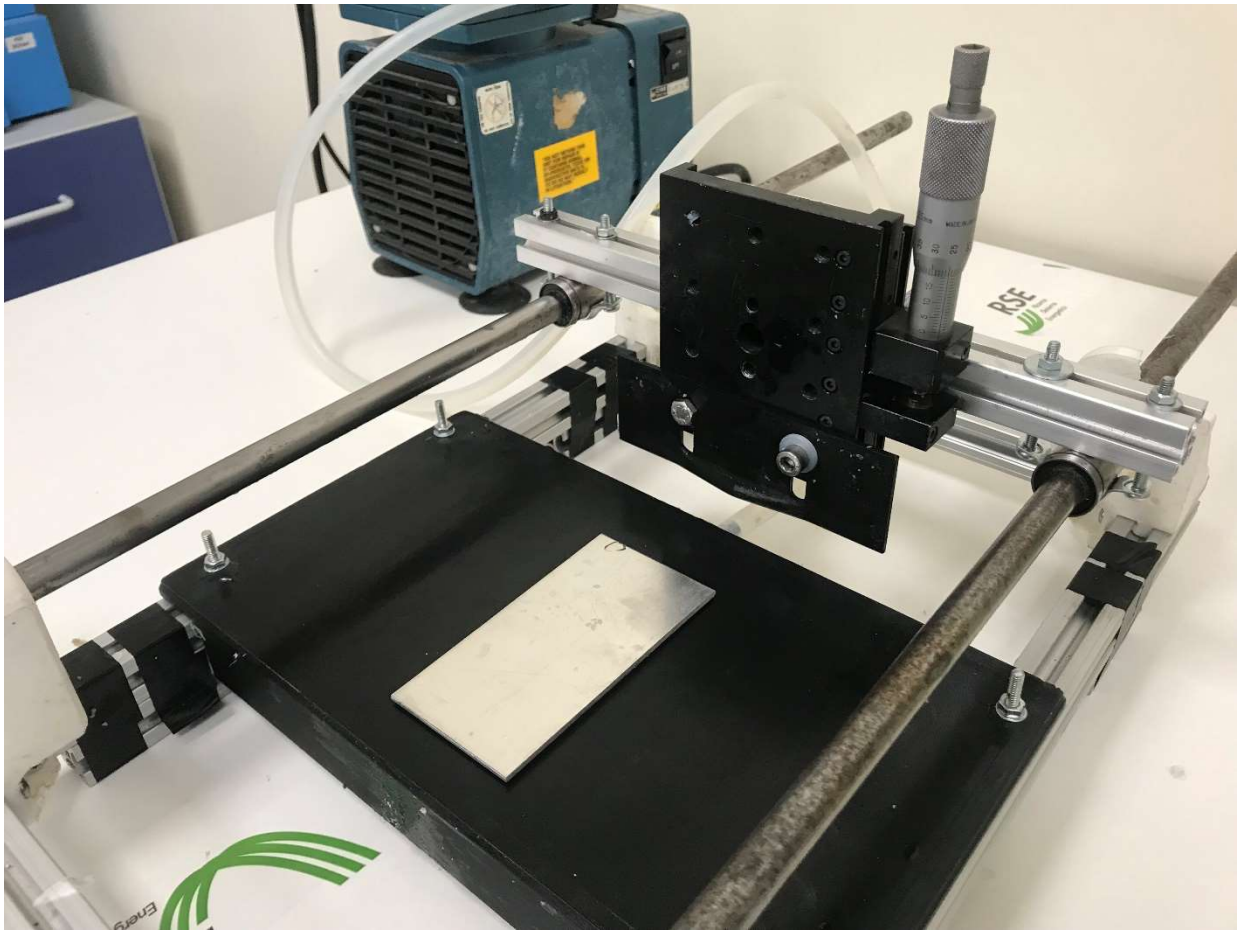

Figure 3.11 – Manual tape casting machine with vacuum pump.

Typically, a flat specimen is mounted on the vacuum slot, then the blade is laid flat and zeroed on the samples' surface and then the coating height is set with a micrometric screw gauge. Coating is then applied on a side of the sample and then the moving head is moved across the sample at a constant speed.

Some tests have been conducted on the reproducibility of this technique with satisfying results (max 15% variation between samples). Height of the so-deposited coatings have been calculated by subtraction to the uncoated sample' height.

3.4.3 3D printer

A Ultimaker 5S has been used to produce all the 3D printed parts reported. CAD files have been produced with Fusion 360 software. Ultimaker Cura slicing software has been used to convert stl files to gcode language. Stl format is a triangulated mesh which is used to import files in a slicing software, which converts geometrical features in discrete movements of the nozzle and other information such as material

extrusion and temperature controls in the form of gcode. A slicing software translates 3D shapes in multiple 2D layers which are additively built one upon the other by the machine. Any solid object is rendered with an external shell of solid and continuous material containing an infill of different percentage.

Ultimaker ABS and Tough PLA 2.75mm filaments have been used following the settings reported in the table below.

Table 3.4- 3D printing parameters for PLA and ABS

Material	Nozzle temperature (°C)	Bed temperature (°C)	Cooling fan speed	Infill (%)	External solid layers
PLA	220	50-60	100%	15%	8
ABS	250	100	1%	15%	6

4 EXPERIMENTAL

4.1 SHP zinc oxide Nanorods for zinc plated guard wires

Research has been conducted on the preparation of SHP Zinc Plated Steel surfaces, typical of guard wires which are prone to severe snow accumulation, not being heated by Joule effect. Application of elastomeric coatings is also unadvisable because applying a thick, non-conductive coating could compromise their intrinsic use as lighting shield on power lines.

In this light, the application of a monolayer of hydrophobic material on a rough surface to create a SHP material has been regarded as the optimal solution.

Results on Superhydrophobic and Ice-phobic Zinc surfaces have been reported in [89].

Zinc plated steel plates, Zinc Nitrate, HMT (hexamethylenetetramine), Stearic acid, FAS, NaOH, have been used throughout all the experiments.

All the hydrothermal synthesis' have been performed by weighing the reagents and mixing them to demineralized water at ambient temperature. Solution was then heated in a stove, up to experiment temperature; ZPS samples have been cleaned as reported and then immersed in the heated solution for the desired time. Samples were then extracted from the solution, rinsed with DW and dried with a jet of nitrogen. Surface treatments have been applied by dip-coating where not specified.

4.1.1 Preliminary testing

In the first place, a set of four experiments was performed [90]–[93] to investigate different pH values, conditions and capping agents to obtain ZnO NR which could also be made superhydrophobic after coating with FAS. All samples have been hydrothermally treated at 70°C for 20h. The table below reports solution components for 100ml of DW along with CA and RO values collected after dip-coating with FAS and thermal treatment (120°C/1h). As the table shows, only samples 1-1-2 and 1-1-0 showed super hydrophobicity in this test. This can be attributed to the formation of well-structured NR on the surface as shown in the SEM images below. Roll-Off (RO) is reported instead of Tilt angle for SHP samples.

Table 4.1- Preliminary testing reagents in 100ml of DW

Sample name	$Zn(NO_3)_2$ (g)	Capping agent (g)	NaOH (g)	CA°	RO°
A	1	-	1,8	114,9 (1,9)	>90
B	0,5	0,5 (citric acid)	1	136,7 (3,6)	>90
1-1-2	1	1 (HMT)	2	167,7 (3,7)	<15
1-1-0	1	1 (HMT)	-	156,1 (17,3)	<15

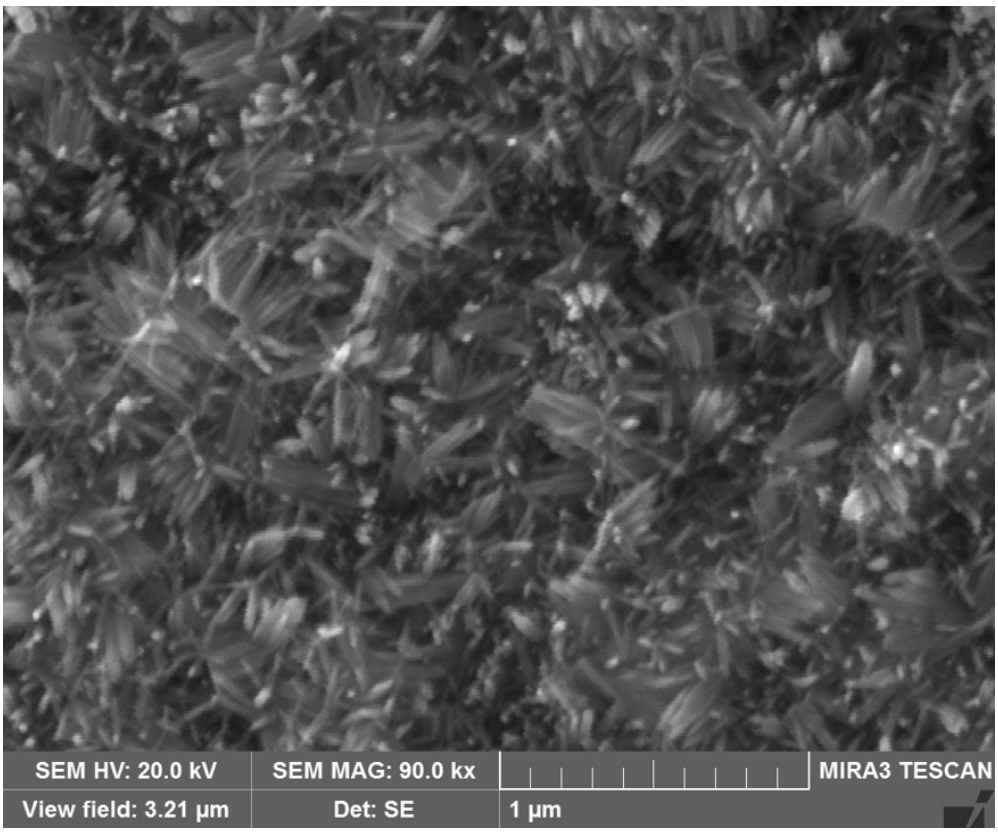

Figure 4.1 – SEM image (90kx) of a 1-1-2 sample

4.1.2 Sample nomenclature

All the so-formulated samples will be named after Zn nitrate, HMT and NaOH quantities in 100ml from now on, e.g. a 1-1-4 solution will contain 1g each of zinc nitrate and HMT and 4g of NaOH in 100 ml of DW.

4.1.3 Effects of treatment time and Temperature

Solutions 1-1-0 and 1-1-2 have been selected and the effect of time and temperature of hydrothermal treatment on CA and RO (after FAS coating) were investigated.

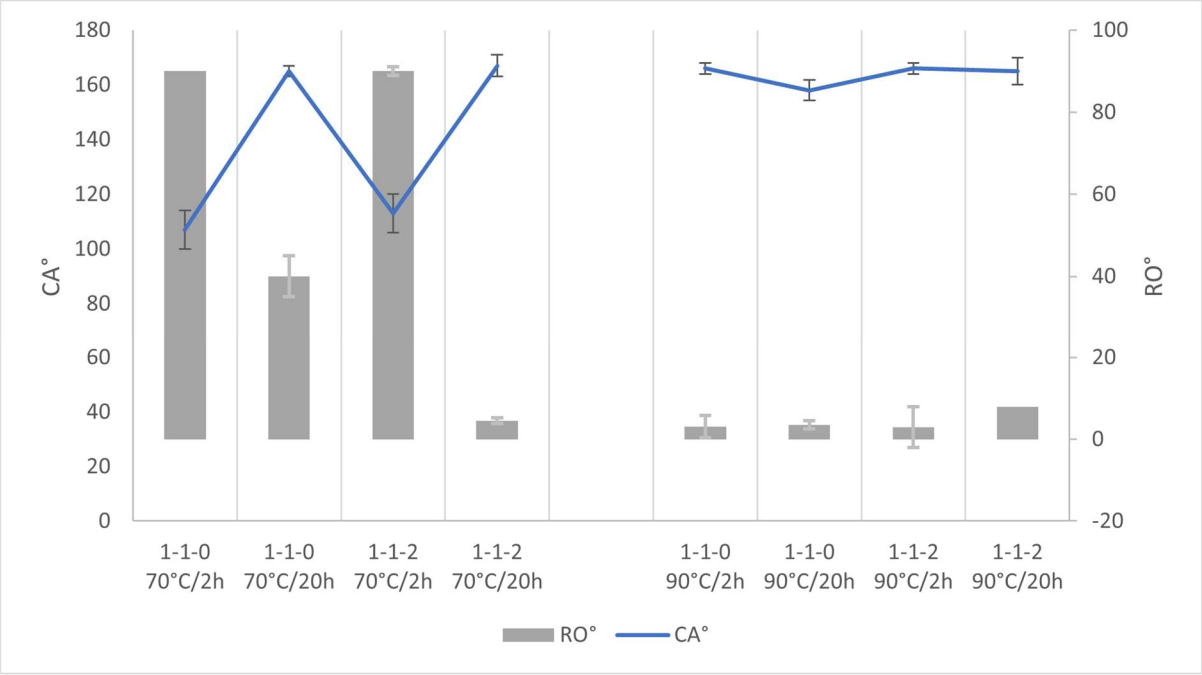

Figure 4.2 – Temperature and time of hydrothermal treatment for 1-1-0 and 1-1-2 growth solutions

Higher temperatures favour a faster formation of a surface roughness suitable to obtain SHP surfaces. In particular, samples 1-1-2 90°C/2h and 1-1-0 90°C/2h exhibit lower RO and higher CA than their 20h counterparts. This is probably due to an overabundance of NR forming upon the surface for long treatments which can be detrimental in terms of SHP properties, as can be seen in the SEM pictures below.

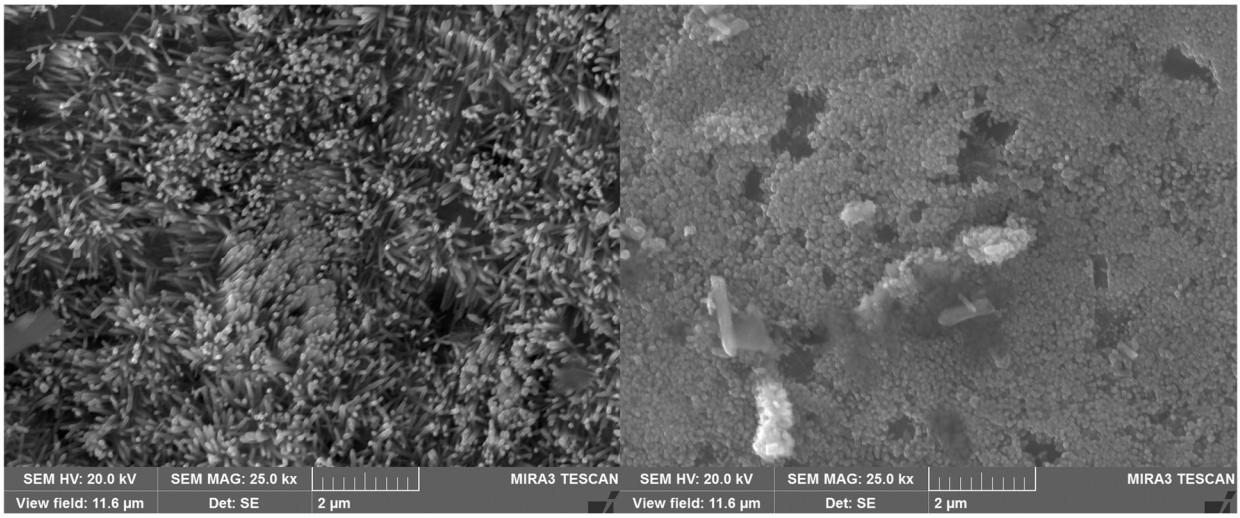

Figure 4.3 – SEM (25kx) of 1-1-2 90°C samples treated for 2h (left) and 20 hours (right)

4.1.4 Decreasing treatment time

Shorter times have been investigated. A minimum time of 15' for 1-1-2 solutions and 60' for 1-1-0 solutions have been found. Reducing times further do not yield the onset of SHP properties. As seen from SEM images, some initial formation of ZnONR is present after 5 minutes of treatment, but it is not comparable in abundance to 15' samples.

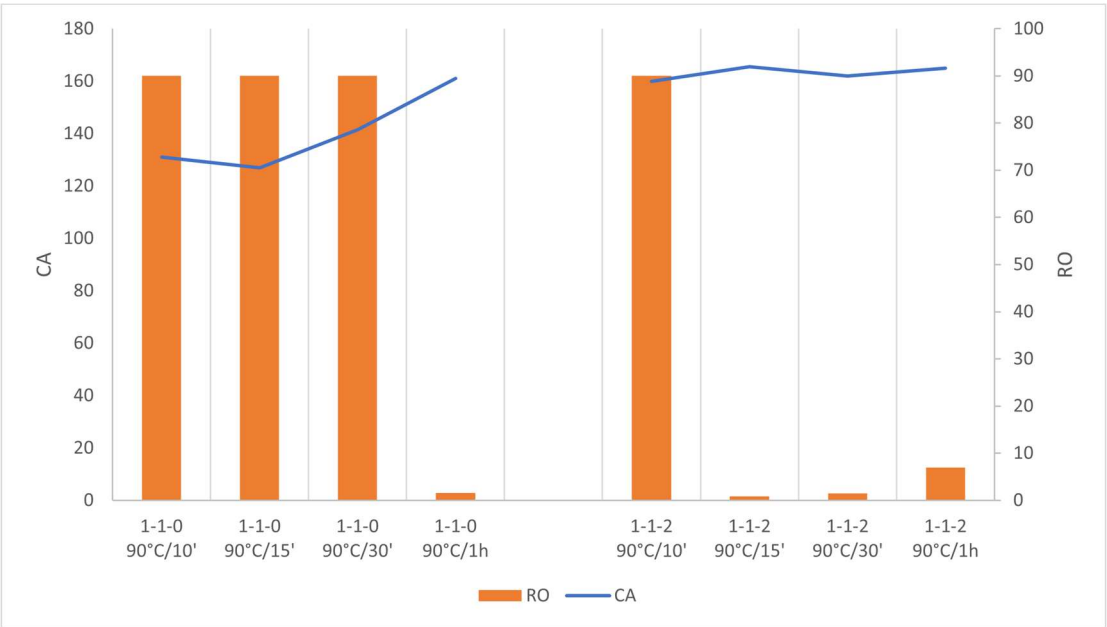

Figure 4.4 – CA and RO for <1h 1-1-0 and 1-1-2 90°C treatments

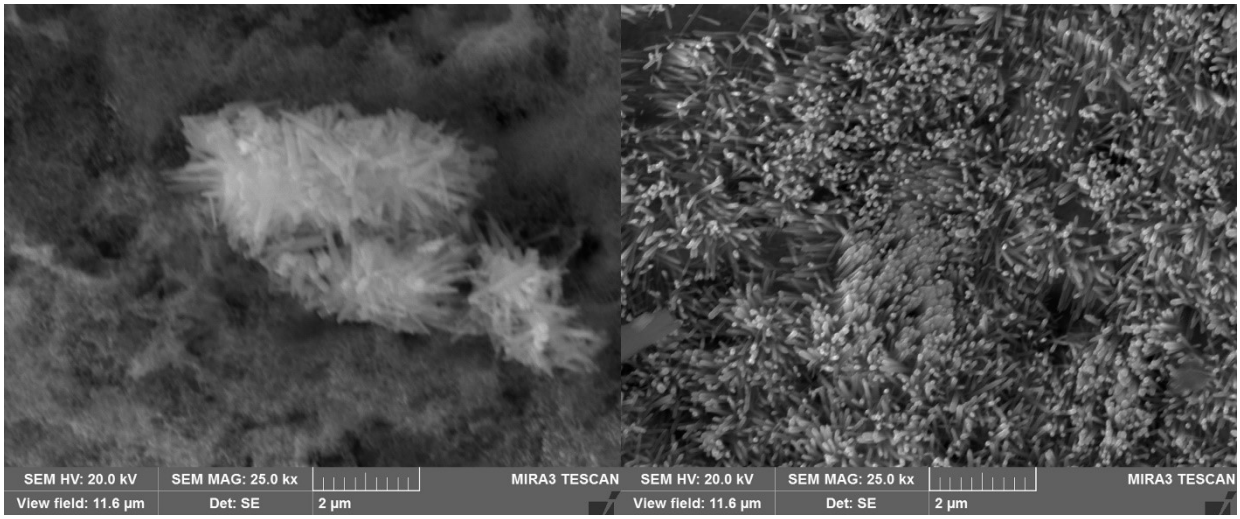

Figure 4.5 – SEM (25xk) images of 5' and 15' 1-1-2 90°C samples

4.1.5 Effect of pH on ZnO NR growth time

The time of hydrothermal growth for ZnO NR has proven to be a function of pH . Higher NaOH concentrations leads to shorter SHP onset times, e.g. the 1-1-01 samples showed SHP properties (CA>160°, RO<10°) after 30' of treatment whereas a 1-1-4 formulation could reduce times to 10'. Still, NaOH concentrations higher than 4g/100ml have not been further investigated due to the fact that steel in samples showed evident signs of oxidation even after a <10' hydrothermal treatment.

4.1.6 Non-fluorinated coating

The aim of the research has then moved from obtaining a suitable micro-nano structure to testing non-fluorinated solutions for coatings. Stearic acid (STA) have been investigated due to its very low toxicity, low price and hydrophobic properties. Several STA concentrations, solvents and immersion times have been investigated. Literature reported STA concentrations in the range of few mM. [94]

The table below shows how SHP properties appear in function of time of solvent, immersion time and concentration on 1-1-2 90°C/30' samples. After immersion samples have been treated at 120 °C/2h.

Table 4.2- presence of SHP properties for different STA concentrations, solvents and times of immersion

Solvent	STA concentration	Immersion time	Presence of SHP properties
EtOH	10mM	1h	
		6h	
		24h	X
Acetone	2mM	4h	
		24h	X
	10mM	30’	X
		4h	X

From the successive characterizations, 10mM STA in acetone solutions have been chosen to impart hydrophobicity on ZnONR samples. Time of immersion have been set to 30’ and following heat treatment to 120 °C/2h.

4.1.7 Hydrophobicity results

For the sake of simplification, 1-1-2 90°C hydrothermal treatments have been used in all the following sets of experiments. Thus, samples are reported as STA or FAS, indicating the type of hydrophobic coating applied, followed by time of hydrothermal treatment at 90°C , e.g. a STA-30 is a sample immersed in a 1-1-2 solution at 90°C for 30 minutes, dipped for 30’ in acetone then heat treated at 120°C for 2h.

The following graphs shows CA and RO results for STA coated samples compared to FAS coated ones for various durations of hydrothermal treatment. As can be seen, both STA-10 and FAS-10 samples show high CA but limited dynamic properties, whereas FAS-15 and STA-15 already have very low RO angles. Both FAS-30 and STA-30 have the lowest RO.

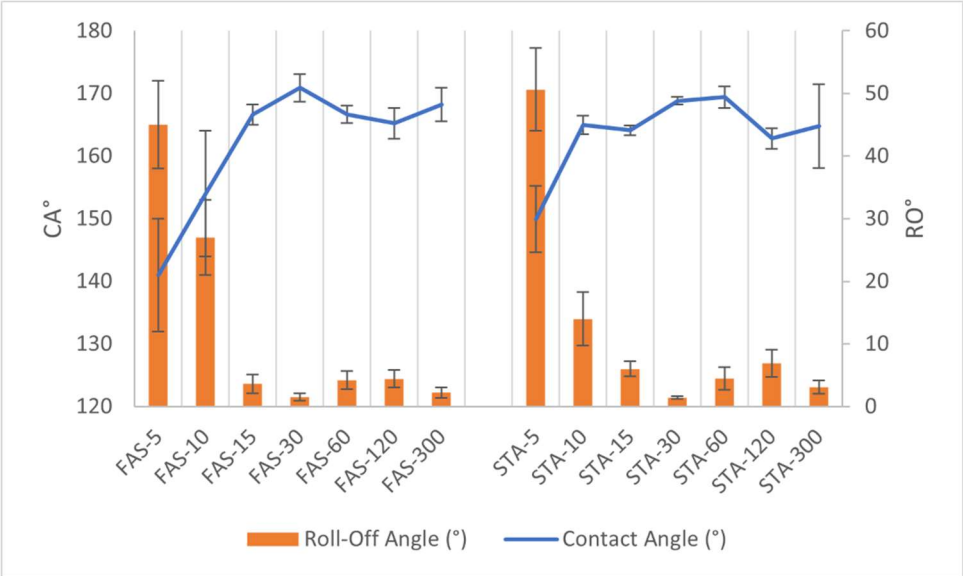

Figure 4.6 – CA and RO for STA and FAS 1-1-2 samples with different times of hydrothermal treatment

4.1.8 Surface Free Energy

Characterization of Surface free energy has also been performed on these samples.

As reported in the table below, FAS is showing lower SFE than STA due to their per fluorinated molecule tails. Even if the difference in total SFE is not negligible, FAS and STA both report very low, and comparable, polar contributes; this feature indicates how STA is a suitable hydrophobicizer for micro-nano structured samples.

Table 4.3- Surface Free Energy for bare ZPS, FAS-0 and STA-0 samples.

Sample	SFE (mN/m)	Disperse (mN/m)	Polar (mN/m)
Bare ZPS	62.6(7.4)	41.3	21.3
FAS-0	14.8(2.4)	14.6	0.2
STA-0	25.9(10.1)	25.4	0.5

4.1.9 Ice adhesion testing

To compare the effect of FAS and STA coatings in terms of icephobicity and to relate them with contact angle and SFE, ice adhesion properties characterization have been then performed. Since ice in the cuvette used for testing didn't adhere at all to the samples' surface, samples FAS-15, FAS-30 and FAS-60 shear stress' of ice adhesion have been reported to be <10kPa, a rounded-up value of the force needed to just push away the cuvette itself.

The following graphs show results of ice adhesion testing, indicating a very low ice adhesion for both STA and FAS samples hydrothermally treated for more than 15 minutes and a strong correlation between ice adhesion and RO angles. It is also shown that CA alone cannot be as good as a direct indicator of low ice adhesion, e.g. for FAS-10 and STA-10 samples.

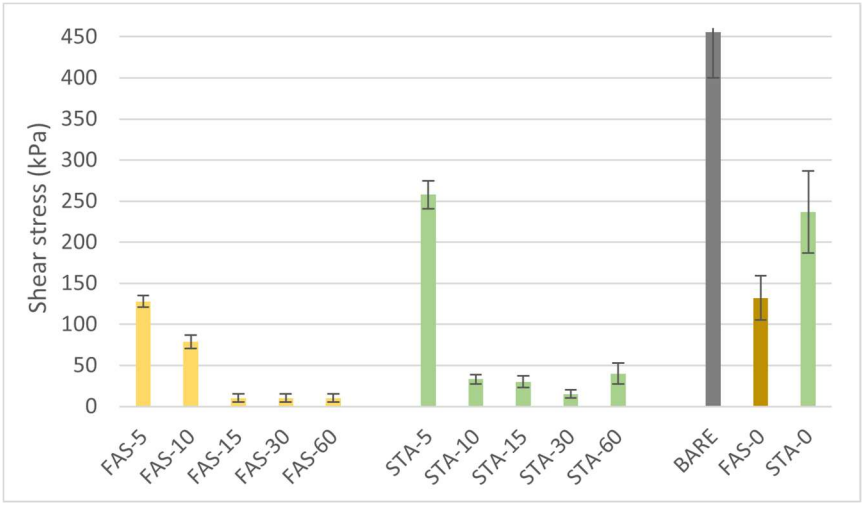

Figure 4.7 – shear stress of ice adhesion for FAS and STA samples with different treatment durations

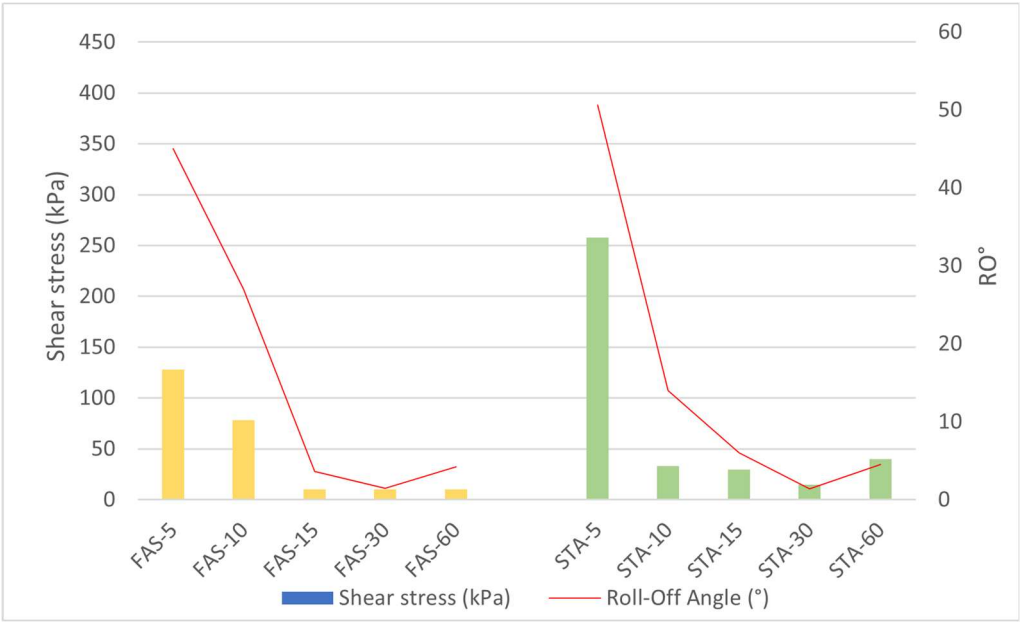

Figure 4.8 – Roll-Off angles and shear stress of ice adhesion for FAS and STA samples

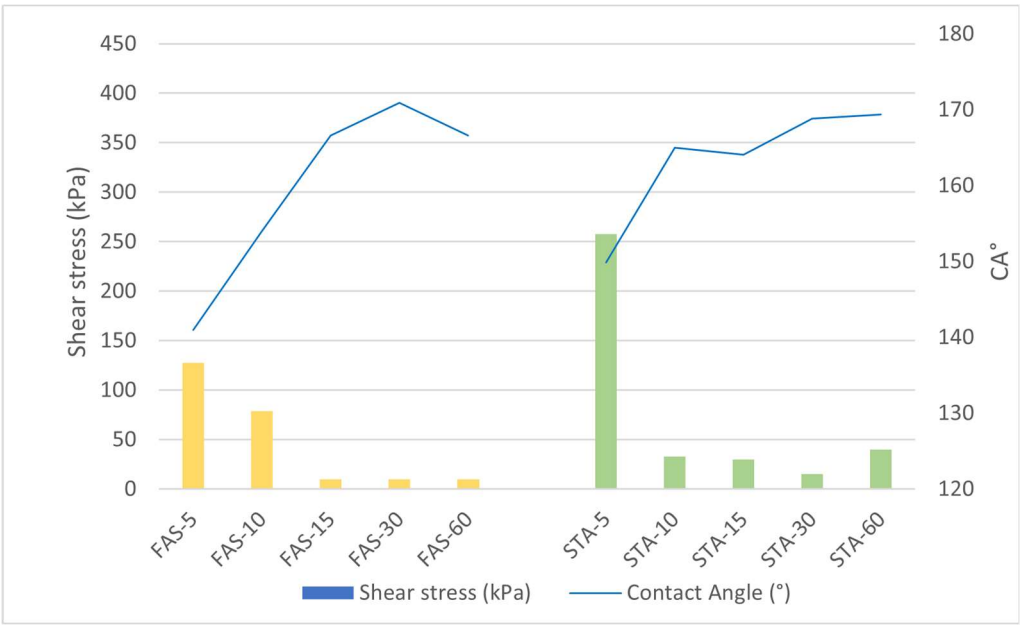

Figure 4.9 – Contact angles and shear stress of ice adhesion for FAS and STA samples

4.1.10 Ice nucleation temperature

Ice nucleation temperature has been measured, showing a heavy effect of SHP ZnO NR. This can be due either to air in the micro-nano structure being insulative or to a low nucleation potential of the samples.

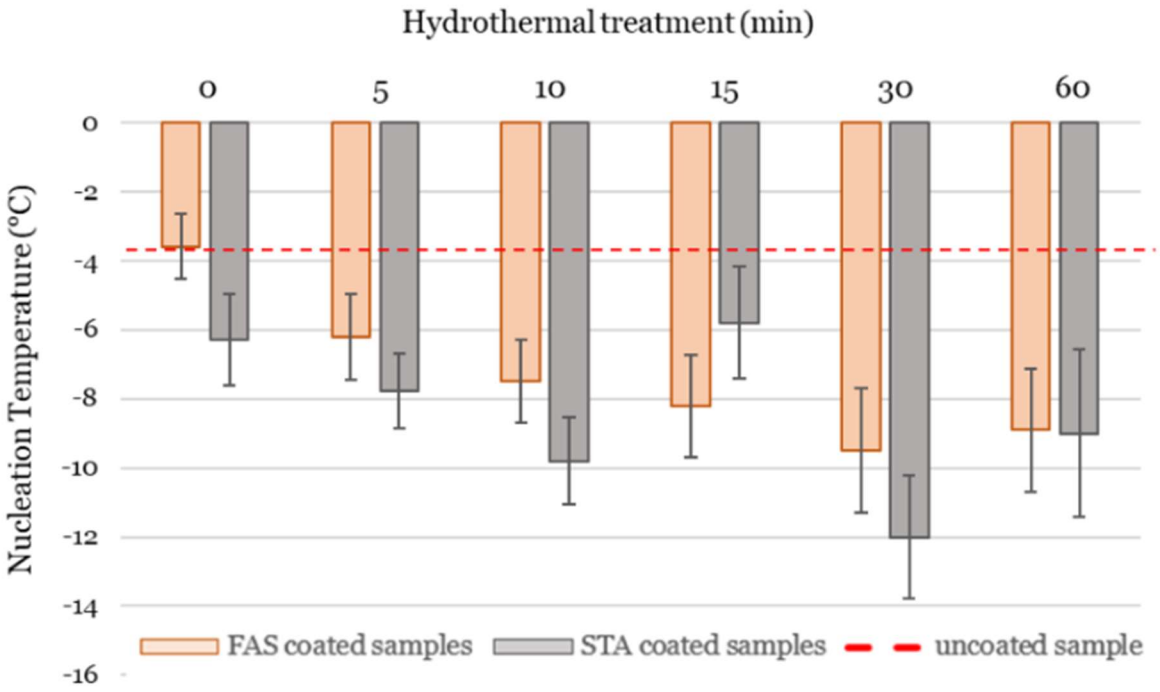

Figure 4.10 – Nucleation temperaturs for FAS and STA samples

4.1.11 Adhesion Reduction Factors

To sum-up, the anti-icing results of surface treatments on ZPS are reported. Evidently, the presence of a well-formed micro-nano structure, as for FAS-30 and STA-30 samples, imparts a 10-fold reduction of ice adhesion in respect to bare ZPS surfaces with a hydrophobic coating, as FAS-0 and STA-0. This is evidently due to the SHP properties of ZnONR on their surface.

Table 4.4- Adhesion reduction factors for STA and FAS samples

Sample	ARF	Sample	ARF
STA-0	1.9	FAS-0	3.5
STA-5	1.8	FAS-5	3.6
STA-10	13.8	FAS-10	5.8

STA-15	15.2	FAS-15	>45
STA-30	30.4	FAS-30	>45
STA-60	11.4	FAS-60	>45

4.1.12 Durability testing

Durability testing has been performed on STA-30 and FAS-30 samples, which have been left immersed in three different aqueous environments: acid (acetic acid, pH=3), basic (NaOH, pH=8.5) and saline (NaCl, 35 g/l). CA, RO and ice adhesion properties have been recorded after up to 30 days of aging.

4.1.12.1 SEM/EDX characterization

The morphology of the aged samples was checked by SEM analysis: the image of the FAS-30 aged in saline solution for 30 days is reported as representative of all samples. With respect to the non-aged sample, the hierarchical structure is less visible. EDX analysis showed a significant reduction in both Si and F in the coating (F from 3.1(0.8)% to 0.9(0.3)%, Si from 0.7(0.1) to 0.5(0.1)) meaning a partial degradation/unbonding of the coating.

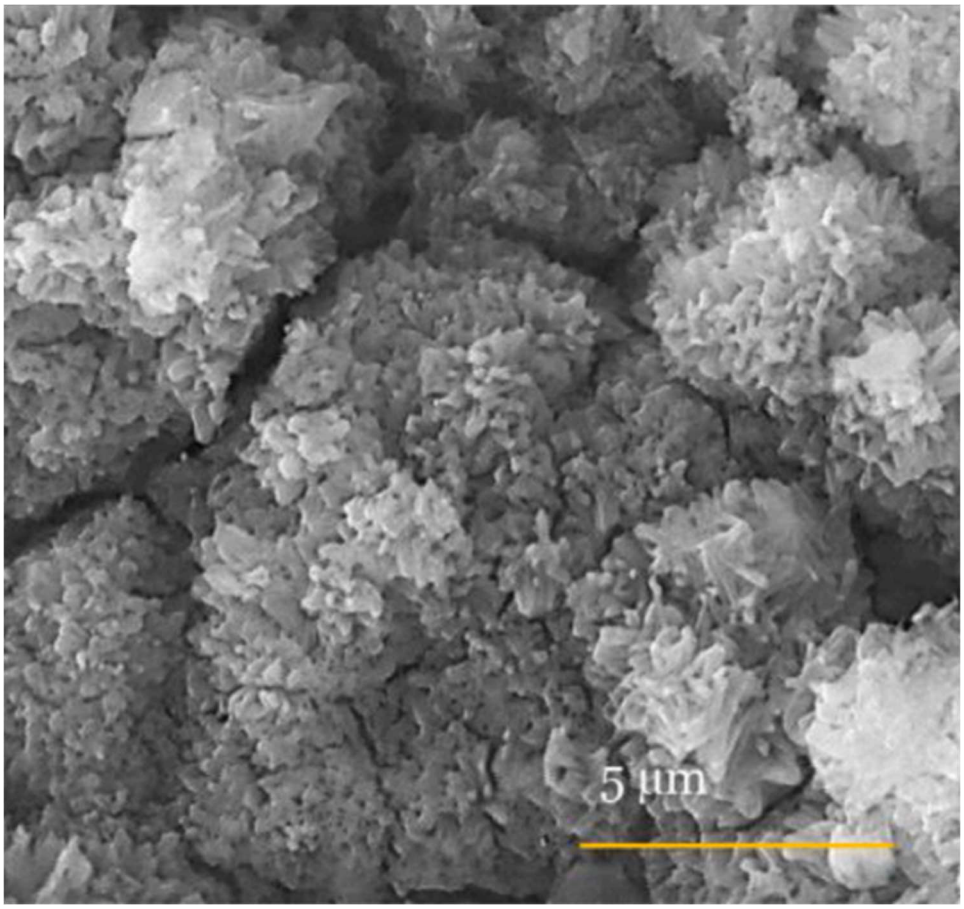

Figure 4.11 – SEM image of a sample aged in wet chemicals for 30 days.

4.1.12.2 Contact angle

In general, both the tested coatings evidenced an initial degradation of the WCA that stabilizes after 7 days. In contrast with some works in literature [95], the FAS coated samples showed a higher deterioration of the WCA than the STA coated specimens. The tilting angles, listed in the following image shows that all the FAS-30 samples completely lose their dynamic properties already after 7 days and this is a clue of deterioration of the surfaces. STA-30 samples evidence some differences among the different ageing solutions: in saline, STA-30 loses its dynamic property after 7 days of immersion, while in acid and basic solution is somehow preserved. Thus, in the applied conditions, STA-30 keeps better hydrophobic behaviour with respect to the fluorinated one. This can be a clue of the reversibility of chemical bonding between FAS and ZnO.

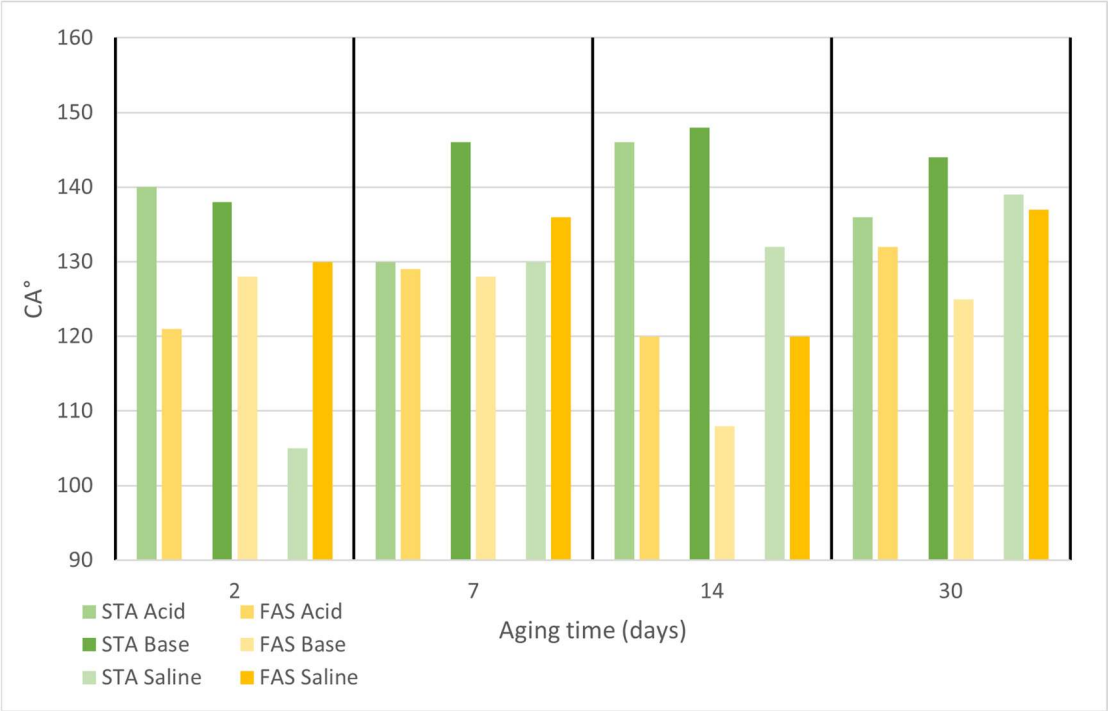

Figure 4.12 – Contact angles in function of aging time and environment

4.1.12.3 Ice adhesion

Shear stress analysis was performed on the FAS-30 and STA-30 samples previously aged in wet chemical solutions for 30 days. As expected, degradation of hydrophobic properties leads to lower ice-phobicity: ice adhesions of the aged samples are higher than those of the non-aged. However, it is important to underline that, after aging, the samples maintain a good ice-phobic behaviour, reducing ice adhesion from 2 to a maximum of 8 times, with respect to bare ZPS.

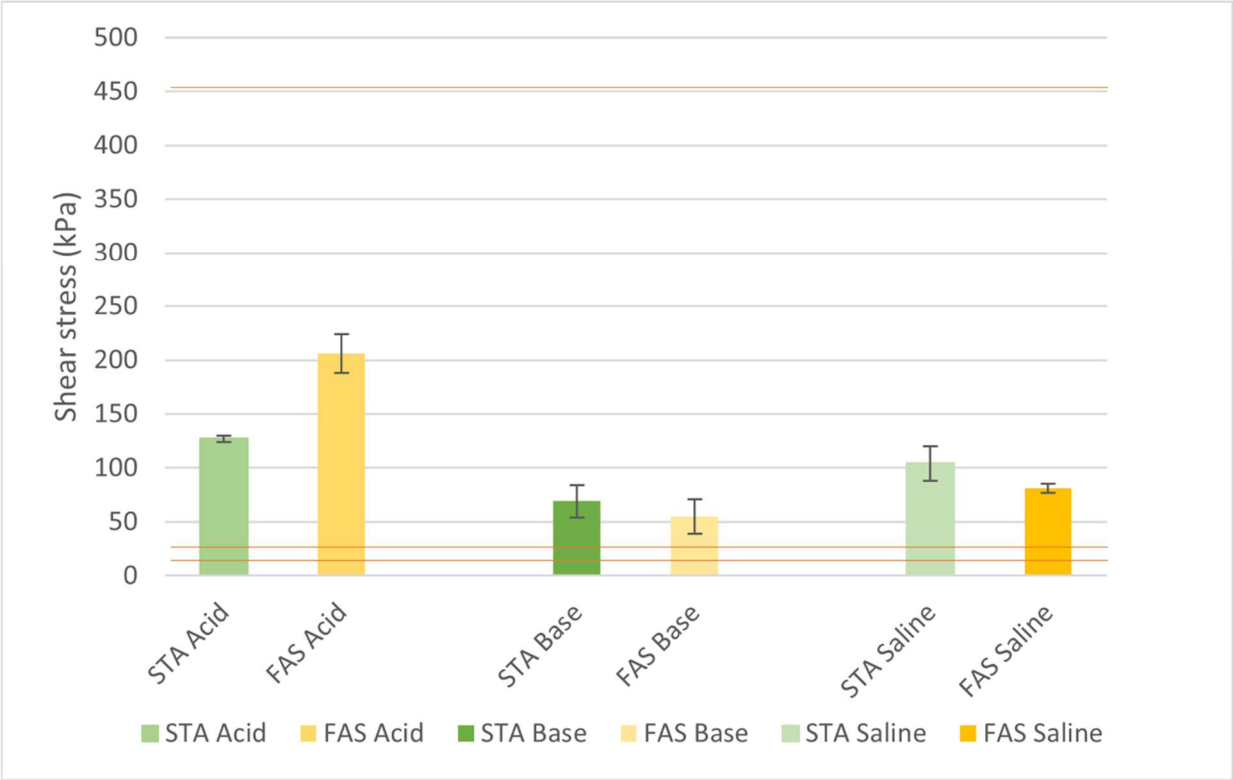

Figure 4.13 – Shear stress of ice adhesion after 30 days, lines in red are relative (from top down) to bare ZPS, STA-30 and FAS-30 for reference.

4.1.13 Properties recovery

To evaluate the feasibility of a fast restoration of ice-phobic properties, the aged samples were recoated in FAS and STA and cured at 120 °C for 1 h. Remarkably, the ice adhesion is lowered for all retreated samples leading in many cases to shear stress values lower than 100 kPa and very close to the original ones. It is thus demonstrated that most of the samples regenerated with this easy process obtain renewed ice-phobic performances.

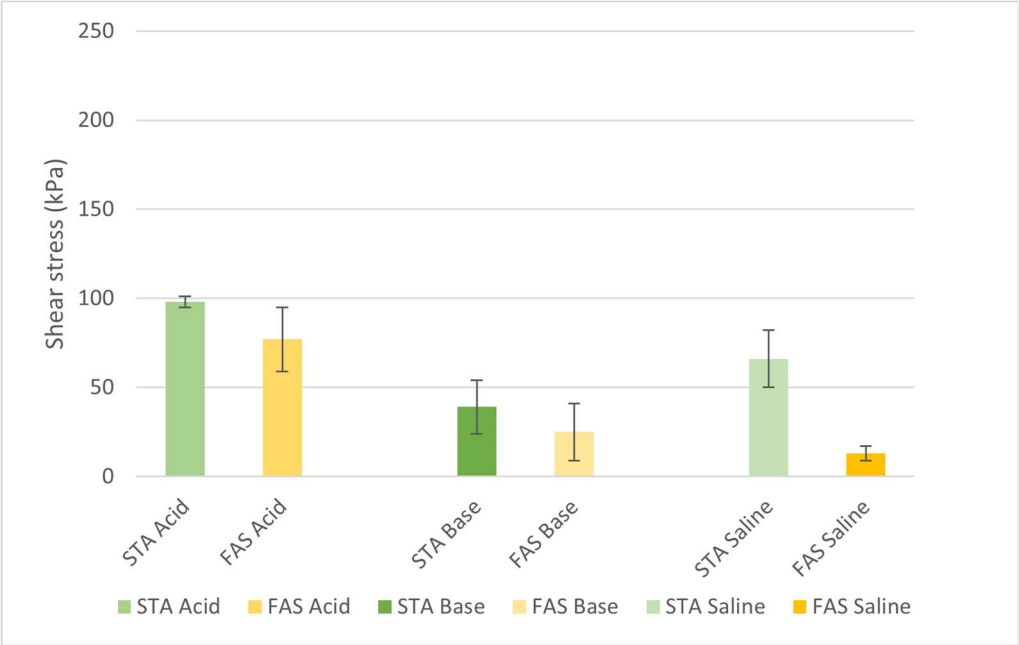

Figure 4.14 – Shear stress of ice adhesion after 30 days of aging and recoating of samples.

Table 4.5- Adhesion reduction factors for 30days aged and re-coated STA and FAS samples

ARF	New	30d Acid	30d Acid recoated	30d Base	30d Base recoated	30d Saline	30d Saline recoated
FAS-30	45	2,2	5,8	8,1	18	5,5	34,6
STA-30	30	3,5	4,6	6,5	11,5	4,3	6,8

4.1.14 Spray coating tests

STA solutions in acetone have been also applied by spray coating from a distance of 15-25 cm from the surface of the samples, followed by the usual heat treatment at 120°C for 2h. CA and RO angles have been measured and no noticeable differences from the reported preparation where evidenced (CA=165°(3), RO=4°(1)). Application by spray coating is particularly useful when aiming at a large scale application of this kind of coating, cutting out the immersion step, which can be difficult to perform on long spans of wire.

4.1.15 ZnO NR growth solution durability

Shelf life of solution have been evaluated, and no noticeable differences have been noticed when samples were prepared with a three month old solution.

Repeated tests were also conducted to assess growth solution durability. More than 100 samples have been prepared with the same 100 ml of 1-1-2 solution without any relevant degradation of CA and RO properties of samples after FAS or STA treatments. This result is encouraging for large scale applications.

4.1.16 Large scale samples

4.1.16.1 WILD station: 15m samples

Large scale samples have been also prepared. A long span of wire have been treated in 5 liters of 1-1-2 solution in a heated container (it is important to heat the guard wire to at least 80°C before putting it in the hydrothermal bath in order to maintain temperature as stable as possible). FAS coating have been applied via brush-coating on this sample, followed by the usual 120°C/2h treatment. A FAS-30 15m rope have been prepared this way and exposed in the WILD station in Vinadio,Italy during 2021-2022 and 2022-2023 winters.

Results from 2021-2022 winter are promising. The sample have been left on site for 2022-2023 testing.

4.2 Elastomers

Elastomers have been studied starting from Sylgard 184 and Sylgard 186 kits from Dow chemicals. Both are two-component mixtures to be mixed in 10:1 ratios.

FT-IR characterizations show that part A is containing the vinyl moieties and part B the Si-H ones for both of the elastomeric kits.

4.2.1 Sylgard PDMS 184 and 186

4.2.1.1 Anti-icing characterization

Sylgard PDMS 184 and 186 anti-icing properties have been tested with ice adhesion testing machine.

The elastomers have been deposited on Al substrates via spin-coating and then heat treated at 120°C for 2h to allow the two components to react.

Syl 186 presents a lower ice adhesion in respect to Syl 184. Further characterization have been conducted to assess which property could be addressed as responsible for these different behaviours.

4.2.1.2 Contact angle, tilting angle, SFE, Young moduli

Other properties of Syl 186 and Syl 184 are reported hereafter.

Since the difference between CA, Tilt Angle and SFE between the two samples is negligible and showing a slightly more hydrophobic behaviour of Syl 184, Young moduli of both have been tested with an AFM machine. Difference in Young moduli couldn't explain lower ice adhesion.

Table 4.6- CA, TA and SFE for Syl 184 and Syl 186

	Ice adhesion (kPa)	Contact angle (°)	Tilting angle (°)	Total SFE (mN/m)	Polar SFE (mN/m)	Disperse SFE (mN/m)	AFM Young modulus (MPa)
Syl 184	153 (25)	107(3)	48(4)	26,1(0,3)	25,9(0,1)	0,2(0,2)	2,46
Syl 186	91(9)	100(1)	56(7)	25,4(2,8)	25,1(2,5)	0,3(0,3)	2,64

4.2.1.3 Viscosity and setting time

The ongoing reaction between the elastomer components have been tracked by monitoring its viscosity.

A+B Syl 184 and Syl 186 mixtures have been prepared and kept at a constant temperature.

Samples have been analysed ranging from 0.3 to 100 RPM with a rotational viscometer.

4.2.1.3.1 Syl 184 Viscosity

Syl 184 showed a Newtonian behaviour until the mixture reached a critical point.

The onset of a non-Newtonian behaviour is evidenced by the transition from a linear viscosity regime to a power-law viscosity regime (Ax^n), with n indicating an index of “non-Newtonianity”.

Generally, values of n below 0 underline deviations from Newtonian behaviour in term of viscosity vs shear rate. In this case, this is also reflected by a transition of the growth of viscosity in function of time from a linear to an exponential regime.

This steep increase in viscosity around 5 hours after mixing the two components and starting the hydrosilylation reaction is strongly indicating the formation of a very interconnected network of molecules.

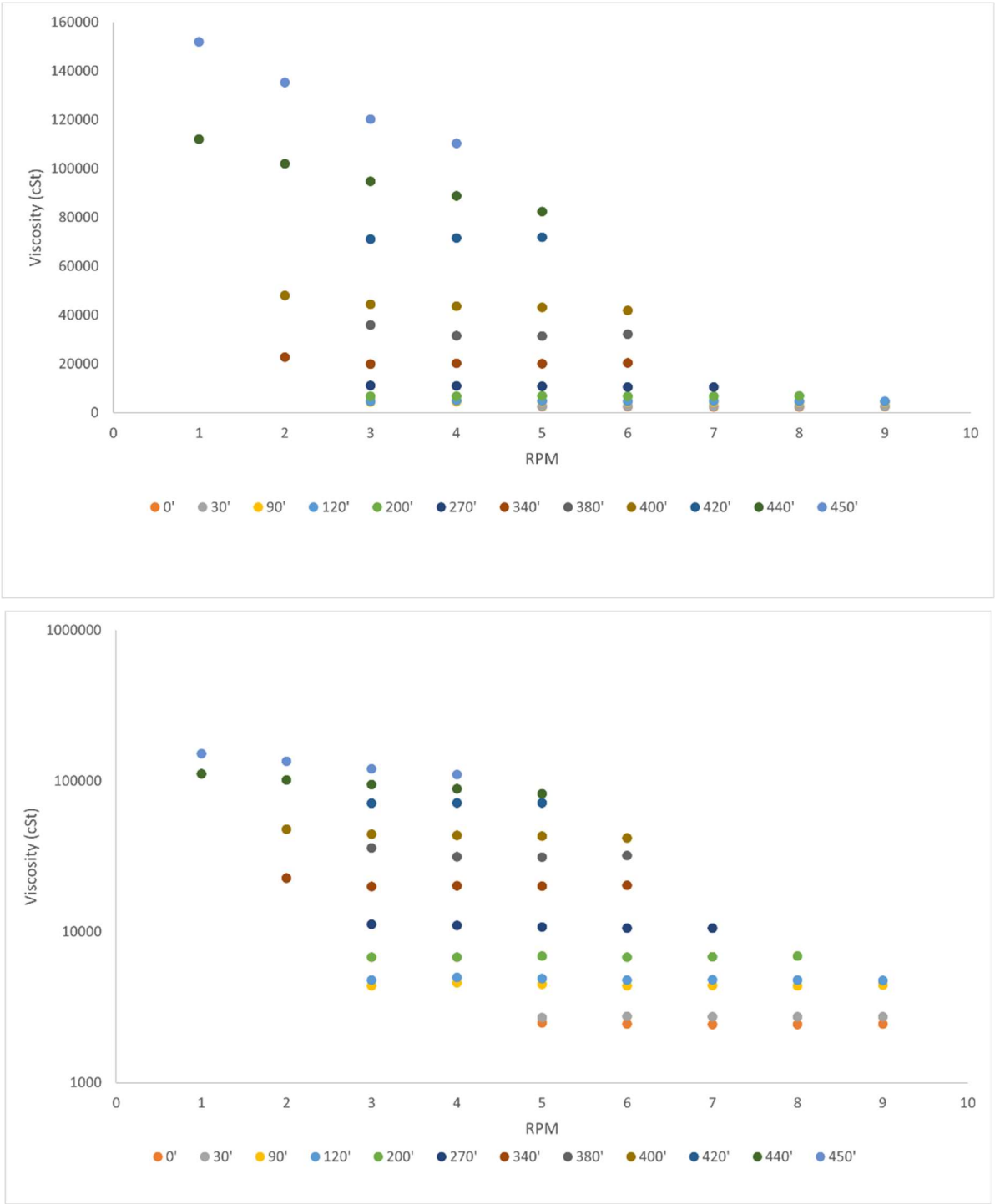

Figure 4.15 – linear and logarithmic views of viscosity vs RPM for Syl 184 shown at different times

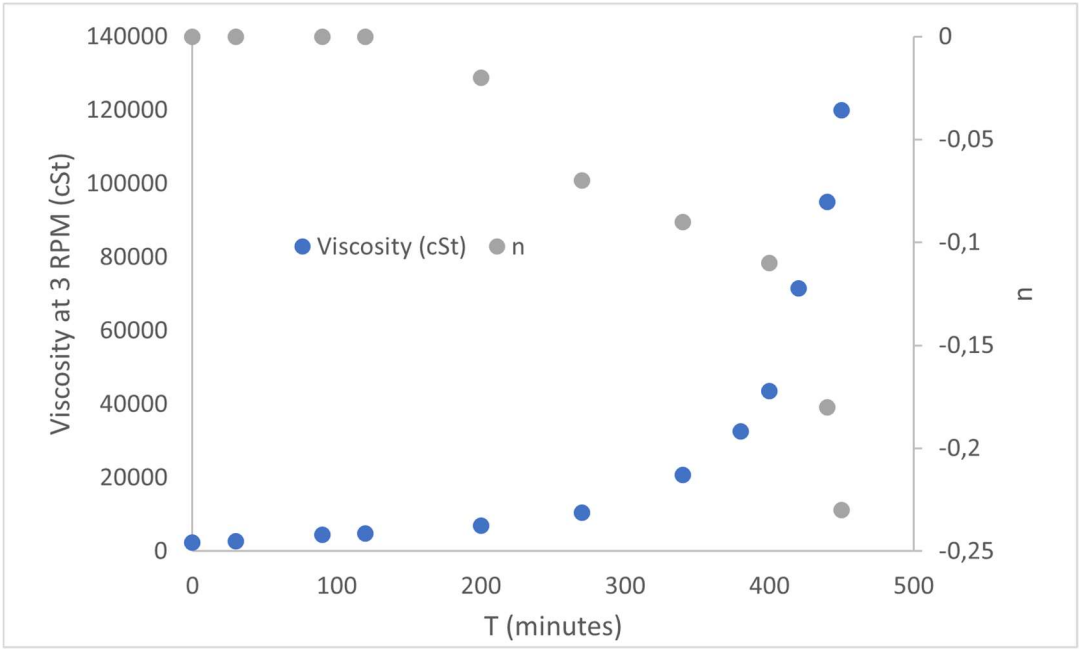

Figure 4.16 – Viscosity at 3 RPM and n vs. time

4.2.1.3.2 Syl 186 Viscosity

Syl 186 showed a non-Newtonian behaviour from t0. The A part of Syl 186 is non Newtonian itself.

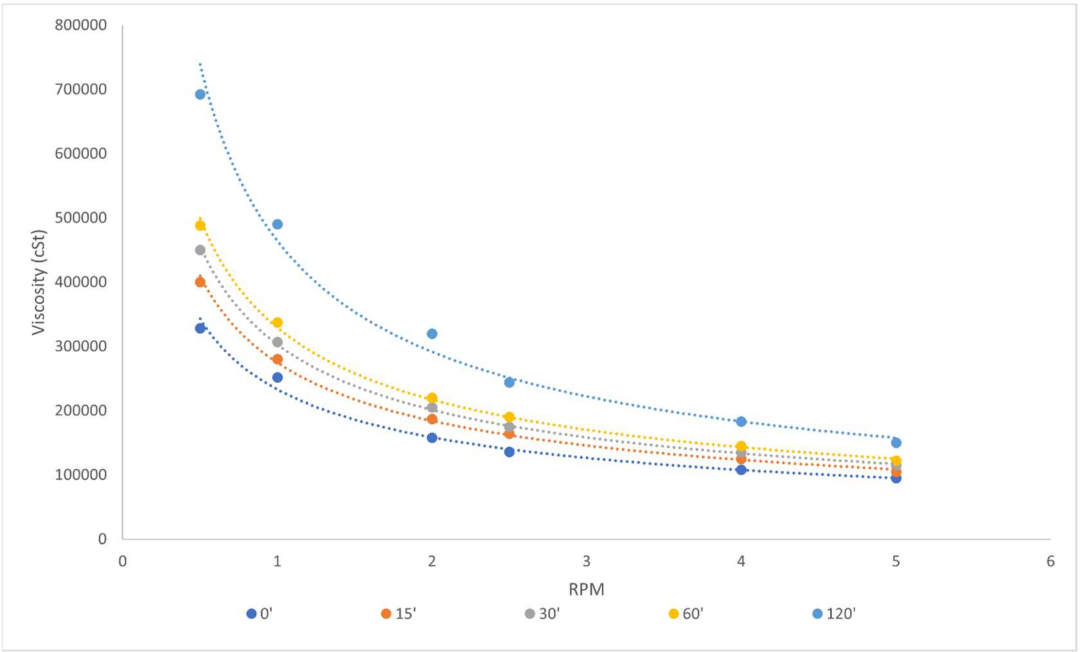

Figure 4.17 –viscosity vs RPM for Syl 186 shown at different times

Syl 186 exhibits values of n of -0,55 at 0’ raising to -0,67 after 120’, at the end of the workability window.

Aside a faster setting time, Syl 186 shows very different rheological features from Syl 184, not only in the evident difference in the thickness of the reagents, but also in terms of its response to external forces, especially gravity, when deposited on a sample. A more explicit non-Newtonian shear-thinning behaviour is preferable in terms of a large scale application, favouring its deposition with a brush or other methods while returning to a more viscous state when not subjected to stress.

4.2.1.4 Effect of film thickness and hardness

For Syl 186, some other ratios aside the usual 10:1 have been investigated, ranging from 5:1 to 30:1.

Different A:B ratios give elastomers of different hardness. In particular, low ratios result in harder final materials. This is due to the fact that for a fixed amount of vinyl moieties, having more cross-linking Si-H moieties allow a higher degree of reticulation.

Young moduli for 5:1 to 30:1 Syl 186 have been investigated with AFM and confronted with results of ice adhesion. Samples are deposited at 800 µm thickness.

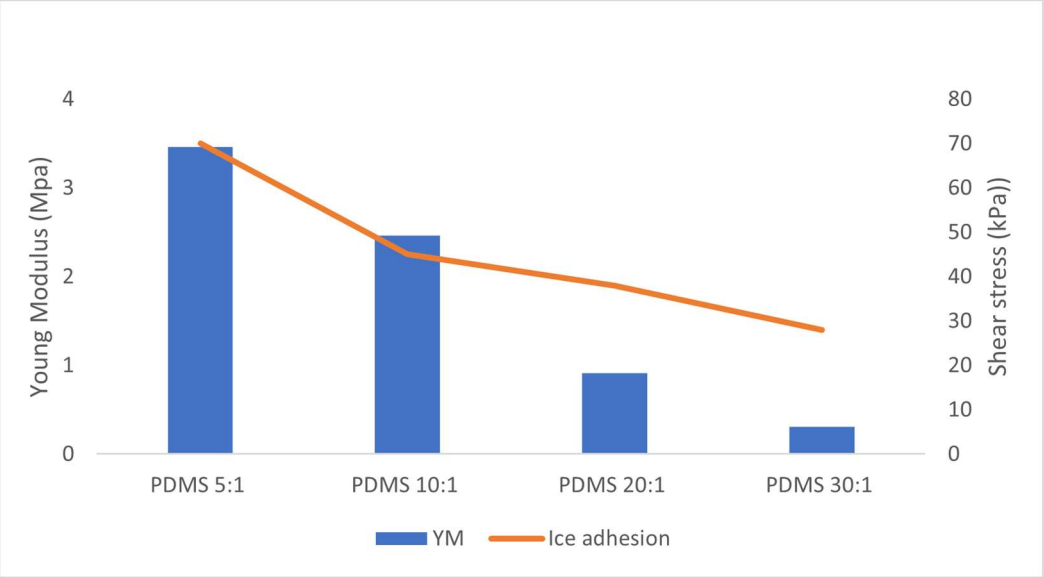

Figure 4.18 – Syl 186 film hardness vs. ice detachment for different A:B ratios

The effect of film thickness have also been tested.

Aluminum samples have been coated with Syl 186 of thickness ranging from 100um to 1200 um using the manual tape caster. Coating thickness after the elastomer turned solid have been measured. For the thinner coating a slightly higher final coating thickness is obtained, whereas for 800um and 1200 um samples a viscous collapse of the still liquid PDMS is seen, resulting in thinner final coatings.

Samples show an expected decrease in ice adhesion in function of coating thickness. Data appear clearer if ice adhesion is expressed in terms of thickness ranges than a continuous distribution.

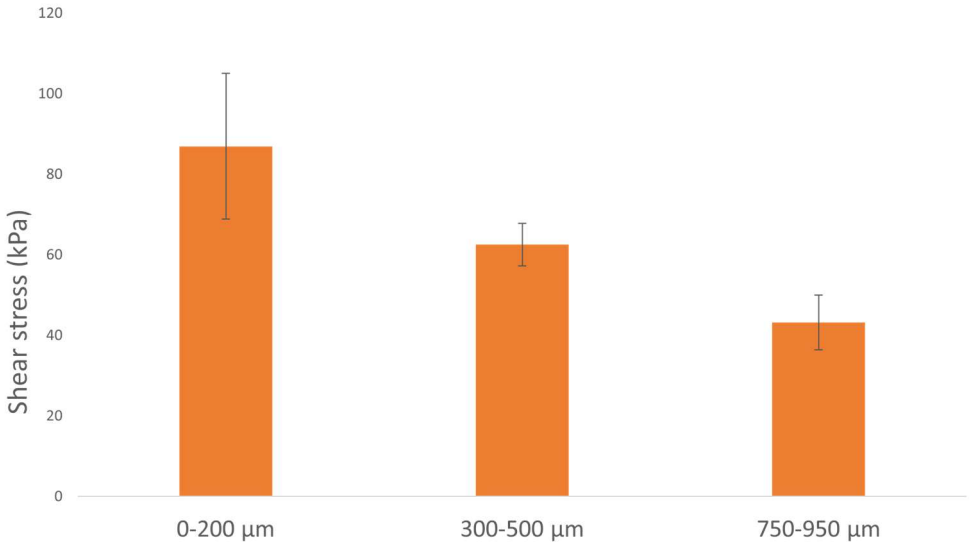

Figure 4.19 – Syl 186 film thickness ranges vs. ice detachment

4.2.1.4.1 Effects on ice detachment behaviour

Differences in ice detachment behaviour have been noticed between harder and softer coatings.

For hard coatings, being them elastomeric or not, ice detachment proceeds with a fast and linear increase in force vs. displacement. In this cases, ice is detached abruptly when a certain force is reached.

Softer elastomeric coatings, as Syl 20:1, instead exhibit a peculiar mechanism. This behaviour have been investigated combining slow motion pictures with data from the test. Load cell data are collected every 100ms, which is a frequency high enough to see a trend but still giving very coarse data. For a further characterization, higher frequencies of sampling must be used.

This mechanism have been divided in three phases:

A) elastic deformation of the coating (images 1 and 2)

B) elastic relaxation with insertion of bubbles between ice and coating (image 3, red circle)

C) detachment/peel off (image 4)

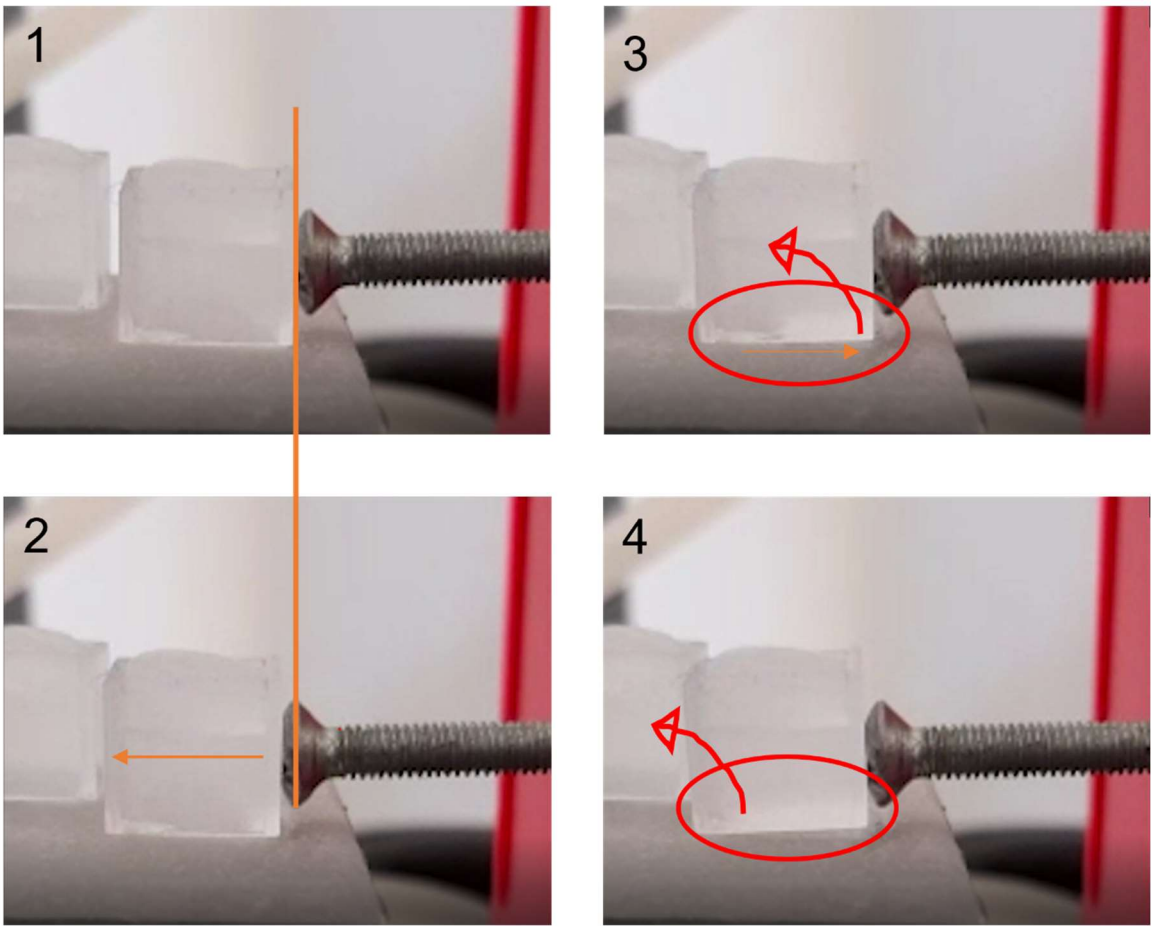

Figure 4.20 – Four frames from a slow motion video of ice detachement

Due to the high deformability of the coating itself, when the probe touches ice an elastic response from the coating is triggered, resulting in a more steep increase in force vs. displacement.

After this, air starts to wedge between ice and coating. This is linked to elastic relaxation of the coating itself.

Ultimately, force vs displacement steepness rises up again and decreases almost linearly until ice completely detaches from the substrate, in other words: ice is gradually peeled off the substrate.

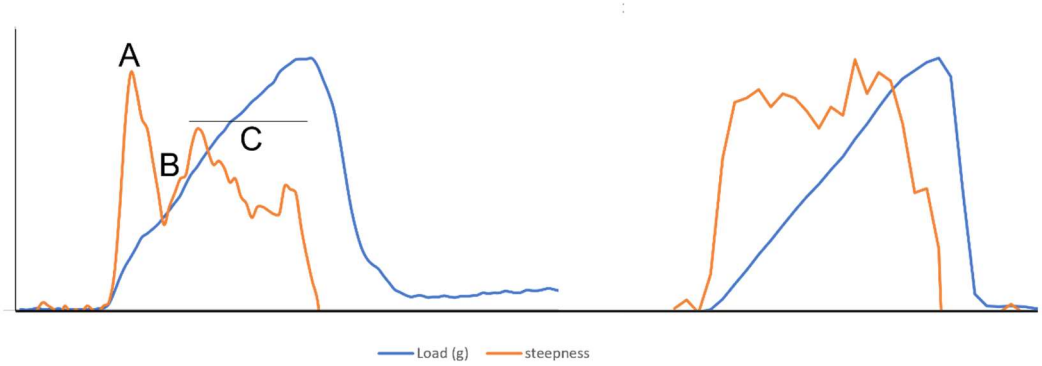

Figure 4.21 – Force vs displacement plots for 20:1 Syl 186 (left) and 5:1 Syl 186 (right). Detachment phases A, B and C are highlighted on the 20:1 sample.

4.2.2 Mixed matrix PDMS (M-PDMS)

Mixed matrix elastomers have been prepared with the aim of modifying PDMS' elastic properties with the addition of liquids. Polymers of different viscosities have been used to investigate the effect of the introduction of non-uniformities in terms of Young moduli in samples. These polymers have been also chosen to ensure a lower ice adhesion strength by exploiting their capability to create a quasi-liquid layer upon the surface.

In this light, PEG-400, Pluronic P-123 and PDMS silicon oil (MW 95'000, high viscosity) have been added to Sylgard PDMS 184 or 186 to test the anti-icing properties of these mixtures. Sylgard PDMS A and B components have been used in 10:1 ratios throughout all experiments. The effect of the addition of PMHS as a hardener will also be investigated.

4.2.2.1 Nomenclature

Samples will be noted with four numbers indicating mass ratios in this order: PDMS_PEG-400_Silicone oil_PMHS (MW 95'000), followed by 184 or 186 indicating which Sylgard PDMS is used in the formulation, e.g. a 10_1_1_1 186 sample contains 10 parts in mass of Sylgard PDMS 186, 1 part PEG-400, 1 part Silicone Oil, 1 part PMHS.

Samples are prepared by mixing the components in the defined ratios, spin- or brush-coated on aluminum plates and cured at 150°C/2h.

4.2.2.2 Peg influence on ice adhesion and CA

The first tests were performed to evaluate how the presence of PEG-400 in a Sylgard PDMS matrix could influence anti-icing properties.

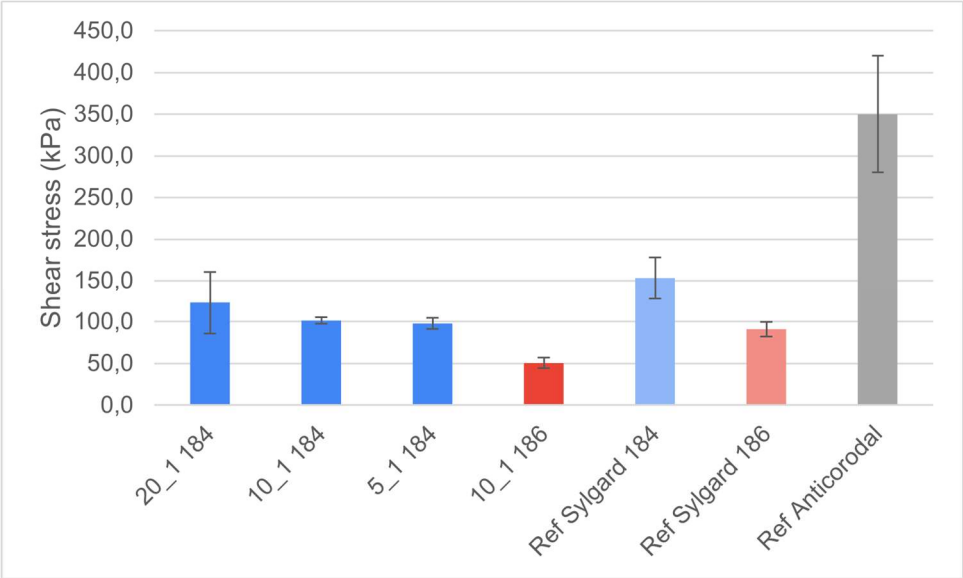

Figure 4.22 –Influence of increasing PEG concentrations

As can be seen, addition of PEG-400 decreases ice adhesion strength of both Syl 184 and Syl 186. It is important to note that the ratio between samples 10_1 186 and 10_1 184 ice adhesion strengths is very similar to that of the Ref 186 and Ref 184, indicating an incremental effect on anti-icing properties when combining the effect of PEG to the effect of a more anti-icing elastomer matrix, as Syl 186 is. CA are also affected by PEG-400 presence, increasing from 105° to 118° from 20_1 184 to 5_1 184 samples. Samples containing only PEG-400 resulted too fragile (0B in the hardness test, completely peeled off or broken).

4.2.2.3 Addition of PHMS and silicon oil

To solve this problem, following samples have been prepared adding PMHS. PMHS is used to obtain a more cross-linked silicone matrix by offering more hydride moieties to bind to the vinyl part of Syl PDMS.

A 10:1 mass ratio Syl PDMS to PMHS results in a harder, more cross-linked, PDMS matrix.

A very viscous silicon oil has also been added to samples.

Anti-icing have been performed on samples containing either or both silicone oil or PMHS, revealing an increased ARF in respect to mixtures containing PEG-400 only. This effect is somehow in contrast in respect to theory, a harder elastomer should have a higher shear stress of ice adhesion. PMHS and silicone oil addition are uninfluential at least in terms of contact angle and SFE, whereas a noticeable difference in terms of ice adhesion is evident in presence of the latter. Samples 10/2/1/2 184 and 5/1/1/1 184 show a 3 fold reduction of ice adhesion.

The same 10/2/1/2 and 5/1/1/1 samples have been prepared using Syl 186 as a matrix.

Samples prepared starting from Syl 186 report a similar ice in adhesion reduction even starting from a lower ice adhesion for the Syl 186 in respect to Syl 184.

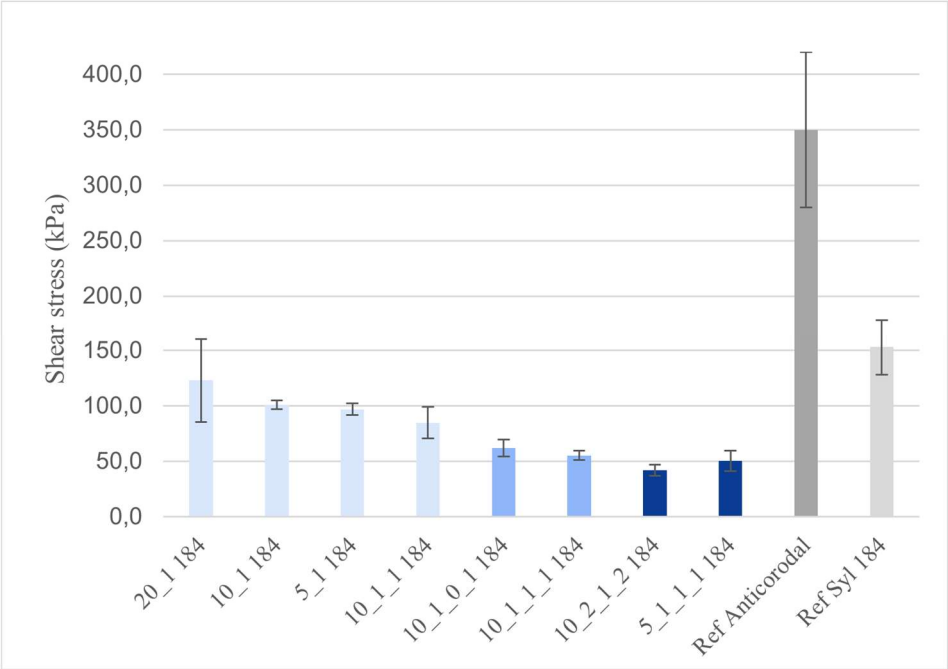

Figure 4.23 –Ice adhesion for M- PDMS. Darker blue tonalities indicate higher PMHS/Syl 184 ratios.

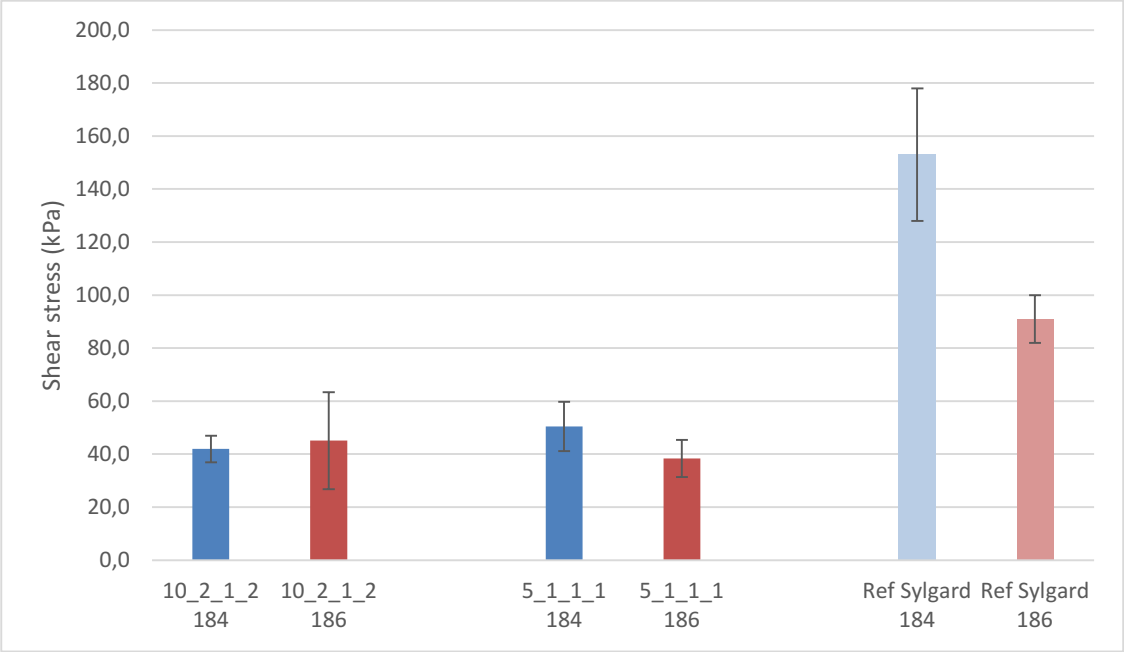

Figure 4.24 –Ice adhesion for PMDS-M with Syl 184 and Syl 186

Table 4.7- SFE for PDMS-M

Sample	Syl 184	Syl 186	5/1 184	10/1/1 184	10/1/0/1 184	10/2/1/2 184	10/2/1/2 186
Total SFE (mN/m)	26,1 (0,3)	25,4 (2,9)	27,5 (0,3)	25,7 (2,9)	26,7 (1,3)	25,6 (1,3)	26,2 (1,2)

4.2.2.4 Hardness characterization

Resistance to mechanical wear is also very important. Samples have been characterized with tape test measurements using a 10 blade cutter. Only samples containing PMHS show a resistance to scratch comparable (3B in tape testing) to those of bare Sylgard PDMS.

4.2.2.5 In-lab PDMS mixed matrix

A 10_1, 10_2_1_2 and a 5_1_1_1 mixture have also been tested with an in-lab-prepared PDMS analogue. In this case, PMHS and vinyl terminated PDMS have been mixed in 1:30 ratio in presence of acetonitrile as an inhibitor, additioned with silicone oil and PEG-400, brush or spin coated and then cured at 120°C/2h.

This set of samples with an in-lab prepared matrix have been indicated with a C instead of 184 or 186 in their names.

It is important to notice that a 30:1 mixture of PDMS-vyn/PMHS reported a lower shear stress of ice adhesion when compared Sylgard 184 or 186.

10_2_1_2 C samples showed a reduction of ice adhesion in respect to a bare C coating.

Given the ARF similarities between samples containing PEG and silicone in respect to their bare PDMS counterparts, them being 184, 186 or "C" coatings, it can be said that addition of polymers of different viscosities to an elastomeric matrix is useful in terms of reducing ice adhesion.

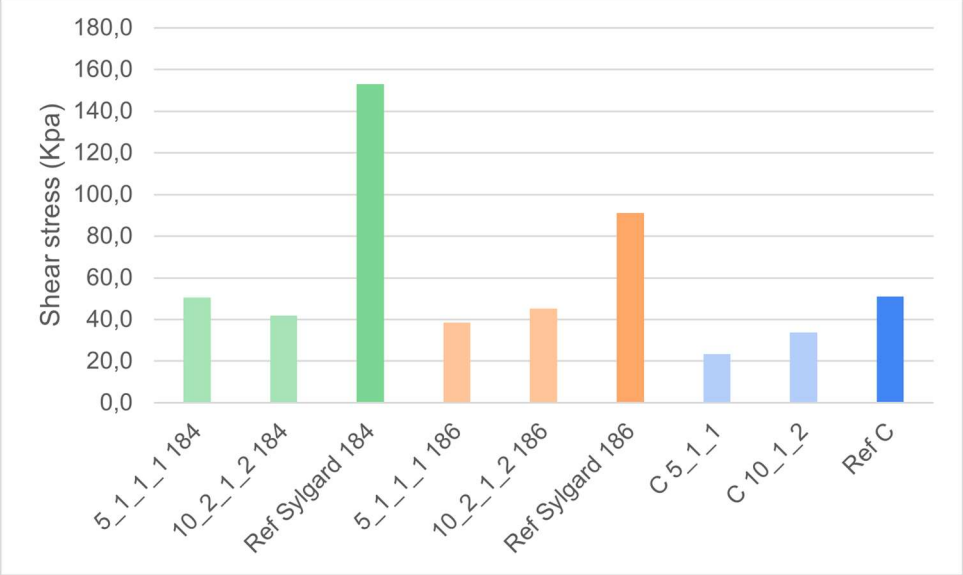

Figure 4.25 –ice adhesion of Mixed Matrix PDMS samples (Syl 184 vs Syl 186 vs PDMS-vyn/PMHS 30:1)

4.2.2.6 Hardness characterization

AFM testing have been performed on these samples in order to understand if different viscosities of the fillers could results in microscale inhomogeneities in terms of young moduli of the samples themselves. Samples have higher YM than pure PDMS ($\sim 2MPa$).

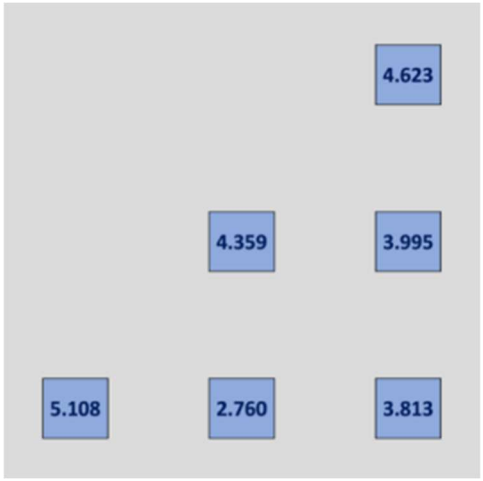

Figure 4.26 –Young moduli (MPa) for 10_2_1_2 184 sample (grey square side is 500µm)

Given the inhomogeneity of YM for this sample, it is to suppose that differences in elasticity of the surface may aid ice detachment by creating preferential paths for bubbles to wedge in.

4.2.2.7 Outdoor testing

A 75cm aluminum conductor have been coated with 10_2_1_2 184 and have been tested during winter 2021-2022 in the WILD facility of Vinadio, Italy. The same conductor have been recoated with a 10_2_1_2 186 coating and has been exposed for 2022-2023 winter.

4.2.2.8 Snow laboratory testing

The 75cm long 10_2_1_2 186 sample have been tested in the snow laboratory before exposure. A complete detachment of the snow sleeve has been observed. Results will be discussed more deeply in the snow laboratory section.

4.2.3 PDMS-B

This set of samples have been prepared in order to obtain a porous and "bubbly" PDMS (PDMS-B) surface in which a liquid, as silicone oil, organic oil or others could be stored in.

Several synthesis' have been tested, including mixing PDMS-vyn and PMHS (the reaction develops hydrogen and gas could create channels in the elastomer matrix) ,mixing PDMS with some solvents as EtOH and iPrOH and then heating to create a porous surface. None of these preliminary tests have developed a surface which could incorporate oil in a satisfactory way.

4.2.3.1 PDMS + hydrogen peroxide

Test have been then conducted on a mixture of hydrogen peroxide and Sylgard PDMS 186. Components have been thoroughly mixed, brush-coated on AC plates and cured at 120°C for 2h.

A surface with bubbles which could incorporate liquids is obtained. Most of the porosity is connected. Pressing with a finger on a bubble inflates others, not only adjacent ones.

Different ratios of Sylgard PDMS 186/H_2O_2 have been tested, ranging from 5/1 to 20/1. As can be seen, no visual differences between samples is apparent. 20/1 ratios have been used throughout all experiments.

Figure 4.27 – Image of 1:20, 2:7 and 1:6 PDMS-B samples

Tape tests have been conducted on these samples, showing a remarkable resistance to scratch considering how thin the top layer of PDMS is, resulting in a 3B hardness, comparable or higher than Sylgard PDMS 186. An interesting thing to note is that, after scratching the surface, even when the top side of the bubble is torn away, the PDMS layer on the surface remains .

To assess the volume of liquids that can be incorporated in their porosity, samples have been weighed, immersed in EtOH for 5 minutes, dried on the back side (which is untreated) and weighed again. The so-measured weight difference was 0.77g on a 50x50mm sample, indicating a volume incorporation of 40 ul/cm2. The same measure have been conducted on a non-porous Sylgard PDMS 186 sample as a control; in this case, volume incorporation was less than 0.5 ul/cm2 , around two orders of magnitude lower than its porous counterpart.

Anti-icing performances have been measured , reporting a remarkably low adhesion with an ARF of 25.

Due to the surface stretching, the ice detachment graph is peculiar., This low force-long stress time type of graph is typical of very elastic materials. A side-to-side comparison with a Syl PDMS 186 sample highlights how ice detachment is very different for PDMS-B. From one side, the force ramp up is more gradual when pushing the ice away from the surface, due to an easier and abundant deformation of the surface; from the other, once maximum force is reached, ice is slowly torn off the surface instead of being abruptly detached.

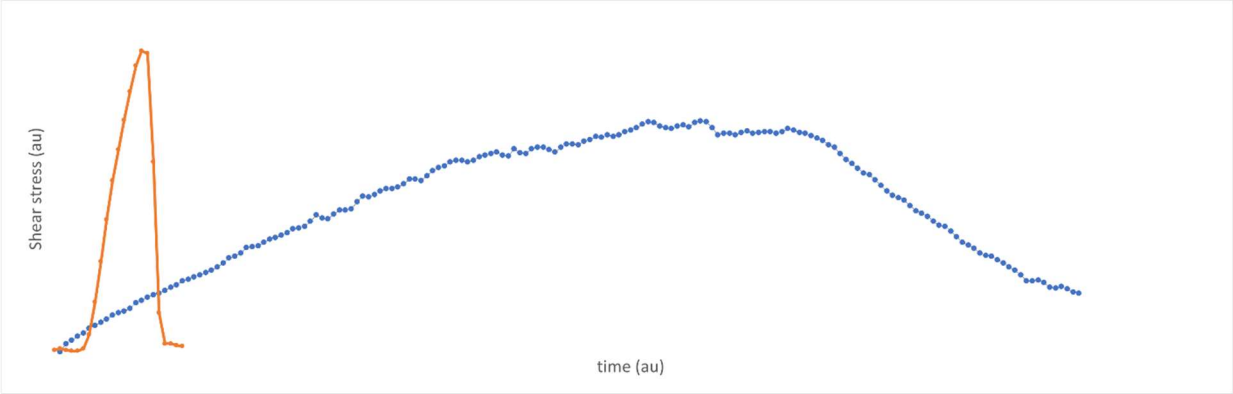

Figure 4.28 – Shear stress vs time plot of a Syl186 sample (orange line) and PDMS-B (blue line).

Samples need outdoor testing to assess how anti-icing in real conditions is affected by this peculiar detachment behaviour. Though, laboratory results, considering the low maximum force of detachment, mimicking real conditions which could be attributed to wind force, weight or oscillations, are promising.

4.2.3.2 Liquid infused PDMS-B

PDMS-B samples have been synthesized to store anti-icing liquids in their cavities. To this scope, peanut oil and a spray silicone lubricant have been added to this formulation.

Silicone lubricant have been sprayed on samples' surface for 5 seconds (50x50mm plates) from a distance of 20-30cm. These samples will be called PDMS-BL.

4.2.3.3 Durability testing

Samples have been exposed for 100 days starting from 6/6/2022 .

PDMS-BL has retained a lower ice adhesion even after 180 days. PDMS-B show low ice adhesion and good durability and good properties of infused liquid retention.

A PDMS-BL sample have been exposed in WILD station in 2022-2023 winter.

4.2.4 Durability tests

Durability in a real environment for elastomeric coatings have been tested. Samples have been exposed for 100 days starting from 6/6/2022 in Piacenza, Italy, facing south.

The exposed samples have been tested for ice adhesion after being taken back in the lab.

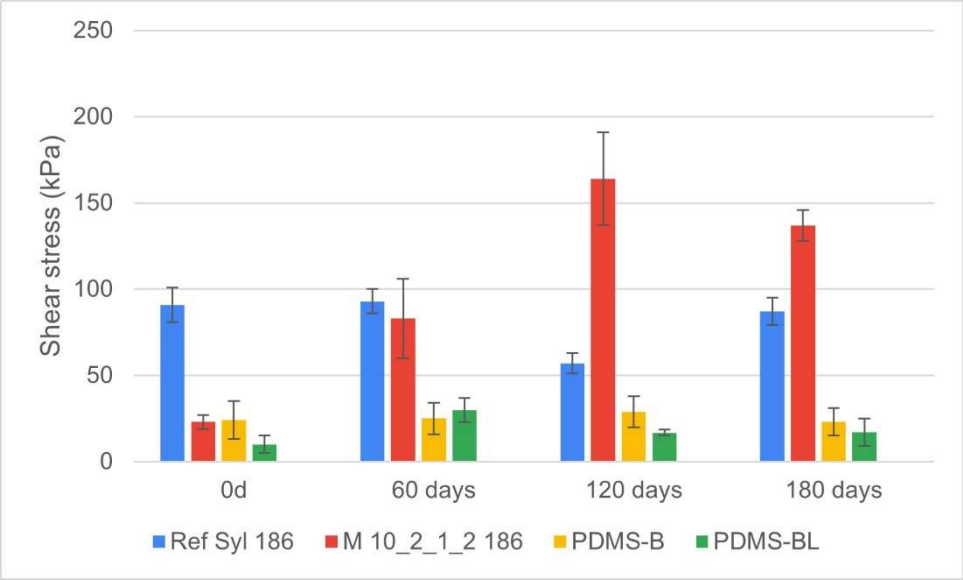

Figure 4.29 – ice adhesion of PDMS based samples after 180 days

Syl 186 reported no degradation in 180 days. 120 days data can be looked at as outliers.
M 10_2_1_2 186 samples showed a heavy increase in ice adhesion, this is probably due to the presence of pores which, once emptied of PEG-400 and silicone oil offer anchoring spots to ice.

PDMS-B and PDMS-BL show no signs of degradation in 180 days, with PDMS-BL samples reporting lower ice adhesion, hinting at a permanence of lubricating material even after 6 months.

4.2.5 Large scale samples

Samples Syl 184, Syl 186, PDMS-C 30:1, PDMS-BL, M 10_2_1_2 184 and M 10_2_1_2 186 have been exposed in WILD station in winter 2020-2021, 2021-2022 and 2022-2023.

All samples in the first two years have been tested on 75cm samples. 15m samples of Syl 184 and Syl 186 were exposed for 2022-2023.

Full characterization until 2022 will be discussed specifically in chapter 4.6.

4.2.6 Considerations

Anti-icing research on elastomers gave very insightful results. Several lines of research have been followed by colleagues as well.

Being the newest field of research for the laboratory, some questions are still open and some samples still need to be optimized.

Anyway, obtained ARF factors are comparable to literature. A characterization of samples in terms of anti-snow properties is necessary and already on its way.

Characterization on viscosity, liquid and solid fillers, times of reaction, thermal treatment and relationship between anti-icing and chemico-physical properties all come into play thinking of a large scale application.

Also, most of the challenges in preparation of large samples are being overcome. One time to the next, winter sample preparation (>100 times larger than laboratory ones) is becoming easier due to experience and previously produced and acquired tools. Large scale samples preparation also gives direct insight on applicability of produced coatings, being or not elastomer based.

Additionally, a even more important insight is to directly participate “hands-on” in samples exposure in WILD station and seeing how a task like the removal of a 400m span of wire is made by trained TERNA operators.

4.3 Sol-Gel reactions

Sol-gel hydrophobic coatings have been synthesized following two ways:

-acid catalysed TEOS + PDMS-OH

-base catalysed with embedded Pluronic

PDMS-OH is a liquid formulation with a linear chain sold with different viscosities. Relationship between viscosity and chain length is reported and found online.

4.3.1 Acid-catalysed PDMS- OH + TEOS

4.3.1.1 Effect of PDMS-OH concentration and chain length: hydrophobicity, anti-fouling, anti-icing

PDMS-OH/TEOS (P/T) coatings have been synthesized with the aim of investigating the effect of the PDMS/TEOS ratio and PDMS-OH chain length on hydrophobic properties.

Three PDMS-OH viscosities have been used: 65cSt, 750cSt and 2750cSt.

Reagents have been mixed with 4/9 or 1/1 ratios (PDMS-OH/TEOS) in EtOH (TEOS/EtOH ratio 1:1), heated at 60 °C under stirring for 2h, until an increase of viscosity appears evident. Glass and aluminum samples have been dip-coated in the solution and heat treated at 120°C/2h.

Samples reported very low tilting angles even at low temperature. Remarkably, icing didn't occur until -15°C for all samples. CAs are in the 95°-105° range for all the samples.

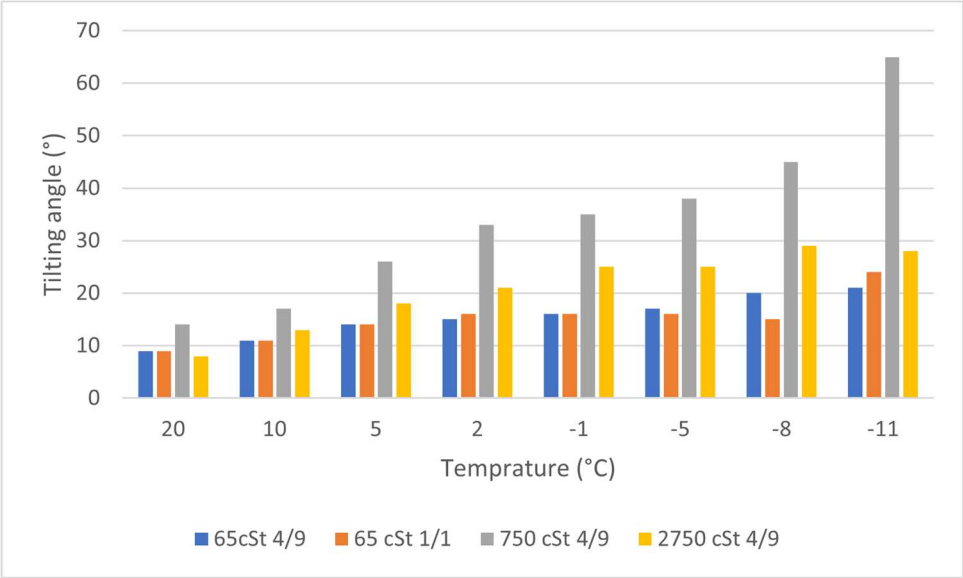

Figure 4.30 – Tilting angles in function of temperature for P/T aluminum samples.

P/T glass samples showed remarkably high FRF in preliminary test with both the reported methods.

Table 4.8- FRF for glass P/T samples (first three results are obtained with the "fast" testing method; ESDD and NSDD are obtained with RSE method

	Kaolin	Carbon Black	NaCl	ESDD	NSDD	Total FRF
65 cSt 4/9	25	1,8	6	-	-	-
65 cSt 1/1	16,5	2	12,5	38	16	54
750 cSt 4/9	10	1,5	10	26	2	28
2750 cSt 4/9	12,5	1,6	5	-	-	-

Anti-icing properties have also been tested. Samples showed an ARF of 20 for 65cSt 4/9 samples, the others showed lower results (ARF 7-10). All samples came with very high standard deviations (>50%).

P/T 65cSt 4/9 have also been tested in the iCORE wind tunnel, giving the lowest ice adhesion by far.

Anti-icing properties are not retained for a long time, though.

4.3.1.2 Durability issues

Durability issues showed up from the second test with ice detachment machine: shear stress increased more than 3 times if the same spot on the sample was tested.

Samples have been exposed (days counting from June 3rd 2022) and reported an heavy increase of ice adhesion after 120 days. It is to hypothesize that data are very dependent from meteorological conditions: heavy rain didn't fall until 50 days from exposure, resulting in an abrupt deterioration of the coating properties between 40 and 60 days testing.

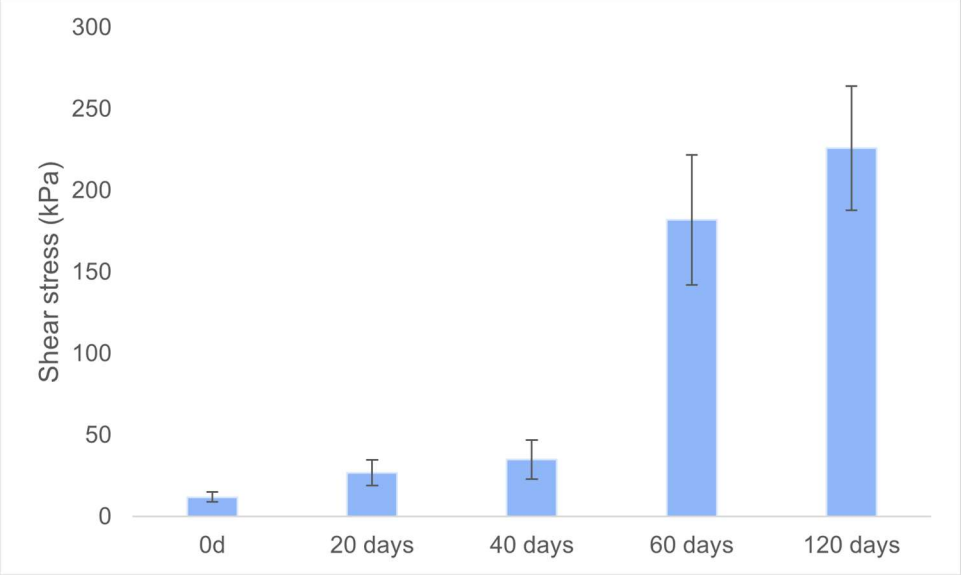

Figure 4.31 – Increase in ice adhesion for P/T 65cSt 4/9 sample.

Samples have also undergone accelerated weathering. In that case only CA after weathering have been tested and no appreciable deterioration in hydrophobic properties was seen.

It is to consider that P/T formulations are viscous and present many -OH moieties, allowing many bonding spots but also prone to hydrolysis. An hypothesis in that the formulation adheres firmly to the substrate only with a very thin layer, resulting in no differences in CA after rain. Above this this layer, an oily thicker layer, which is weakly bonded and exposed to hydrolysis, is present but is washed away very soon after mechanical stress or exposure to rain.

4.3.1.3 Tests to increase durability

A huge amount of samples have been formulated and synthesized to obtain more durable P/T coatings.

A total of more than 60 samples have been synthesized. The table below shows some of the investigated variables.

Table 4.9- Variations to P/T samples

Treatment conditions	Solvent amount	Catalyst	Crosslinking reagent	Other conditions
60°C	10 times EtOH	Acid pH 3 (HCl or H_3PO_4)	TEOS	Ratios up to 5/1 PDMS-OH/TEOS
Direct heating 120°C	No solvent	Acid pH 1 (pure HCl added)	M-TEOS	Times of reaction from 2 minutes to 8h
Ultrasounds 50°C	Solvent evaporation	NaF	Boric acid	Two step addition of PDMS-OH
80°C	Dilution	Ammonia		Closed reaction

The above table is to be intended as matrix in which most of the possible samples have been tested.

All in all, the reactions ended up in just two different categories: oily and solid samples.

Tests that resulted in oily coatings reported the same durability issues as previously reported (NaF catalyzed reactions showed slightly more durable coatings but results weren't encouraging enough to be investigated further).

In other cases, the reaction led to a solid film coating with 50-60 kPa of ice adhesion shear stress and a FRF not comparable to the ones presented before. Those results were not investigated further due to the

difficulty in obtaining a well-structured layer on samples' surface. Some tests with boric acid as a crosslinker phase transitioned from a viscous liquid to a solid in a matter of seconds. So obtained coating resulted fragile and waxy in most cases, unless a very slow solvent evaporation was allowed. All the reactions seem to maintain their viscosity (very slow reaction rate) when placed at 3°C.

4.3.1.4 Considerations

Although alluring, P/T samples have shown big issues in terms of durability. Given the amount of testing, a fine-tuned reaction that could synthesize a material which is durable but maintaining P/T remarkable anti-icing and anti-fouling properties is hard to imagine. Research has proceeded towards finding conditions for which a solid layer coating which could still result oily to the touch (also to ice and dirt) could be obtained.

4.3.2 Mixed matrix TEOS (MM TEOS)

Mixed matrix samples have been prepared with a base catalysed sol-gel reaction.

Methyl triethoxy silane, hydroxy terminated PDMS and Pluronic P-123 have been exploited to create a coating that could have PDMS induced hydrophobicity and the low-temperature properties (quasi-liquid layer) of Pluronic.

The optimized reaction contains: M-TEOS : PDMS-OH 65cSt : PDMS-OH 750cSt : Pluronic (P123, 5k6Da) : water (1% NaOH) (mass ratios 4:2:1:0,5:5). The hypothesis behind the use of two different PDMS chain lengths and base catalysis was to create a web-like network containing Pluronic molecules.

Reactants have been kept under stirring for four hours. Samples have been dip-coated or brush-coated and heat treated at 120°C/2h.

4.3.2.1 Hydrophobicity, anti-icing properties, anti-fouling properties

MM TEOS samples reported low tilting angle at low temperature, unremarkable anti-icing properties (100kPa shear stress) and just decent FRF (values around 2 for all contaminants). Samples tested for icing temperature reported -12°C freezing temperature. Such a result can be an hint about the anti-icing effect of Pluronic as an anti-icing material.

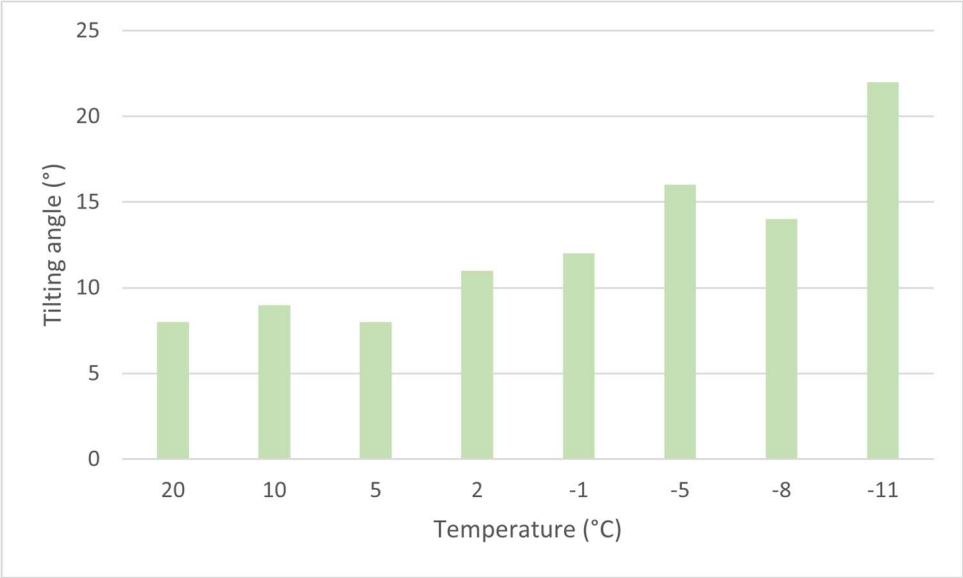

Figure 4.32 – Tilting angle at low temperature for MM TEOS samples

Aging tests have been conducted: MM TEOS samples have been immersed in acid, basic and saline solutions and tested for CA.

Table 4.10- Water Contact angle of MM TEOS samples after wet chemicals aging

	New sample	24h CA (°)	48h CA (°)	1week CA(°)
Acid (pH=3)	89 (5)	87(6)	83(9)	95(17)
Base (pH=9)	92(5)	x	88(4)	79(5)
Saline (35 g /l NaCl)	88(10)	78(11)	85(3)	83(9)

Table 4.11- Tilting angles of MM TEOS samples after wet chemicals aging

	New sample	24h Tilt (°)	48h Tilt (°)	1week Tilt(°)
Acid (pH=3)	6,6 (0,5)	11,4 (2,7)	12 (3,8)	64 (11)
Base (pH=9)	3,6 (2,1)	x	33 (5)	60 (7)
Saline (35 g /l NaCl)	4 (1,3)	x	24 (5)	48 (11)

MM TEOS showed a good resistance to chemical aging. No deterioration is seen in CA, whereas Tilt angles are increasing but some water dynamic properties are seen even after 1 week of immersion.

4.3.2.2 WILD station results

MM TEOS samples have been selected for outdoor exposure during 2020-2021 winter due to the lack of samples and the possibility to use the coating on Al surfaces. A 75cm sample have been exposed and reported unexpectedly good results. MM TEOS samples will need a more profound investigation.

4.4 Photocatalytic materials

4.4.1 TiO_2

TiO2 photocatalytic properties have been exploited to degrade organic compound accumulating on insulators' surface.

Throughout all experiments, nanometric TiO2 particles (TiO2 NP) synthesized by laser ablation by colleagues at RSE [96], have been used.

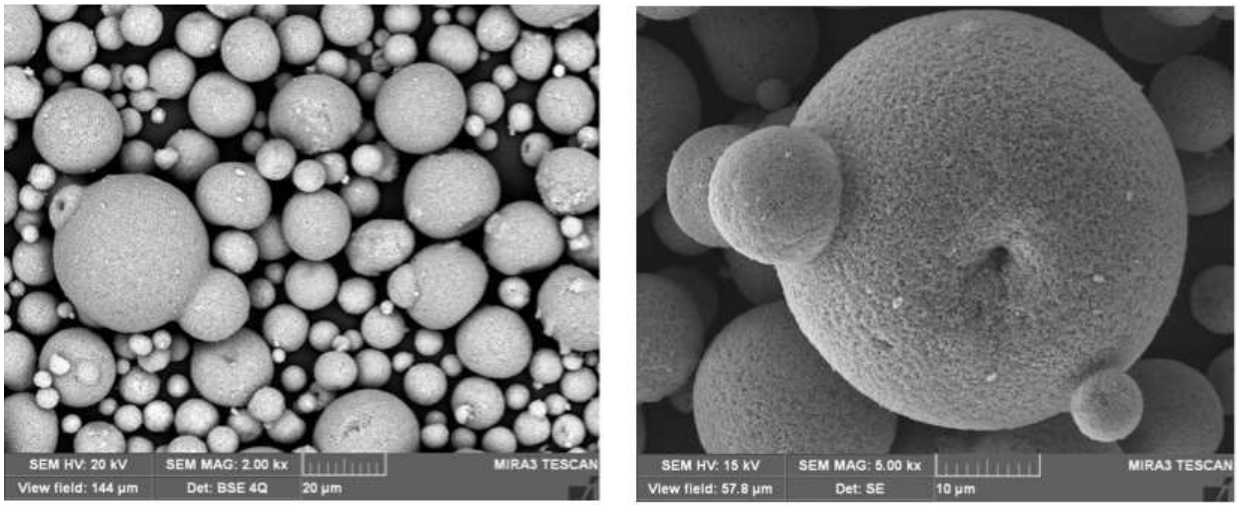

Figure 4.33 – SEM images at 2kx and 5kx of TiO_2 particles. Spheres in the pictures are composed of agglomerates of particles <200nm.

4.4.1.1 Glass adhesion

Before testing their photocatalytic properties, glass adhesion of TiO_2 NP was investigated. NaOH activated and DW cleaned microscope slides have been immersed for 2h in water containing different concentrations of TiO2 NP and then thermally treated at 200°C or 350°C. Solutions have been acidified to pH=3 with addition of HCl. The table below shows conditions which have been investigated.

Table 4.12- Samples, TiO2 concentration and calcination temperature.

Sample	TiO2 conc. (g/l)	Calcination T (°C)
TiO_2_25h	25	350
TiO_2_25l		200
TiO_2_10h	10	350
TiO_2_10l		200
TiO_2_2h	2	350
TiO_2_2l		200

4.4.1.2 Ti concentration on the surface

After thermal treatment, an opaque film is obtained on glass slides. Ti concentration on their surface have been investigated with XRF, confirming the presence of a growing concentration of Ti at the increase of TiO2 concentration in solution.

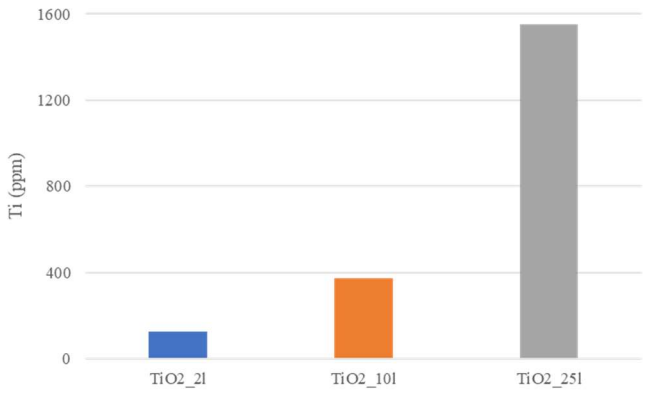

Figure 4.34 – Ti concentration on glass surface.

4.4.1.3 Adhesion testing

Samples' contact angle have been measured on samples exposed to light, since CA could vary when TiO2 is not exposed to light. Tape tests have been performed on TiO2 coated samples to assess their adhesion to the glass substrate. Standard 3M scotch tape have been made stick and pulled away from the surface for 10 times and then CA was recorded after cleaning the samples with acetone to remove any leftover glue.

Table 4.13- Contact angles before and after tape testing.

Sample	CA (°)	CA after tape test (°)
Bare glass	46,7 (4,0)	
TiO_2_25h	6,1 (2,3)	8,3 (2,4)
TiO_2_25l	7,7 (2,6)	9,3 (2,2)
TiO_2_10h	6,4 (2,9)	7,2 (2,5)
TiO_2_10l	23,0 (4,7)	20,1 (1,6)

TiO_2_2h	8,1 (3,8)	50,1 (1,3)
TiO_2_2l	48,0 (9,2)	35,8 (6,3)

As can be noticed, samples treated at high temperature report lower CA, especially in low concentration samples indicating a dependency particle adhesion in function of T. A good level of adhesion is shown by tape test data, except for low concentration samples. This is indicated by a low variation between the before and after CA.

Sample TiO2_25l is the most promising sample under many points of view: high particle concentration on its surface, high particle adhesion, lower treatment temperature and super-hydrophilicity.

4.4.1.4 TEOS TiO_2 and Glued TiO_2

Another set of samples were made with a two-step procedure: glass slides were first immersed in a acid TEOS sol-gel solution (5ml TEOS, 50ml EtOH, 1,5ml water, 0,5ml HCl 37%), then immersed for 30'in the TiO2 25 g/l solution and heat treated at 80°C for 1h. Lower heat treatment temperatures are particularly appealing for insulators, due to their composite structure (usually glass and cement) which can suffer of cracks if treated at high temperatures.

Further approaches regarded the incorporation of TiO2 NP in a glue matrix, to this scope a commercial methyl-cyan acrylate glue (Ciano TiO2) and a silicone based sealant TESA glue (MS TiO2) have been used. For both samples, glue have been deposited on the surface and the glass slide pushed flat on an amount of TiO2 powders.

4.4.1.5 Contact angle, tilt angle, adhesion, Ti concentration

CA, CA after tape test, Tilting Angle and XRF analysis are reported for all the samples in the table below.

Table 4.14- Contact angles before and after tape testing, tilting angles and Ti concentration for all TiO_2 samples.

Sample	CA(°)	CA(°) after tape test	Tilt angle (°)	Ti XRF conc. (ppm)

TiO2_2l	48,0 (9,2)	35,8 (6,3)	55,7 (5,0)	131
TiO2_10l	23,0 (4,7)	20,1 (1,6)	44,4 (5,5)	390
TiO2_25l	7,7 (2,6)	9,3 (2,2)	30,1 (5,5)	1554
TEOS- TiO2	37,9 (4,2)	38,2(2,3)	>90°	3075
MS TiO2	88,7 (8,2)	60,3 (6,4)	57,2 (5,7)	-
Ciano TiO2	142,8 (4,3)	147,6 (4,2)	147,1 (2,1)	-

CA and Tilt measurements highlight the Superhydrophilicity (very low CA with moving droplet) of TiO2_25l samples, which is regarded as a good anti fouling mechanism. TiO2_25l reporting a FRF (fouling reduction factor) of around 1,5is due to the fact that water sliding away from the samples' surface sweeps a wider area due to the low contact angle. Ciano TiO2 samples show almost SHP values of CA and tilting angle, with the typical Roll-Off mechanism when surface is tilted. A good degree of proportionality between solution concentration and Ti ppm on the surface is visible from TiO2_2l, TiO2_10l, TiO2_25l data, whereas TEOS TiO2 show an even higher Ti concentration on the surface hinting at the presence of a thicker layer of TiO2 on the surface, incorporated in the TEOS structure adhered to the glass surface.

4.4.1.6 Fouling reduction factors

Fouling reduction factors have been evaluated for all the samples: the ideal sample has a combined effect of conventional (atmospheric water induced) self-cleaning and photocatalytic properties.

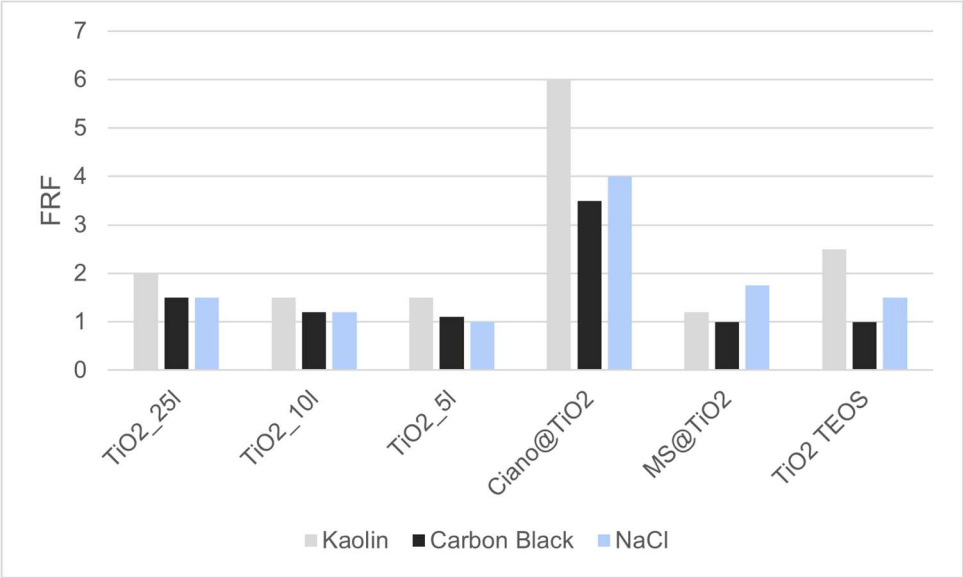

Figure 4.35 – FRF for TiO_2 samples

The graph show how some effect on FRF emerges from TiO_2 samples, especially for SHP Ciano@TiO_2.

Interestingly, TiO_2_25l and TiO_2 TEOS show a FRF of 2 or higher for kaolin, due to superhydrophilic properties.

4.4.1.7 Accelerated weathering tests

Accelerated weathering tests have been performed on photocatalytic samples .

Contact angle and visual testing have been used to assess the deterioration of coating properties.

Coatings MS@TiO_2 and Ciano@TiO_2 have been discarded following the complete detachment of the coating.

The remaining samples maintained their opaque appearance that was present after immersion in TiO_2 solution and thermal treatment.

TEOS@TiO_2 samples have proven to be the most resistant to weathering, with a slight decrease from 34° to 19° in CA. This effect has been attributed to a higher exposure of TiO_2 particles.

Samples TiO_2_25l and TiO_2_10l have reported a minor increase of CA up to around 33° (glass control CA = 43°) without losing their dynamic properties. Samples have not been tested for photocatalysis.

4.4.1.8 Photocatalytic properties

Photcatalytic efficiency have been tested with the method described in methods chapter.

Percentages of reduction in the intensity of the stearic acid IR peaks after 12h of exposure to UV in respect to t0 are reported hereafter, showing the effectiveness of different coatings in terms of organic molecules degradation.

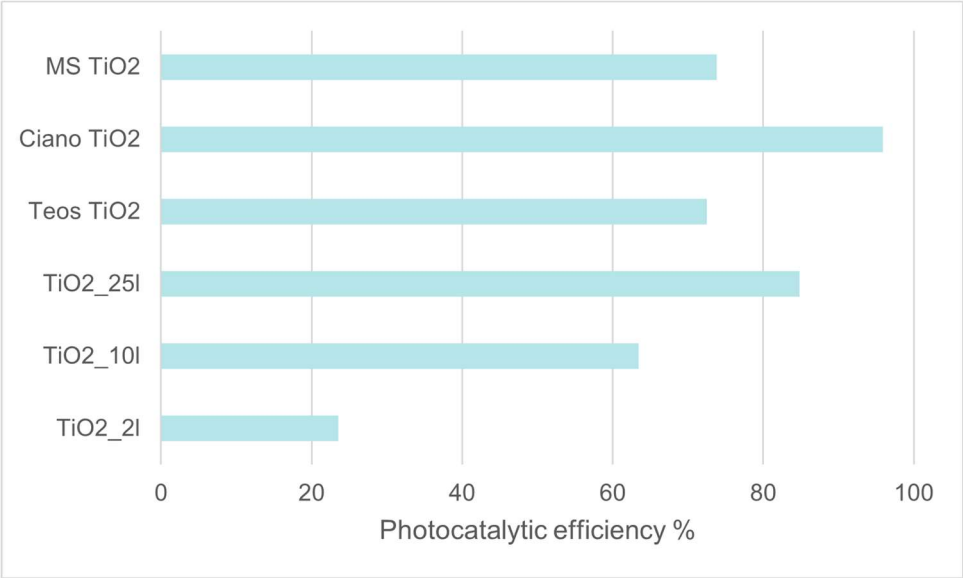

Figure 4.36 – Photocatalytic efficiency after 12h of exposure to UV, based on reduction in intensity of peaks at 2800 cm^{-1} of stearic acid

As can be seen, higher TiO2 concentrations on the surface, as for TiO2_25l, TEOS TiO2, MS and Ciano samples lead to higher degradation rates. TEOS and MS showing less than 80% photocatalytic efficiency can be attributed to the fact that TiO2 particles are not exposed to the surface due to the presence of a surface layer of TEOS or MS probably hindering photocatalytic activity.

4.4.2 Conclusions

Different methods of deposition of TiO_2 NP on glass surfaces mimicking insulators have been tested. Simple immersion in acidified TiO_2 dispersions followed by 200°C thermal treatment report high degree of adhesion an good durability. Adhesion with different glues proved not to withstand weathering. The use of a TEOS acidic sol-gel as a primer reported satisfactory UV degradation results along the possibility to use <100°C thermal treatments.

4.5 Snow rings

Snow ring shapes and dimensions have been developed and tested. All Snow rings in the following image are 3D printed in PLA and the two halves are kept together with a zip-tie.

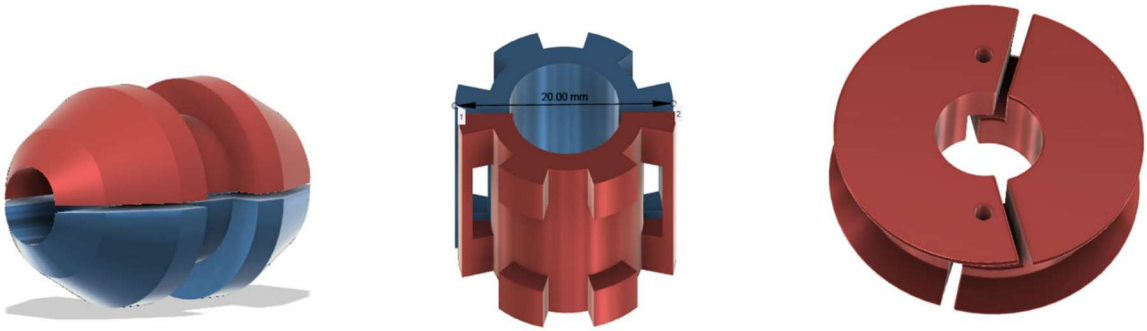

Figure 4.37 – Tested snow ring shapes and dimensions (left: ogive, 30mmx50mm, center: gear, 20mmx25mm or 30mmx30mm, right: yo-yo 100mmx30mm)

The distance from one ring to the next has been kept at 75cm for all samples. Ogive shaped and gear shaped big and small snow rings have been tested on 5m sections of a 15m span in WILD station, winter 2020-2021. “yo-yo” shape have been tested on a 75cm sample during the same winter. Gear shape has been chosen for future characterization, since different shapes reported comparable effects. Smaller diameters seem to facilitate snow sleeve detachment more than bigger diameters. Since images are taken every 15 minutes, such small differences, if present, cannot be appreciated.

SR overall effect can be appreciated, though. In 2020-2021 (ogive +gear small + gear big) and 2021-2022 (only small gear shaped) snow ring equipped samples reported better results than the reference without snow rings.

Snow rings (small gear) have been placed on half of the 400m Al guard wire test span in Cencenighe Agordino.

4.6 Snow and ice wind tunnel characterization

4.6.1 WILD station, Vinadio

Samples exposed in the WILD outdoor laboratory in Vinadio have been tested during 2020-2021 and 2021-2022 winters. The testing station allows up to ten 75cm samples and five 15m samples to be tested at once. Samples are kept in a slow rotation: 12 rph for short samples and 3 rph for 15m ones.

Results of Load and Coverage indexes are presented along with meteorological data.

4.6.1.1 Samples

Some samples are not reported before in this dissertation and will be recapped here:

-boehmite growth conditions on Al: “boil” if they have undergone a 30’ hydrothermal treatment in 100°C water

-acid etching conditions “HCl xM” followed by concentration if they have undergone a 30’ treatment in HCl of concentration x.

-ALK: commercial hydrophobic alkyl-silane coating, Dynasylan 9896, dip-coated and heat treated at 120°/2h.

-“PTFE” samples have a hydrophobic PTFE tape wrapped around the wire. This is a simple but effective anti-snow method used on wires.

-SP samples have undergone shot-peening, which differs from Sand Blasting (SB) in terms of shape of the particles used to obtain the surface treatment. SP used spherical glass particles of homogeneous dimension.

-SB samples have been sandblasted with angular corundum

-C-PDMS refers to PDMS-vyn/PMHS (20:1 + karsted’s catalyst) synthesis as a laboratory made analogue to commercial Syl PDMS

-“reg” samples have been given another coat of coating after being exposed for one year

Winter 2019-2020 campaign

Winter 2019-2020 campaign saw 9 snowing events, 6 meaningful ones, but fewer have been recorded due to some failures. Snowing events are reported in the table below.

Table 4.15- conditions for reported 2019-2020 winter snow events

	event 1 23-24 Jan 2019 13:30-05:30	event 2 31 Jan 2019 18:30-02 Feb 2019 09:45	event 3 02 Feb 2019 09:45-03 Feb 2019 06:30	event 4 1 Dec 2019 04:00-21:00	event 8 5 Mar 2020 13:30-20:30	event 9 25-26 Mar 2020 21:30-07:30
T ave[°C]	-3,6	-2,7	0,2	0,6	0,6	-1,3
T min[°C]	-4,0	-4,6	-0,7	0,2	0,3	-3,7
T max[°C]	-3,1	-1,4	1,4	2,0	1,1	0,9
Relative humidity min[%]	82	74	79	84	82	50
RH max[%]	85	84	84	87	86	85
Water Equivalent Precipitation [mm]	11,8	59,4	12,6	44,0	18,0	9,0
Snow on ground[mm]	190	560	100	190	105	70
Snow density [kg/dm3]	0,06	0,09	0,13	0,23	0,17	0,13
Max sleeve load [kg/m]	0,45	1,28	1,00	3,21	0,85	0,25
Max sleeve thickness [cm]	4,0	5,5	-	5,2	2,5	1,7
Dry/wet	dry	dry	wet	wet	wet	dry/wet

Coverage and load (in brackets) indexes of 75cm and 15m samples are reported in the tables below.

Table 4.16- Samples tested in 2019-2020 winter on 75 cm samples

Sample	Properties	#1	#2	#3	#4	#8	#9	Mean Cov Index	Mean Load index
REF		1	1	1	1	1	1	1	1
SB boil FAS	SHP	0,23 (0.28)	0.35 (0.86)	1.03 (0.31)	-	-	-	0.54(±0.36)	0.48(±0.33)

SP boil FAS	SHP	0.42 (0.39)	0.45 (0.61)	1.05 (0.34)	-	-	-	0.64(±0.43)	0.44(±0.15)
SB boil ALK	Slippery hydrophobic	0.81 (0.63)	0.75 (0.69)	0.90 (0.52)	-	-	-	0.82(±0.08)	0.61(±0.08)
Boil ALK	Slippery hydrophobic	0.79 (0.60)	0.75 (0.77)	0.97 (0.67)	-	-	-	0.84(±0.12)	0.68(±0.09)

Table 4.17- Samples tested in 2019-2020 winter on 15m samples

Sample	Properties	#1	#2	#3	#4	#8	#9	Mean Cov Index	Mean Load index
REF		1	1	1	1	1	1	1	1
SB boil FAS	SHP	1.21 (0.85)	0.54 (1.11)	1.44 (0.,71)	0.35 (1.04)	-	-	0.88(±0.45)	0.92(±0.16)
SB boil ALK	Slippery hydrophobic	1.10 (1.10)	1.02 (0.94)	1.13 (1.21)	0.77 (0.68)	-	-	0.97(±0.15)	0.96(±0.20)

Mainly gathering data about SHP vs slippery samples, 2019-2020 winter testing reported somehow discording results with the few available samples and recorded events. FAS coatings show very different behaviours from one event to the other and even differences between short and long samples. ALK reports worse results but lower variability.

4.6.1.2 Winter 2020-2021 campaign

Winter 2020-2021 campaign saw 13 snowing events. Fewer brought meaningful data.

Table 4.18- conditions for reported 2020-2021 winter snow events

	event 1	event 2	event 3	event 4	event 5	event 6	event 10
T ave[°C]	-1,3	-0,3	-3,7	-0,6	-0,5	0,1	-0,4
Tmin[°C]	-1,7	-0,9	-4,3	-2,1	-1,9	-0,7	-1,2
Tmax[°C]	-0,8	0,7	-3,3	0,7	0,8	0,6	0,3

Ur min[%]	81	76	80	77	77	82	80
Ur max[%]	86	87	83	84	86	87	85
WE [mm]	45,8	12,2	12	26,8	22,8	20	8
hsnow[mm]	420	190	170	270	240	165	110
density [kg/dm3]	0,11	0,06	0,07	0,10	0,10	0,12	0,07
Dry/wet	dw	d	d	dw	dw	dw	d
Max sleeve load [kg/m]	5	1,1	0,9	1,3	1,6	1,35	0,7
Max sleeve thickness [cm]	13,5	8	8	8	10	8	6

Coverage and load (in brackets) indexes of 75cm and 15m samples are reported in the tables below.

Table 4.19- Samples tested in 2020-2021 winter on 75 cm samples

Sample	Properties	#1	#2	#3	#4	#5	#6	#10	Mean Cov Index	Mean Load index
REF		1	1	1	1	1	1	1	1	1
SB boil FAS	SHP	0.86 (0.69)	1.01 (1.03)	1.00 (0.46)	0.90 (0.69)	0.96 (0.75)	0.85 (1.00)	0.99 (0.92)	0.93 (±0.10)	0.84 (±0.18
FAS	Hydrophobic	0.55 (0.38)	0.85 (0.51)	0.46 (0.90)	1.01 (0.45)	0.28 (0.64)	0.85 (1.01)	0.71 (0.49)	0.65 (±0.29)	0.66 (±0.22)
MM TEOS	Slippery hydrophobic	0.47 (0.54)	0.69 (0.56)	0.53 (0.83)	0.85 (0.44)	0.44 (0.64)	1.02 (1.01)	0.73 (0.58)	0.68 (±0.21)	0.64 (±0.21)
HCl 3M boil ALK	Slippery hydrophobic	0.55 (0.51)	-	-	-	-	-	0.79 (0.70)	0.67	0.60

HCl 0.5M boil FAS	SHP	0.44 (0.38)	-	-	-	-	-	0.95 (0.70)	0.70	0.54
Reg ALK PTFE	Slippery hydrophobic + PTFE	0.51 (0.30)	0.69 (0.46)	0.42 (0.74)	0.97 (0.40)	0.28 (0.73)	1.04 (0.97)	0.71 (0.60)	0.64 (±0.25)	0.66 (±0.22)
Reg FAS PTFE	SHP + PTFE	0.84 (0.67)	0.66 (0.46)	0.38 (0.66)	0.82 (0.41)	0.77 (0.69)	0.99 (0.97)	0.85 (0.63)	0.71 (±0.21)	0.69 (±0.18)

Table 4.20- Samples tested in 2020-2021 winter on 15m samples

Sample	Properties	#1	#2	#3	#4	#5	#6	#10	Mean Cov Index	Mean Load index
REF		1	1	1	1	1		1	1	1
SB boil FAS	SHP	0.97 (1.34)	1.04 (1.00)	-	-	-	-	1,03 (0.77)	0.94 (±0.11)	0.76 (±0.46)
SB boil ALK	Slippery hydrophobic	0.99 (1.26)	0.97 (0.67)	0.77 (1.05)	0.94 (1.26)	1.02 (0.88)	0.99 (0.98)	0.96 (1.00)	0.92 (±0.10)	0.83 (±0.37)
SB boil FAS Snow rings (ogive, gear 20mm,	SHP + snow rings	0.59 (0.48)	0.21 (0.43)	0.11 (0.22)	0.69 (1.09)	0.75 (0.68)	0.78 (1.00)	0.49 (0.49)	0.63 (±0.27)	0.61 (±0.36)

gear 30mm										

MM TEOS, FAS and PTFE Reg samples showed good results and wide variability. Event #1 is very meaningful, being a dry/wet snow very abundant event. Snow rings reported a huge effect against snow sleeve accumulation on 15m spans.

4.6.1.3 Winter 2021-2022 campaign

Winter 2021-2022 saw few snowing events. Only 3 are reported.

Table 4.21- conditions for reported 2021-2022 winter snow events

	event 3	event 4	event 5
T ave[°C]	-0.2	0.5	-0.6
Tmin[°C]	-0.9	-0.3	-1.5
Tmax[°C]	0.4	1,7	0.7
Ur min[%]	76	69	83
Ur max[%]	84	86	87
WE [mm]	20	15.6	9.2
hsnow[mm]	320	200	112
density [kg/dm3]	0,06	0,07	0,08
Dry/wet	D	d	d
Max sleeve load [kg/m]	0.82	0.98	0,52
Max sleeve thickness [cm]	5.5	6	4

Table 4.22- Samples tested in 2021-2022 winter on 75 cm samples

Sample	Properties	#3	#4	#5	Mean Cov Index	Mean Load index
REF		1	1	1	1	1

Syl 184	Elastomer	0.67 (0.59)	0.68 (1.03)	0.72 (0.72)	0.69 (±0.03)	0.78 (±0.22)
C-PDMS	Elastomer	0.76 (0.59)	0.68 (1.03)	0.91 (1.04)	0.78 (±0.10)	0.89 (±0.25)
M 10 2 1 2 184	Slippery hydrophobic	0.59 (0.89)	1.01 (1.02)	0.83 (0.56)	0.69 (±0.21)	0.83 (±0.23)

Table 4.23- Samples tested in 2021-2022 winter on 15m samples

Sample	Properties	#3	#4	#5	Mean Cov Index	Mean Load index
REF		1	1	1	1	1
ZnO NR FAS	SHP	0.87 (0.47)	0.56 (0.74)	0.78 (0.51)	0.74 (±0.15)	0.57 (±0.14)
SB boil FAS + Snow rings (20mm gear)	SHP + snow rings	0.87 (0.66)	0.96 (1.05)	0.75 (0.67)	0.86 (±0.10)	0.79 (±0.22)

Winter 2021-2022 data are confused due to the low amount of events. Event #1 is the most abundant one. Elastomer based coatings performed with different accumulation and shedding mechanisms, reporting inverse coverage and load ratios. ZnO NR sample showed remarkable effects on reducing snow load.

4.6.2 Snow laboratory

A few snow laboratory tests have been made on 2022-2023 75cm Al samples, prior to WILD facility testing.

Snow #2 have been used in all experiments. Snow #2 has a high LWC (25%). Chamber temperature is 0°C and air humidity is >77%RH. Samples are kept in rotation at 3 RPM.

Tests are qualitative, being a direct comparison between a bare sample and coated one(s).

4.6.2.1 Test 1: Syl 186

Test #1 assessed Syl 186 anti-snow properties.

No delay in snow accumulation was seen.

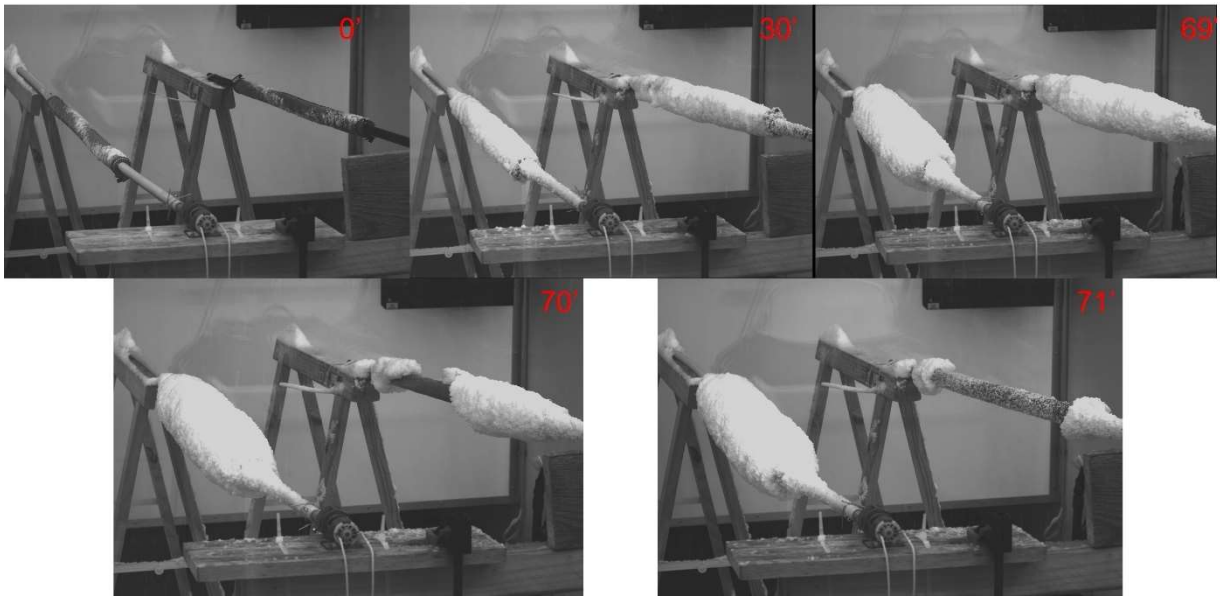

Figure 4.38 – stills from Test 1 recording. Reference left, Syl 186 right in the frame.

The test proceeded for 90' with snow detaching from Syl 186 sample after 70' from the start of the simulated precipitation. Snow didn't detach from the reference sample. At 70' minutes total snow sleeve diameter has been estimated at 100mm.

After the first snow shedding, that occurred on half of the total length of the sample, the structure of the remaining snow was weakened and complete detachment happened in <100''.

4.6.2.2 Test #2: PDMS-BL

PDMS-BL have been tested in the snow laboratory and compared with a bare Al sample. No delay in snow accumulation was seen. Snow shedding happened on PDMS-BL sample after 75 minutes, sleeve thickness has been estimated at 100mm.

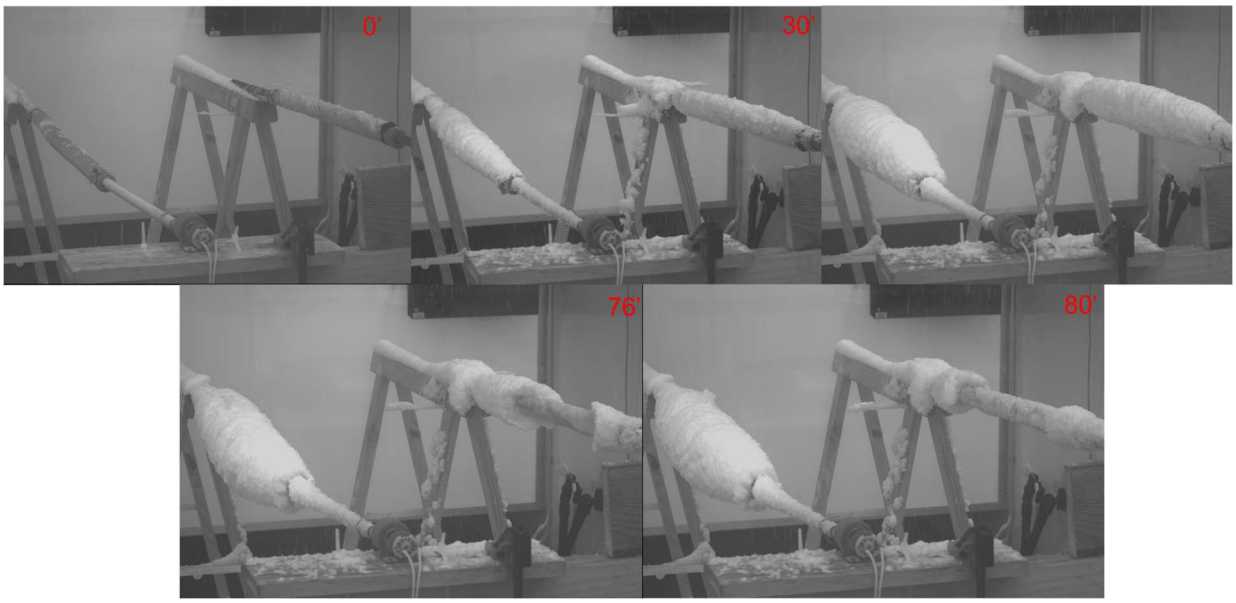

Figure 4.39 – stills from Test 1 recording. Reference left, PDMS-BL right in the frame.

PDMS-BL showed properties comparable to Syl 186. Direct comparison will be performed.

4.6.2.3 Test #3: M 10/2/1/2 186, PDMS @PO, Boehmite

Test #3 was made with 4 samples:

-a M 10/2/1/2 Syl 186 mixed matrix coating(10 parts Syl 186/ 2 parts PEG/ 1 high viscosity PDMS silicone oil/ 2 parts PMHS),

-a Peanut oil filled Syl 186 (10% oil in Syl 186, mixed) called PDMS@PO

-Al boehmite sample after 30' immersion in 0.5M HCl, 30' in boiling water, FAS coating (boehmite HCl 0.5M boil FAS)

-bare Al reference

Since the length of the wire spans has been doubled, shedding times are not to be compared with previous tests, due to differences in snow precipitation.

In this case, snow sleeve accumulation delay was reported for PDMS@PO. Snow sleeve diameter was measured after 1h: PDMS@PO samples reported a 10mm sleeve diameter while other samples all reported values around 20mm. Delay is clearly seen in images after 60' from test start. Complete

detachment after 85’ happened on M 10 2 1 2 186 , sleeve diameter has been estimated at 70mm at this time. Boehmite FAS detached from 50% of the sleeve after 110’.

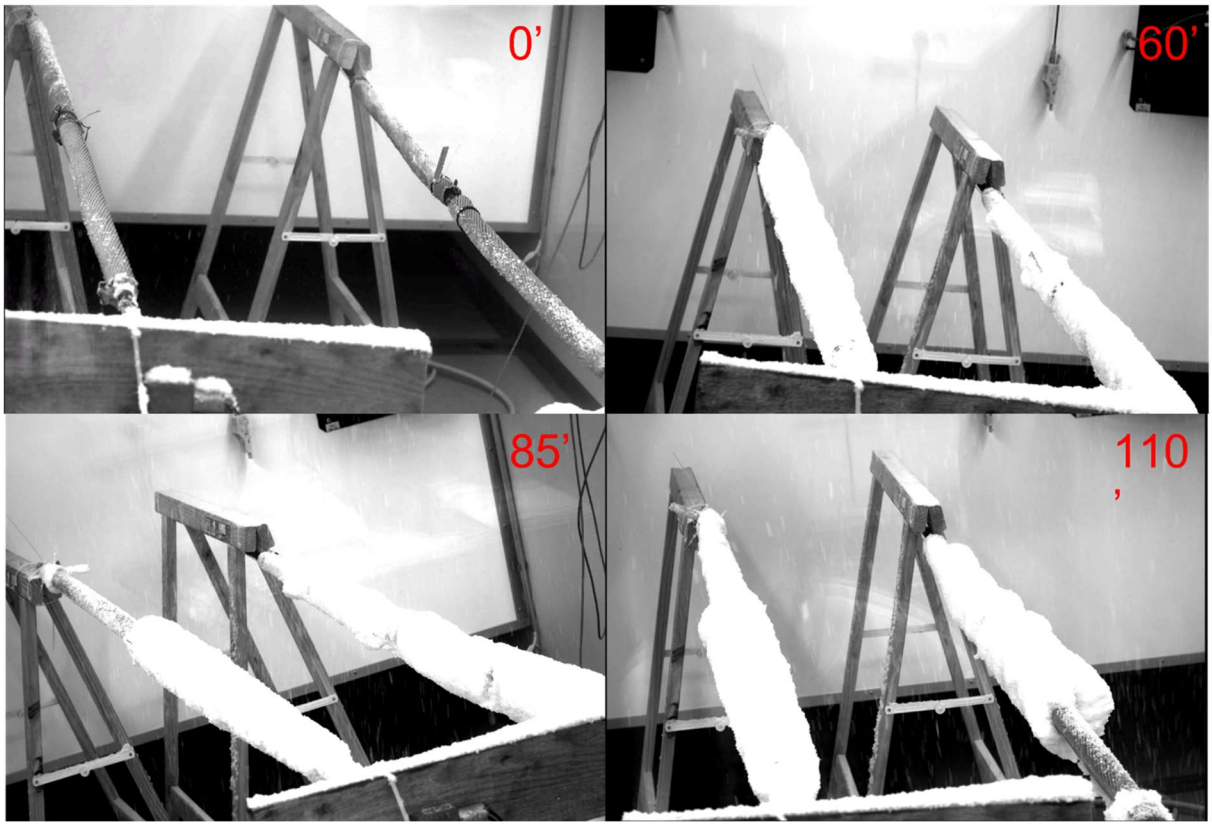

Figure 4.40 – stills from test #3: ref is bottom left, M 10 2 1 2 186 is upper left, PDMS@PO upper right, FAS boehmite is bottom right

It is interesting to note that this was the only tested sample to report a complete detachment of the snow sleeve all at once. Further testing is needed to link 4-sample and 2-sample characterization. The same samples tested here have been exposed in WILD station for 2022-2023 testing,.

4.6.2.4 Snow laboratory testing results: considerations

Snow laboratory testing is of great importance for this research. Not being subjected to seasonal testing, a much more propound comprehension of snow adhesion and shedding mechanisms can be obtained in far less time. Still, upgrades to the testing are needed as well as management of obtained snow conditions.

4.6.3 Ice wind tunnel

Ice wind testing have been conducted on cylinder samples (12mm diameter, 100mm length).

Glaze and rime have been accreted for respectively 4 and 5 minutes. After this time, samples have been turned of 90°. Then, wind speed have been raised up to 140 m/s in 10m/s steps each 20 seconds. If ice did not detach, temperature was increased at 2°C/min.

Bare Al and Syl 184 samples have been used as reference for others.

10_2_1_2 and 10_1_0_1 M-PDMS, C-PDMS of different PDMS-vyn/PMHS ratios, MM TEOS and P/T samples have been tested. Syl 184 10% PVDF contains, as the name implies, 10%wt of PVDF powder in Syl 184, mixed from liquid and heat treated at 120°C.

Results for glaze and rime adhesion are reported.

Table 4.24- Glaze ice test results.

Sample	Properties	Wind speed (m/s)	Temperature (°C)
Ref Al		140	4
Ref Syl 184	Elastomer	140	-2.1
M- PDMS 10_2_1_2	Liquid filled elastomer	130	-4
M-PDMS 10_1_0_1	Liquid filled elastomer	140	3.3
C-PDMS 30:1	Elastomer	140	-4
C-PDMS 15:1	Elastomer	120	-4

C-PDMS 5:1	Elastomer	120	-4
P/T 65cSt 1/1	Slippery	40	-4
P/T 750cSt 4/9	Slippery	50	-4
MM TEOS	Slippery	140	-1.8
Syl 184 + 10% PVDF	Particle filled elastomer	140	6.6

Table 4.25- Rime ice test results

Sample	Properties	Wind speed (m/s)	Temperature (°C)
Ref Al		140	6
Ref Syl 184	Elastomer	140	2.4
M- PDMS 10_2_1_2	Liquid filled elastomer	140	1.6
M-PDMS 10_1_0_1	Liquid filled elastomer	140	6
C-PDMS 30:1	Elastomer	140	3
C-PDMS 15:1	Elastomer	140	1.4
C-PDMS 5:1	Elastomer	140	1.8

P/T 65cSt 1/1	Slippery	140	-3.5
P/T 750cSt 4/9	Slippery	140	5.5
ALK	Slippery	140	6
Syl 184 + 10% PVDF	Particle filled elastomer	140	5

Rime appears more difficult to shed than glaze.

P/T samples showed outstanding results, in particular against glaze. M-PDMS and C-PDMS showed better results than Syl 184 reference. Syl 186 has not been tested at the time, so a direct comparison with C-PDMS is not available.

Ice detachment mechanism have been recorded with a high speed camera on a Syl 184 sample under glaze ice conditions.

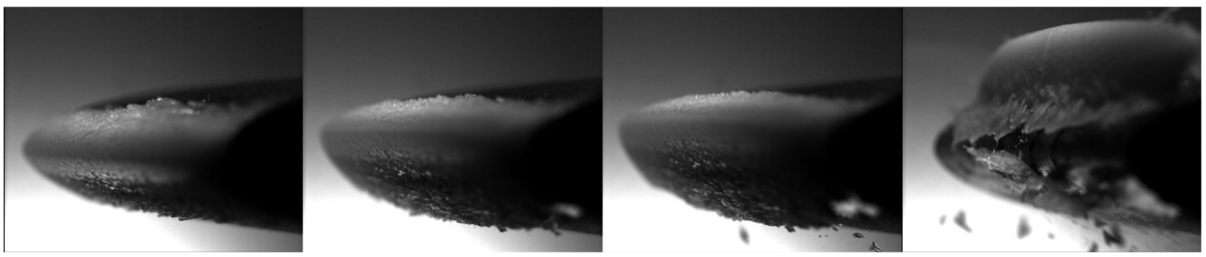

Figure 4.41 – high speed camera stills from wind tunnel ice detachment

5 CONCLUSIONS

Provision of electricity is of outstanding importance for our civilization.

In a world in which more and more electrical energy is requested every day and private transport is moving away from fossil fuels, the need for power grid that is robust and resilient is mandatory.

Robustness in operation, and resilience in case of faults, of the power grid relies on an enormous knowledge base, in terms of both theory and practice.

Everything in between a produced Watt and a consumed Watt needs to be taken care of to improve the quality of the electrical system.

e.g. From an electrical perspective, many steps are being taken towards the so-called “n-x” principle for design of power lines instead the “n-1” system which has been the standard for a long time. These definitions indicate the number of out of use distribution lines that can be withstood without letting users without electricity.

One of the main dangers power lines undergo is wide scale icing and snowing events. Such events can in some cases be disruptive for electrical transmission. To prevent this, the use of passive anti-icing methods is advocated as the best solution. Passive anti-icing include ice-phobic chemical coatings.

Coatings formulation must be cheap, scalable and durable.

These needs come from the fact that coatings need to be applied to a huge amount of conductors and guard wires and must resist any kind of weather.

Icing and snowing events of such magnitude to pose a danger to electrical lines are rare.

The extraordinariness of these events is in reality something to be feared even more. From one side, meteorologists cannot predict them much in advance, whereas, from a chemist’s perspective, the durability of a coating is as important as its effectiveness.

Another danger posed to power lines is pollution accumulation on insulators leading to flashovers. Flashovers are arc discharges that can damage structures and humans. A self-cleaning coating that could avoid the accumulation of large amounts of pollutants is needed as much as anti-icing materials on metal wires.

Several lines of research have been followed to cover the three most used materials: zinc plated steel. Aluminum and glass.

Zinc plated steel is used in guard wires, aluminum in conductors (and guard wires) and glass for insulators.

An ice testing machine has been conceived, electrically and mechanically designed, built, programmed, tested and, eventually, used, to obtain all the ice adhesion characterization presented in this dissertation.

5.1 Superhydrophobic Zinc surfaces

An important part of the research has been focused in synthesis and characterization of ice-phobic treatments and coatings for zinc plated steel guard wires, resulting in a publication (Superhydrophobic ice-phobic zinc surfaces).

Superhydrophobicity results from water droplets fluctuating above a hydrophobic hierarchical micro-nano structure in the so-called “fakir state”.

Zinc surfaces have been made superhydrophobic, growing ZnO Nanorods (NR) on their surface.

Since metals and their oxides are hydrophilic by nature, an hydrophobicizer needs to be applied on their surface to impart SHP properties.

ZnO NR have been grown with a short hydrothermal treatment. Treatment times have been reduced to the tens of minutes range (15’ and 30’) and the choice of an hydrothermal reaction tries to lean towards the needs for scalability, safety and price.

Superhydrophobic zinc samples have been tested in laboratory for anti-icing, giving good results with an ARF above 45 for FAS (Fluorinated alkyl silane) coated samples.

Stearic acid have been tested as an alternative to fluorinated coatings resulting in a ARF of 30.

Durability have been tested in wet chemical, along with the possibility to regenerate icephobicity after a new coat of hydrophobicizer. These test concluded that samples can withstand harsh wet chemical conditions for a month maintaining an ARF >2, up to 8. After recoating, some of the lost properties are recovered (~2-fold decrease of ice adhesion).

A 15m sample have been exposed during winter 2021-2022 in the WILD station in Vinadio, resulting in a snow load index of 0.57 and a coverage index of 0.74 (where 1 is bare sample load and coverage).

5.2 Elastomers

Research on elastomers has proceeded towards characterization of commercial Sylgard 184 and 186 ice-phobic properties. In particular, characterization on hardness and thickness effects.

Production of defined thickness coatings have been possible by building a manual tape casting machine, allowing the deposition of a uniform (less than 15% deviation across the surface of a single sample) layer of PDMS in the 100-1500 μm range.

PDMS is widely used for its chemical properties, including hydrophobicity and ice-phobicity.

Open field and snow laboratory testing have been conducted. These data lay a base for further developments, focused towards a real application.

Syl PDMS is a good starting base for modifications. This has been the focus of a conference paper (an ice-phobicity oriented approach to the chemico-physical modifications of PDMS) presented at IWAIS 2022.

Samples containing PEG-400, Pluronic, silicone oils have been produced. Direct incorporation in PDMS matrix (mixed matrix PDMS) has proven to have a positive effect in terms of ice adhesion reduction (max ARF 9.2).

M 10_2_1_2 sample has been tested for hardness, durability, efficacy against real conditions and laboratory snow. Durability resulted worse than PDMS, while snow laboratory testing resulted in probably the best result so far. The same sample have given good results in respect to Syl PDMS in a ice wind tunnel testing, conducted in the iCORE wind tunnel, in the Airbus facility, near Munich.

A treatment for the formation of uniform and macroscopical porosity on Syl PDMS have been researched.

This peculiar structure allows large scale (and large volume) slippery liquid infusing, which is a standard ice phobic countermeasure, but is only reported on a micro-nano scale. PDMS-B (“B” standing for bubbly due to appearance) samples reported low ice adhesion, characterized by a very long detachment displacement and time (20 times more than PDMS, ARF to PDMS 3-5). PDMS-BL samples showed

promising results in snow laboratory testing. The possibility to incorporate and gradually release lubricant have been tested on a 6 months span. After this time, positive effects for a sample sprayed with a commercial silicon lubricant are still seen. PDMS-B and PDMS-BL showed very a remarkable durability.

Mixed matrix PDMS and PDMS-B samples are exposed in the WILD station to test their behaviour in "certified and tested" alpine snow.

5.3 Photocatalytic TiO_2

TiO_2 is a probably "the" photocatalytic material. Research have been focused on developing and characterizing a set of treatments to obtain a durable adhesion of TiO_2 nanoparticles to glass.

Samples' photocatalytic properties have been characterized, resulting in the effectiveness of adhered coatings, with a clear dependence on Ti quantity on the surface, as measured with XRF characterization.

Samples have been tested for durability sustaining accelerated weathering tests and exposure to the elements.

TiO_2 photocatalytic nanoparticles have been deposited on glass from an aqueous dispersion and a low temperature thermal treatment (RT and 100°C for TEOS-TiO_2 samples, <250°C for TiO_2 particles alone), keeping in mind the application on composite insulators.

5.4 Sol-gel

Sol-gel reactions are widely used in materials chemistry to obtain nanoparticles and coatings.

5.4.1 PDMS-OH/TEOS

P/T samples showed outstanding results in terms of anti-fouling and anti-icing (especially in wind tunnel testing) but suffer from low durability.

A huge, and mostly unwritten, effort have been taken to improve durability of the coating by modifying sol-gel reaction conditions.

Data shown how shorter PDMS chains produce higher FRF (fouling reduction factors).

A deeper characterization is needed to understand mechanisms behind the effectiveness of P/T coatings, as well as ways to extend their durability.

5.4.2 Mixed Matrix TEOS

Base catalysed Mixed Matrix TEOS coatings have been synthesized. Laboratory data showed promising properties of water mobility at low temperature.

MM-TEOS coatings reported unexpectedly good results from WILD station testing (0.64 load and 0.68 coverage mean index) during 2020-2021 winter testing. Especially, MM-TEOS reported load and coverage indexes of 0.5 in the two major snowing events of that winter (420mm and 270mm snow on ground).

Further testing is needed for these samples.

5.5 Snow rings

Snow rings have been tested with good results. Though, their use is unlikely in this form, due to difficulties in installation on a real power line, unless they report unprecedented results. Still, testing in WILD station and snow laboratory can give more insights on the chemico-physical reasons behind their, so far, outstanding results in terms of avoiding sleeve accumulation.

5.6 Considerations

Anti.icing solutions for overhead conductors and guard wires have been proposed and tested, as well as anti-fouling ones for glass insulators.

Some of these coatings have been tested in open environment. Testing in real high voltage conditions requires more steps and more selection bottlenecks for a coating to go through. For reference, a single SHP Al samples tested on a 400m wire have been previously tested for >5 years of laboratory and open field testing and selection. SHP boehmite Al samples have been taken as a stepping stone,and somehow granted in laboratory testing and confrontation, for SHP Zn samples exposed in this dissertation.

Coatings' processes of selection will be sped up with snow laboratory testing, in terms of all-year availability of snow for testing At least, preliminary experiments showed consistent results. With the

same vision, a benchtop ice adhesion testing machine has been made and used for an easy laboratory characterization.

Power line upkeep has strict rules and uses, some of them better understood and basic ideas included in laboratory work of synthesis and characterization.

Notions from ice chemistry and physics have been understood and permeate many of the ideas and considerations reported in previous pages.

More testing and optimization is, as always, needed.

BIBLIOGRAPHY

[1] 'Electrical grid', *Wikipedia*. Dec. 05, 2022. Accessed: Dec. 14, 2022. [Online]. Available: https://en.wikipedia.org/w/index.php?title=Electrical_grid&oldid=1125802079

[2] 'electricalreviews.blogspot.com/2016/06'. http://electicalreviews.blogspot.com/2016/06/tower.html (accessed Dec. 14, 2022).

[3] 'Electric conductors in transmission lines', *The Energy of change*, May 24, 2016. http://www.theenergyofchange.com/electric-conductors-transmission-line (accessed Dec. 14, 2022).

[4] 'Design Criteria', *Power Line Magazine*, Jan. 26, 2016. https://powerline.net.in/2016/01/26/design-criteria/ (accessed Dec. 14, 2022).

[5] 'What is a Zinc Plating? - Definition from Corrosionpedia', *Corrosionpedia*. http://www.corrosionpedia.com/definition/1196/zinc-plating (accessed Dec. 14, 2022).

[6] P. Thorsson, 'Modelling of Atmospheric Icing', p. 57.

[7] L. Makkonen, 'Models for the growth of rime, glaze, icicles and wet snow on structures', *Philosophical Transactions of the Royal Society of London. Series A: Mathematical, Physical and Engineering Sciences*, vol. 358, no. 1776, pp. 2913–2939, Nov. 2000, doi: 10.1098/rsta.2000.0690.

[8] L. Makkonen, 'Estimating Intensity of Atmospheric Icing Accretion on Stationary Structures'.

[9] C. Volat and M. Farzaneh, 'De-icing / Anti-icing Techniques for Power Lines : Current Methods and Future Direction', 2005. Accessed: Dec. 14, 2022. [Online]. Available: https://www.semanticscholar.org/paper/De-icing-%2F-Anti-icing-Techniques-for-Power-Lines-%3A-Volat-Farzaneh/98a673da9f4d035c5bdd29ea728fd1aaa7f9a0d0

[10] Conseil international des grands réseaux électriques, Ed., *Coatings for protecting overhead power network equipment in winter conditions*. Paris: CIGRÉ, 2015.

[11] 'Audizione Enel 10ª Commissione Senato della Repubblica'. Aug. 02, 2017.

[12] 'RELAZIONE CONCLUSIVA SULLE INTERRUZIONI DEL SERVIZIO ELETTRICO OCCORSE NEI GIORNI 6 FEBBRAIO 2015 E SEGUENTI IN EMILIA ROMAGNA E LOMBARDIA'.

[13] Y. Furukawa, 'Structures and Formation Mechanisms of Snow Polycrystals', *Journal of the Meteorological Society of Japan*, vol. 60, no. 1, pp. 535–547, 1982, doi: 10.2151/jmsj1965.60.1_535.

[14] T. L. Malkin, B. J. Murray, A. V. Brukhno, J. Anwar, and C. G. Salzmann, 'Structure of ice crystallized from supercooled water', *Proc. Natl. Acad. Sci. U.S.A.*, vol. 109, no. 4, pp. 1041–1045, Jan. 2012, doi: 10.1073/pnas.1113059109.

[15] N. Dalili, A. Edrisy, and R. Carriveau, ‘A review of surface engineering issues critical to wind turbine performance’, *Renewable and Sustainable Energy Reviews*, vol. 13, no. 2, pp. 428–438, Feb. 2009, doi: 10.1016/j.rser.2007.11.009.

[16] ISO 12494:2017, ‘ISO 12494:2017’, *ISO*. https://www.iso.org/standard/72443.html (accessed Dec. 14, 2022).

[17] ‘glaze | meteorology | Britannica’. https://www.britannica.com/science/glaze (accessed Dec. 14, 2022).

[18] I. Tagliaro, A. Cerpelloni, V.-M. Nikiforidis, R. Pillai, and C. Antonini, ‘On the Development of Icephobic Surfaces: Bridging Experiments and Simulations’, in *The Surface Wettability Effect on Phase Change*, M. Marengo and J. De Coninck, Eds. Cham: Springer International Publishing, 2022, pp. 235–272. doi: 10.1007/978-3-030-82992-6_8.

[19] Y. Sakamoto, ‘Snow accretion on overhead wires’, *Philosophical Transactions of the Royal Society of London. Series A: Mathematical, Physical and Engineering Sciences*, vol. 358, no. 1776, pp. 2941–2970, Nov. 2000, doi: 10.1098/rsta.2000.0691.

[20] S. Würzer, N. Wever, R. Juras, M. Lehning, and T. Jonas, ‘Modelling liquid water transport in snow under rain-on-snow conditions – considering preferential flow’, *Hydrol. Earth Syst. Sci.*, vol. 21, no. 3, pp. 1741–1756, Mar. 2017, doi: 10.5194/hess-21-1741-2017.

[21] P. Bonelli, M. Lacavalla, P. Marcacci, G. Mariani, and G. Stella, ‘Wet snow hazard for power lines: a forecast and alert system applied in Italy’, *Nat. Hazards Earth Syst. Sci.*, vol. 11, no. 9, pp. 2419–2431, Sep. 2011, doi: 10.5194/nhess-11-2419-2011.

[22] Frank Techel, ‘The Influence of Water on Snow: micro-structural measurements and wet snow stability assessment’, Bern.

[23] J. Heil, B. Mohammadian, M. Sarayloo, K. Bruns, and H. Sojoudi, ‘Relationships between Surface Properties and Snow Adhesion and Its Shedding Mechanisms’, *Applied Sciences*, vol. 10, no. 16, p. 5407, Aug. 2020, doi: 10.3390/app10165407.

[24] S. Rønneberg, J. He, and Z. Zhang, ‘The need for standards in low ice adhesion surface research: a critical review’, *Journal of Adhesion Science and Technology*, vol. 34, no. 3, pp. 319–347, Feb. 2020, doi: 10.1080/01694243.2019.1679523.

[25] A. Work and Y. Lian, ‘A critical review of the measurement of ice adhesion to solid substrates’, *Progress in Aerospace Sciences*, vol. 98, pp. 1–26, Apr. 2018, doi: 10.1016/j.paerosci.2018.03.001.

[26] A. Dotan, H. Dodiuk, C. Laforte, and S. Kenig, ‘The Relationship between Water Wetting and Ice Adhesion’, *Journal of Adhesion Science and Technology*, vol. 23, no. 15, pp. 1907–1915, Jan. 2009, doi: 10.1163/016942409X12510925843078.

[27] M. Balordi, Santucci de Magistris, A. Cammi, and F. Pini, ‘Effect of experimental parameters on icephobic measurements’, *Proceedings – Int. Workshop on Atmospheric Icing of Structures IWAIS 2022 - Montreal, Canada, June 19-23*, vol. 077, [Online]. Available: https://www.mcgill.ca/iwais2022/files/iwais2022/paperid077.pdf

[28] M. Bleszynski and E. Clark, ‘Current Ice Adhesion Testing Methods and the Need for a Standard: A Concise Review’, *Standards*, vol. 1, no. 2, pp. 117–133, Nov. 2021, doi: 10.3390/standards1020011.

[29] X. Zhang and S. M. Rowland, ‘Modelling of dry-band discharge events on insulation surfaces’, in *2010 IEEE International Symposium on Electrical Insulation*, San Diego, CA, USA, Jun. 2010, pp. 1–5. doi: 10.1109/ELINSL.2010.5549489.

[30] Mohammed El Amine Slama, ‘Experimental Study and Modeling of the Effect of ESDD/NSDD on AC Flashover of SiR Outdoor Insulators’.

[31] H. L. Ems, ‘MICROSTRUCTURE ALONE INDUCED WETTING TRANSITION FROM HYDROPHILIC TO HYDROPHOBIC ON SILICON AND GRAPHENE’.

[32] T. Koishi, K. Yasuoka, S. Fujikawa, T. Ebisuzaki, and X. C. Zeng, ‘Coexistence and transition between Cassie and Wenzel state on pillared hydrophobic surface’, *Proc. Natl. Acad. Sci. U.S.A.*, vol. 106, no. 21, pp. 8435–8440, May 2009, doi: 10.1073/pnas.0902027106.

[33] S. Moulinet and D. Bartolo, ‘Life and death of a fakir droplet: Impalement transitions on superhydrophobic surfaces’, *Eur. Phys. J. E*, vol. 24, no. 3, pp. 251–260, Nov. 2007, doi: 10.1140/epje/i2007-10235-y.

[34] V. Hejazi, K. Sobolev, and M. Nosonovsky, ‘From superhydrophobicity to icephobicity: forces and interaction analysis’, *Sci Rep*, vol. 3, no. 1, p. 2194, Dec. 2013, doi: 10.1038/srep02194.

[35] M. Ghasemlou, F. Daver, E. P. Ivanova, and B. Adhikari, ‘Bio-inspired sustainable and durable superhydrophobic materials: from nature to market’, *J. Mater. Chem. A*, vol. 7, no. 28, pp. 16643–16670, 2019, doi: 10.1039/C9TA05185F.

[36] T. Darmanin and F. Guittard, ‘Superhydrophobic and superoleophobic properties in nature’, *Materials Today*, vol. 18, no. 5, pp. 273–285, Jun. 2015, doi: 10.1016/j.mattod.2015.01.001.

[37] A. M. A. Mohamed, ‘Corrosion behavior of superhydrophobic surfaces: A review’.

[38] Q. Ke, Y. Jin, P. Jiang, and J. Yu, ‘Oil/Water Separation Performances of Superhydrophobic and Superoleophilic Sponges’, *Langmuir*, vol. 30, no. 44, pp. 13137–13142, Nov. 2014, doi: 10.1021/la502521c.

[39] S. A. Kulinich, S. Farhadi, K. Nose, and X. W. Du, ‘Superhydrophobic Surfaces: Are They Really Ice-Repellent?’, *Langmuir*, vol. 27, no. 1, pp. 25–29, Jan. 2011, doi: 10.1021/la104277q.

[40] L. B. Boinovich and A. M. Emelyanenko, ‘Anti-icing Potential of Superhydrophobic Coatings’, *Mendeleev Communications*, vol. 23, no. 1, pp. 3–10, Jan. 2013, doi: 10.1016/j.mencom.2013.01.002.

[41] M. Balordi, G. Santucci de Magistris, and C. Chemelli, ‘A Novel Simple Anti-Ice Aluminum Coating: Synthesis and In-Lab Comparison with a Superhydrophobic Hierarchical Surface’, *Coatings*, vol. 10, no. 2, p. 111, Jan. 2020, doi: 10.3390/coatings10020111.

[42] L. Liu, J. Zhao, Y. Zhang, F. Zhao, and Y. Zhang, 'Fabrication of superhydrophobic surface by hierarchical growth of lotus-leaf-like boehmite on aluminum foil', *Journal of Colloid and Interface Science*, vol. 358, no. 1, pp. 277–283, Jun. 2011, doi: 10.1016/j.jcis.2011.02.036.

[43] G.-C. Yi, C. Wang, and W. I. Park, 'ZnO nanorods: synthesis, characterization and applications', *Semicond. Sci. Technol.*, vol. 20, no. 4, pp. S22–S34, Apr. 2005, doi: 10.1088/0268-1242/20/4/003.

[44] H. Meskine and P. A. Mulheran, 'Simulation of reconstructions of the polar ZnO (0001) surfaces', *Phys. Rev. B*, vol. 84, no. 16, p. 165430, Oct. 2011, doi: 10.1103/PhysRevB.84.165430.

[45] A. Resmini *et al.*, 'A simple all-solution approach to the synthesis of large ZnO nanorod networks', *J. Mater. Chem. A*, vol. 3, no. 8, pp. 4568–4577, 2015, doi: 10.1039/C4TA05207B.

[46] N. A. Hammed, A. A. Aziz, A. I. Usman, and M. A. Qaeed, 'The sonochemical synthesis of vertically aligned ZnO nanorods and their UV photodetection properties: Effect of ZnO buffer layer', *Ultrasonics Sonochemistry*, vol. 50, pp. 172–181, Jan. 2019, doi: 10.1016/j.ultsonch.2018.09.020.

[47] P. Dash, A. Manna, N. C. Mishra, and S. Varma, 'Synthesis and characterization of aligned ZnO nanorods for visible light photocatalysis', *Physica E: Low-dimensional Systems and Nanostructures*, vol. 107, pp. 38–46, Mar. 2019, doi: 10.1016/j.physe.2018.11.007.

[48] S. Kumar, P. D. Sahare, and S. Kumar, 'Optimization of the CVD parameters for ZnO nanorods growth: Its photoluminescence and field emission properties', *Materials Research Bulletin*, vol. 105, pp. 237–245, Sep. 2018, doi: 10.1016/j.materresbull.2018.05.002.

[49] N. A. Polyakov, I. G. Botryakova, V. G. Glukhov, G. V. Red'kina, and Yu. I. Kuznetsov, 'Formation and anticorrosion properties of superhydrophobic zinc coatings on steel', *Chemical Engineering Journal*, vol. 421, p. 127775, Oct. 2021, doi: 10.1016/j.cej.2020.127775.

[50] M. Wang, D. Zhang, Z. Yang, C. Yang, Y. Tian, and X. Liu, 'A Contrastive Investigation on the Anticorrosive Performance of Stearic Acid and Fluoroalkylsilane-Modified Superhydrophobic Surface in Salt, Alkali, and Acid Solution', *Langmuir*, vol. 36, no. 34, pp. 10279–10292, Sep. 2020, doi: 10.1021/acs.langmuir.0c02080.

[51] L. E. Roth, E. M. Vallés, and M. A. Villar, 'Bulk hydrosilylation reaction of poly(dimethylsiloxane) chains catalyzed by a platinum salt: Effect of the initial concentration of reactive groups on the final extent of reaction: Bulk Hydrosilylation Reaction', *J. Polym. Sci. A Polym. Chem.*, vol. 41, no. 8, pp. 1099–1106, Apr. 2003, doi: 10.1002/pola.10649.

[52] R. Hofmann, M. Vlatković, and F. Wiesbrock, 'Fifty Years of Hydrosilylation in Polymer Science: A Review of Current Trends of Low-Cost Transition-Metal and Metal-Free Catalysts, Non-Thermally Triggered Hydrosilylation Reactions, and Industrial Applications', *Polymers*, vol. 9, no. 12, p. 534, Oct. 2017, doi: 10.3390/polym9100534.

[53] F. Chambon and H. H. Winter, 'Linear Viscoelasticity at the Gel Point of a Crosslinking PDMS with Imbalanced Stoichiometry', *Journal of Rheology*, vol. 31, no. 8, pp. 683–697, Nov. 1987, doi: 10.1122/1.549955.

[54] S. Deguchi, J. Hotta, S. Yokoyama, and T. S. Matsui, 'Viscoelastic and optical properties of four different PDMS polymers', *J. Micromech. Microeng.*, vol. 25, no. 9, p. 097002, Sep. 2015, doi: 10.1088/0960-1317/25/9/097002.

[55] D. L. Beemer, W. Wang, and A. K. Kota, 'Durable gels with ultra-low adhesion to ice', *J. Mater. Chem. A*, vol. 4, no. 47, pp. 18253–18258, 2016, doi: 10.1039/C6TA07262C.

[56] J. Yong *et al.*, 'Femtosecond Laser Weaving Superhydrophobic Patterned PDMS Surfaces with Tunable Adhesion', *J. Phys. Chem. C*, vol. 117, no. 47, pp. 24907–24912, Nov. 2013, doi: 10.1021/jp408863u.

[57] C. W. Schultz, C. L. W. Ng, and H.-Z. Yu, 'Superhydrophobic Polydimethylsiloxane via Nanocontact Molding of Solvent Crystallized Polycarbonate: Optimized Fabrication, Mechanistic Investigation, and Application Potential', *ACS Appl. Mater. Interfaces*, vol. 12, no. 2, pp. 3161–3170, Jan. 2020, doi: 10.1021/acsami.9b18041.

[58] J. Petit and E. Bonaccurso, 'General Frost Growth Mechanism on Solid Substrates with Different Stiffness', *Langmuir*, vol. 30, no. 4, pp. 1160–1168, Feb. 2014, doi: 10.1021/la404084m.

[59] L. Zhu, J. Xue, Y. Wang, Q. Chen, J. Ding, and Q. Wang, 'Ice-phobic Coatings Based on Silicon-Oil-Infused Polydimethylsiloxane', *ACS Publications*, May 03, 2013. https://pubs.acs.org/doi/pdf/10.1021/am400704z (accessed Dec. 14, 2022).

[60] B. Liu *et al.*, 'Strategies for anti-icing: low surface energy or liquid-infused?', *RSC Adv.*, vol. 6, no. 74, pp. 70251–70260, 2016, doi: 10.1039/C6RA11383D.

[61] P. F. Ibáñez-Ibáñez, F. J. Montes Ruiz-Cabello, M. A. Cabrerizo-Vílchez, and M. A. Rodríguez-Valverde, 'Ice adhesion of PDMS surfaces with balanced elastic and water-repellent properties', *Journal of Colloid and Interface Science*, vol. 608, pp. 792–799, Feb. 2022, doi: 10.1016/j.jcis.2021.10.005.

[62] D. Chen, M. D. Gelenter, M. Hong, R. E. Cohen, and G. H. McKinley, 'Icephobic Surfaces Induced by Interfacial Nonfrozen Water', *ACS Appl. Mater. Interfaces*, vol. 9, no. 4, pp. 4202–4214, Feb. 2017, doi: 10.1021/acsami.6b13773.

[63] F. Wang, W. Ding, J. He, and Z. Zhang, 'Phase transition enabled durable anti-icing surfaces and its DIY design', *Chemical Engineering Journal*, vol. 360, pp. 243–249, Mar. 2019, doi: 10.1016/j.cej.2018.11.224.

[64] R. Gulfam, D. Orejon, C.-H. Choi, and P. Zhang, 'Phase-Change Slippery Liquid-Infused Porous Surfaces with Thermo-Responsive Wetting and Shedding States', *ACS Appl. Mater. Interfaces*, vol. 12, no. 30, pp. 34306–34316, Jul. 2020, doi: 10.1021/acsami.0c06441.

[65] 'Self-cleaning of superhydrophobic surfaces by self-propelled jumping condensate | PNAS'. https://www.pnas.org/doi/10.1073/pnas.1210770110 (accessed Dec. 14, 2022).

[66] S. Hosseini, *Self-Cleaning surfaces for different purposes: Review of production methods and future prospects*. 2020.

[67] Q. Xu, W. Zhang, C. Dong, T. S. Sreeprasad, and Z. Xia, 'Biomimetic self-cleaning surfaces: synthesis, mechanism and applications', *Journal of The Royal Society Interface*, vol. 13, no. 122, p. 20160300, Sep. 2016, doi: 10.1098/rsif.2016.0300.

[68] 'Self-Cleaning Properties of Super-Hydrophobic Silicone for High Voltage Insulators -'. https://www.inmr.com/self-cleaning-properties-super-hydrophobic-silicone-high-voltage-insulators/ (accessed Dec. 14, 2022).

[69] L. E. Correa, E. Velilla, M. Gómez, F. Echeverría, A. Marín, and J. G. Castaño, 'Evaluación del desempeño de aisladores de porcelana recubiertos con películas de dióxido de titanio para disminuir el ensuciamiento', 2013.

[70] V. A. Ganesh, H. K. Raut, A. S. Nair, and S. Ramakrishna, 'A review on self-cleaning coatings', *J. Mater. Chem.*, vol. 21, no. 41, p. 16304, 2011, doi: 10.1039/c1jm12523k.

[71] C. Xu, P. Ravi Anusuyadevi, C. Aymonier, R. Luque, and S. Marre, 'Nanostructured materials for photocatalysis', *Chem. Soc. Rev.*, vol. 48, no. 14, pp. 3868–3902, 2019, doi: 10.1039/C9CS00102F.

[72] A. Beeldens, 'An environmental friendly solution for air purification and self-cleaning effect: the application of TIO2 as photocatalyst in concrete'.

[73] J. O. Carneiro *et al.*, 'Development of photocatalytic asphalt mixtures by the deposition and volumetric incorporation of TiO2 nanoparticles', *Construction and Building Materials*, vol. 38, pp. 594–601, Jan. 2013, doi: 10.1016/j.conbuildmat.2012.09.005.

[74] L. Li, B. Li, J. Dong, and J. Zhang, 'Roles of silanes and silicones in forming superhydrophobic and superoleophobic materials', *J. Mater. Chem. A*, vol. 4, no. 36, pp. 13677–13725, 2016, doi: 10.1039/C6TA05441B.

[75] Q. Fu *et al.*, 'Development of Sol–Gel Icephobic Coatings: Effect of Surface Roughness and Surface Energy', *ACS Appl. Mater. Interfaces*, vol. 6, no. 23, pp. 20685–20692, Dec. 2014, doi: 10.1021/am504348x.

[76] M. Poddighe and P. Innocenzi, 'Hydrophobic Thin Films from Sol–Gel Processing: A Critical Review', *Materials*, vol. 14, no. 22, p. 6799, Nov. 2021, doi: 10.3390/ma14226799.

[77] M. Boudot, V. Gaud, M. Louarn, M. Selmane, and D. Grosso, 'Sol–Gel Based Hydrophobic Antireflective Coatings on Organic Substrates: A Detailed Investigation of Ammonia Vapor Treatment (AVT)', *Chem. Mater.*, vol. 26, no. 5, pp. 1822–1833, Mar. 2014, doi: 10.1021/cm403787v.

[78] L. V. Ng and A. V. McCormick, 'Acidic Sol−Gel Polymerization of TEOS: Effect of Solution Composition on Cyclization and Bimolecular Condensation Rates', *J. Phys. Chem.*, vol. 100, no. 30, pp. 12517–12531, Jan. 1996, doi: 10.1021/jp960089o.

[79] G. D. Sorarù, N. Dallabona, C. Gervais, and F. Babonneau, 'Organically Modified SiO2−B2O3 Gels Displaying a High Content of Borosiloxane (B−O−Si:) Bonds', *Chem. Mater.*, vol. 11, no. 4, pp. 910–919, Apr. 1999, doi: 10.1021/cm980353l.

[80] G. E. Newby, I. W. Hamley, S. M. King, C. M. Martin, and N. J. Terrill, 'Structure, rheology and shear alignment of Pluronic block copolymer mixtures', *Journal of Colloid and Interface Science*, vol. 329, no. 1, pp. 54–61, Jan. 2009, doi: 10.1016/j.jcis.2008.09.054.

[81] G. Wakahama, D. Kuroiwa, and K. Gotō, 'Snow Accretion on Electric Wires and its Prevention', *J. Glaciol.*, vol. 19, no. 81, pp. 657–657, 1977, doi: 10.3189/S0022143000215682.

[82] 'Dispositivi per prevenire interruzioni di corrente dovute alla neve - HEPCO Network'. https://www.hepco.co.jp/network/stable_supply/efforts/snow_prevention/index.html (accessed Dec. 14, 2022).

[83] R. Entz and R. Jorge, *Non-Intrusive Ice Accretion Detection and Measurement System*. 2016.

[84] S. Alamri *et al.*, 'Self-Limited Ice Formation and Efficient De-Icing on Superhydrophobic Micro-Structured Airfoils through Direct Laser Interference Patterning', *Advanced Materials Interfaces*, vol. 7, no. 22, p. 2001231, 2020, doi: 10.1002/admi.202001231.

[85] V. Vercillo *et al.*, 'Analysis and modelling of icing of air intake protection grids of aircraft engines', *Cold Regions Science and Technology*, vol. 160, Apr. 2019, doi: 10.1016/j.coldregions.2019.01.012.

[86] 'Wet-snow accretion on Overhead Lines. The RSE response to harmful winter blackouts in Italy', *RSE*. https://www.rse-web.it/pubblicazioni/wet-snow-accretion-on-overhead-lines-the-rse-response-to-harmful-winter-blackouts-in-italy-316007/ (accessed Dec. 14, 2022).

[87] M. Balordi *et al.*, 'A comparison of anti-ice and anti-snow coatings performances: laboratory and field testing', p. 6.

[88] 'Misura del diametro dei manicotti di ghiaccio su conduttori elettrici con il sistema ELISAm', *RSE*. https://www.rse-web.it/news/misura-del-diametro-dei-manicotti-di-ghiaccio-su-conduttori-elettrici-con-il-sistema-elisam/ (accessed Dec. 14, 2022).

[89] M. Balordi, F. Pini, and G. Santucci de Magistris, 'Superhydrophobic ice-phobic zinc surfaces', *Surfaces and Interfaces*, vol. 30, p. 101855, Jun. 2022, doi: 10.1016/j.surfin.2022.101855.

[90] R. Shi, P. Yang, X. Dong, Q. Ma, and A. Zhang, 'Growth of flower-like ZnO on ZnO nanorod arrays created on zinc substrate through low-temperature hydrothermal synthesis', *Applied Surface Science*, vol. 264, pp. 162–170, Jan. 2013, doi: 10.1016/j.apsusc.2012.09.164.

[91] H. Zhang *et al.*, 'Controllable growth of ZnO nanostructures by citric acid assisted hydrothermal process', *Materials Letters*, vol. 59, no. 13, pp. 1696–1700, Jun. 2005, doi: 10.1016/j.matlet.2005.01.056.

[92] K.-C. Hsu, J.-D. Liao, and Y.-S. Fu, 'Hydrothermal Synthesis of ZnO Nanorods using the HMT Surfactant', *Integrated Ferroelectrics*, vol. 143, no. 1, pp. 97–106, Jan. 2013, doi: 10.1080/10584587.2013.796233.

[93] A. Kathalingam, H.-C. Park, S.-D. Kim, H.-S. Kim, S. Velumani, and T. Mahalingam, 'Synthesis of ZnO nanorods using different precursor solutions and their two terminal device characterization', *J Mater Sci: Mater Electron*, vol. 26, no. 8, pp. 5724–5734, Aug. 2015, doi: 10.1007/s10854-015-3129-6.

[94] A. B. Gurav *et al.*, 'Superhydrophobic surface decorated with vertical ZnO nanorods modified by stearic acid', *Ceramics International*, vol. 40, no. 5, pp. 7151–7160, Jun. 2014, doi: 10.1016/j.ceramint.2013.12.052.

[95] L. B. Boinovich and A. M. Emelyanenko, 'The behaviour of fluoro- and hydrocarbon surfactants used for fabrication of superhydrophobic coatings at solid/water interface', *Colloids and Surfaces A: Physicochemical and Engineering Aspects*, vol. 481, pp. 167–175, Sep. 2015, doi: 10.1016/j.colsurfa.2015.05.003.

[96] P. Ciambelli *et al.*, 'Vanadium oxide catalysts supported on laser-synthesized titania powders: Characterization and catalytic activity in the selective reduction of nitric oxide', *Applied Catalysis B-environmental - APPL CATAL B-ENVIRON*, vol. 1, pp. 61–77, Jun. 1992, doi: 10.1016/0926-3373(92)80033-V.

6 ACRONYMS

Acronnym	Description
DW	distilled water
ZPS	zinc plated steel
SHP	superhydrophobic
CA	Contact Angle
RO	Roll-Off angle
SA	Sliding Angle
SFE	surface free energy
ARF	adhesion reduction factor
AC	anticorodal
FRF	fouling reduction factor
ZnO NR	zinc oxide nanorods
SEM	scanning electron microscope
LWC	liquid water content
PEG	Poly Ethylen glycol
PPG	Poly Propylen Glycol
PDMS	Polydimthyl siloxane
PMHS	Poly methyl hydro siloxane
FAS	Fluorinated alkyl silane (SIVO EC)
STA	Stearic acid
EtOH	ethanol
PLA	Poly Lactic acid
ABS	Acrylonitrile Butadiene Styrene
ZPS	Zinc plated steel
iPrOH	2-propanol
Syl	Sylgard
YM	Young modulus